



# **In-depth modelling and simulation of cerebral cortex in traumatic brain injury**

*by* Arpad Bakonyi, BSc

*A research project to be conducted under the supervision of*

Professor Ali M. Sadegh, PhD, PE  
Director of the Center for Advanced Engineering Design and Development,  
Department for Mechanical Engineering  
*at*  
The City College of New York, CUNY

*A thesis submitted in partial fulfilment of the requirements for the degree of  
Master of Science in Engineering*

*at the*  
University of Applied Sciences Technikum Wien

*under the supervision of*

Gudrun Kinz, Dipl.-Ing.  
UAS Technikum Wien

## Eidesstattliche Erklärung

„Ich, als Autor / als Autorin und Urheber / Urheberin der vorliegenden Arbeit, bestätige mit meiner Unterschrift die Kenntnisnahme der einschlägigen urheber- und hochschulrechtlichen Bestimmungen (vgl. Urheberrechtsgesetz idgF sowie Satzungsteil Studienrechtliche Bestimmungen / Prüfungsordnung der FH Technikum Wien idgF).

Ich erkläre hiermit, dass ich die vorliegende Arbeit selbständig angefertigt und Gedankengut jeglicher Art aus fremden sowie selbst verfassten Quellen zur Gänze zitiert habe. Ich bin mir bei Nachweis fehlender Eigen- und Selbstständigkeit sowie dem Nachweis eines Vorsatzes zur Erschleichung einer positiven Beurteilung dieser Arbeit der Konsequenzen bewusst, die von der Studiengangsleitung ausgesprochen werden können (vgl. Satzungsteil Studienrechtliche Bestimmungen / Prüfungsordnung der FH Technikum Wien idgF).

Weiters bestätige ich, dass ich die vorliegende Arbeit bis dato nicht veröffentlicht und weder in gleicher noch in ähnlicher Form einer anderen Prüfungsbehörde vorgelegt habe. Ich versichere, dass die abgegebene Version jener im Uploadtool entspricht.“

---

Ort, Datum

---

Unterschrift

## **Declaration of Authenticity**

“As author and creator of this work to hand, I confirm with my signature knowledge of the relevant copyright regulations governed by higher education acts (for example see §§ 21, 42f and 57 UrhG (Austrian copyright law) as amended as well as § 14 of the Statute on Studies Act Provisions / Examination Regulations of the UAS Technikum Wien).

In particular, I declare that I have made use of third-party content correctly, regardless what form it may have, and I am aware of any consequences I may face on the part of the degree program director if there should be evidence of missing autonomy and independence or evidence of any intent to fraudulently achieve a pass mark for this work (see § 14 para. 1 Statute on Studies Act Provisions / Examination Regulations of the UAS Technikum Wien).

I further declare that up to this date I have not published the work to hand nor have I presented it to another examination board in the same or similar form. I affirm that the version submitted matches the version in the upload tool.”

---

Place, Date

---

Signature

## Kurzfassung

Im Falle einer Kontakt-Kopfverletzung, die Gehirnrinde ist die primäre Struktur, die aufgrund des Umstoßens des Gehirns einer Druck-/Zugspannungsbelastung ausgesetzt ist. Die graue Substanz im Neocortex enthält die meisten neuronalen Zellkörper des Gehirns und steuert die Muskel- und Sinneswahrnehmung. Sie ist das meistbetroffene Gewebe bei der Entstehung von Gehirnerschütterungen und Schädel-Hirn-Traumata (SHT). Die mechanischen Materialeigenschaften der grauen Substanz bezüglich SHT wurden im Detail jedoch noch nicht untersucht. Forschung in dem Feld wird voraussichtlich wichtige Ergebnisse in den Bereichen Kontaktsport, Sportverletzungen, Unfallmechanik, Verteidigungsindustrie, Fahrzeugsicherheit sowie im allgemeinen Gesundheitsmanagement liefern. Die Grundlage zur Analyse des SHT-Mechanismus besteht darin, ein detailliertes Modell des Gehirns mit entsprechenden Materialmodellen zu erstellen. In dieser Studie wurde ein Präparat des dorsolateralen superioren frontalen Kortex aus einem Kadavergehirn extrahiert. Nach optischer Analyse der Zellstruktur konnten sechs verschiedene Schichten des Neokortexes identifiziert werden. Die Probe wurde mittels Nanoindrucks-Experimenten an einem Atomkraftmikroskop auf Materialeigenschaften untersucht, wobei der Schwerpunkt auf dem Unterschied zwischen den identifizierten Schichten lag. Elastizitätsmodule konnten für jede Schicht aus Messungen erhalten und statistisch aufbereitet werden. In ähnlicher Weise wurden dimensionslose Prony-Parameter extrahiert, indem zeitabhängige Relaxations-experimente durchgeführt wurden und Durchschnittswerte der Parameter für jede Schicht erstellt wurden. Unterschiede zwischen den Schichten hinsichtlich der elastischen und viskoelastischen Eigenschaften waren offensichtlich. Es wurde beobachtet, dass das Elastizitätsmodul der Schicht III signifikant höher war als das der Schicht I ( $p=0,15$ ). Dimensionslose viskoelastische Relaxationskurven der Schichten zeigten auffällige Muster von Unterschieden und Ähnlichkeiten. Die erhaltenen Parameter wurden in einer FEM-Simulation eines lokalen Modells des Neokortexes angewendet. Die resultierende Dehnung von Modellen mit und ohne geschichtete graue Substanz wurde im gleichen Spannungszustand verglichen, mit besonderem Fokus auf der Differenz des Spannungszustands der Schichten. Schichten I und II erlitten Dehnungsbelastungen über dem kritischen Niveau von 0,15, während die höchste Dehnung in den anderen Schichten bei etwa 0,07 blieb. Es kann daraus schließen, dass das Präsenz von Pyramidenzellen zusammen mit der Myelinendichte vermutlich die Steifigkeit, die Viskosität und damit die Belastbarkeit der Schichten beeinflusst. In dieser Studie wurden detaillierte FEM-Simulationen des Neocortexes zum ersten Mal durchgeführt, somit einen wichtigen Beitrag in dem Gebiet geleistet.

## Abstract

At a contact head injury event, the cortex of the brain is the primary structure that is subjected to a compressive or tensile load due to the coup and counter coup of the brain. The grey matter neocortex contains most of the brain's neuronal cell bodies, and controls muscle and sensory perception, playing an important role in the causation of concussions and traumatic brain injury (TBI). However, the detailed mechanical material properties of the grey matter as they relate to the outcomes of TBI have not been investigated yet. Research focusing on TBI is expected to yield important results in the fields of contact sports, sports injuries, general injury mechanics, military and defense engineering, automotive safety and in general health management. The key approach to assess TBI mechanism is to create a detailed model of the brain along with appropriate material modeling. In this study, a specimen of the dorsolateral superior frontal cortex was extracted from a cadaveric brain. After visual assessment of the cellular structure, six distinct layers of the neocortex could be identified. The specimen was examined for its material properties with AFM nanoindentation experiments, focusing on the differences among identified layers. Young's Moduli could be obtained for each layer from several measurements and statistically analyzed for differences. Likewise, dimensionless Prony-parameters were extracted by conducting time-dependent relaxation experiments, and by building mean values of the parameters for each layer. Differences were apparent among layers regarding both elastic and viscoelastic properties. The elastic modulus of layer III was observed to be significantly higher than that of layer I ( $p=0.15$ ). Dimensionless viscoelastic relaxation functions for each layer demonstrated remarkable patterns of differences and similarities in decay. The obtained viscoelastic parameters for each layer were applied to a FEM simulation of a local model of the neocortex. The strain response of models with and without a layered grey matter were compared for the same stress state, with special focus on the difference of the resulting strain state between layers. Layers I and II were observed to sustain considerable strains above the critical level of 0.15, whereas the highest strain in the other layers remained around 0.07. It could be concluded that the presence of pyramidal cells along with the myelin density presumably influences stiffness, viscosity and therefore the vulnerability across the layers. Material properties of neocortical layers have not been experimentally examined before. In this study, detailed mechanical FEM simulations of the deeper neocortical architecture were concluded. Therefore, this research is an important contribution to the field of in-depth head injury simulations.

## ACKNOWLEDGEMENT

First I would like to thank my advisor, DI Gudrun Kinz at the University of Applied Sciences (UAS) Technikum Vienna, for the supervision of my thesis, and the UAS, my home university for their organizational support in collaboration with the Austrian Marshall Plan Foundation.

I would like to express my deepest gratitude to the Austrian Marshall Plan Foundation for granting me the Marshall Plan Scholarship which enabled conducting my research as a visitor in the USA.

I am gratefully indebted to my second advisor, Prof. Ali M. Sadegh, PhD, PE, at the City College of New York (CCNY) for his important support during my entire stay and his valuable comments on this thesis. I am thankful that his door always stood open for me and that he advised me in any issue. The atmosphere of his project group helped me enjoy my workdays at the university a lot. I greatly appreciate that Prof. Sadegh did his best to provide me any technical requirements and appropriate circumstances to be able to conduct my work. At this point I would also express my gratitude to the CCNY of the City University of New York for providing the infrastructure and laboratory equipment and for the organizational support.

Additionally, I would like to express my appreciation to my colleagues in the work group, Siavash Hashemi and Shahabedin Mansoorbaghaei for their valuable inputs, Avi Fajtelewitz for assisting me during my experimental work, Prof. Luis Cardoso for providing the computational infrastructure of his laboratory, and Darryl Warner, Chief College Lab Technician and Gross Anatomy Diener for making it possible to employ a human cadaver for my experimental work.

Finally, I would like to express my gratitude towards my parents for their continuous support and encouragement throughout my years of study, along with my entire family and friends for being there for me and motivating me during my stay abroad. This accomplishment would not have been possible without them. Thank you.

## Abbreviations

AFM – Atomic force microscopy  
ANOVA – Analysis of variance  
CAD – Computer aided design  
CNS – Central nervous system  
CSDM – Cumulated Strain Damage Method  
CSF – Cerebrospinal fluid  
CT – Computer tomography  
CTE – Chronic traumatic encephalopathy  
DAI – Diffuse axonal injury  
FE – Finite element  
FEM – Finite element method  
GLI – Grey level index  
GM – Grey matter  
H&E – Hematoxylin-eosin  
HIC – Head Injury Criterion  
LEPmax – Maximum principal logarithmic strain  
MRE – Magnetic resonance elastography  
MRI – Magnetic resonance imaging  
mTBI – Mild traumatic brain injury  
QLV – Quasi linear viscoelasticity  
SAS – Subarachnoid space  
TBI – Traumatic brain injury  
WM – White matter

## Table of contents

Kurzfassung .....	4
Abstract .....	5
ACKNOWLEDGEMENT .....	6
Abbreviations .....	7
Table of contents .....	8
1. Introduction .....	11
1.1. Motivation .....	11
1.2. Objectives .....	12
1.3. The structure of this thesis .....	12
1.4. Literature review .....	13
1.4.1. Indentation measurements .....	13
1.4.2. Material models for grey and white matter .....	14
1.4.3. Measurement of grey and white matter properties .....	14
1.4.4. Cellular constitution of the neocortex .....	15
1.4.5. Functionality of layers .....	16
1.4.6. Studying of accidental injuries of the head .....	16
2. Anatomy and Histology .....	16
2.1. Brain .....	16
2.1.1. The function of the brain .....	17
2.1.2. Structural and mechanical properties .....	17
2.1.3. Cerebrum .....	20
2.2. The cerebral cortex .....	20
2.3. Constitution of GM and WM .....	22
2.3.1. Layers of the GM neocortex .....	23
2.4. Neuronal architecture .....	24
2.4.1. Pyramidal neurons .....	27
3. Head biomechanics .....	28
3.1. Head injuries .....	28
3.2. Traumatic brain injury .....	29
3.3. Trauma biomechanics .....	31
3.4. Head impact mechanics .....	35
3.5. Material models .....	36



3.5.1.	Elasticity .....	37
3.5.2.	Viscoelasticity.....	38
3.5.3.	Hyperelasticity .....	42
3.6.	Material properties of GM and WM .....	42
3.6.1.	Elastic properties.....	43
3.6.2.	Hyperelastic properties .....	43
3.6.3.	Viscoelastic properties .....	44
3.7.	Experimental measurement of material properties .....	45
3.7.1.	Measurements for elasticity .....	45
3.7.2.	Measurements for viscoelasticity.....	45
3.7.3.	Indentation measurements with AFM.....	45
4.	Employed experimental methods.....	51
4.1.	Preparation of the sample.....	51
4.1.1.	Cadaver .....	51
4.1.2.	Preparation and segmentation .....	53
4.1.3.	Microtome slicing .....	53
4.2.	Microscopy .....	56
4.3.	AFM measurements .....	56
4.3.1.	Instrument properties .....	57
4.3.2.	Choice of the cantilever .....	59
4.3.3.	Calibration.....	61
4.3.4.	Preparing the specimen .....	63
4.4.	Measuring the E-modulus .....	65
4.4.1.	Force distance .....	65
4.4.2.	Trigger.....	66
4.4.3.	Calculation methods.....	69
4.4.3.1.	Zero contact point .....	69
4.4.3.2.	Computed variables .....	71
4.4.3.3.	Young modulus calculation .....	71
4.4.4.	Statistical assessment .....	71
4.4.4.1.	Outliers.....	71
4.4.4.2.	Comparative statistics .....	72
4.5.	Measurements for viscoelastic parameters .....	73
4.5.1.	Computational methods .....	75

4.5.1.1.	Zero-point correction .....	76
4.5.1.2.	Calculating the shear function .....	76
4.5.2.	Statistical analysis .....	77
4.5.2.1.	Outliers.....	77
4.5.2.2.	Comparative statistics .....	78
4.6.	Statistical methods .....	78
4.7.	Computational methods .....	79
4.7.1.	Global head model .....	79
4.7.1.1.	Meshing.....	80
4.7.1.2.	Applied material models .....	82
4.7.1.3.	Results from the global model .....	82
4.7.2.	Local models.....	84
4.7.2.1.	Meshing.....	85
	.....	86
4.7.2.2.	Material models .....	86
4.7.2.3.	Load and boundary conditions.....	87
5.	Results.....	88
5.1.	Microscopic images .....	88
5.2.	Elastic properties.....	90
5.3.	Viscoelastic properties .....	93
5.4.	FEM simulations.....	95
6.	Discussion.....	96
6.1.	Limitations of this study .....	99
7.	Conclusion .....	101
8.	Extension in future studies.....	102
	Bibliography .....	104
	Appendix A – <i>An overview of cortical cell characteristics</i> .....	114
	Appendix B - <i>Technical specifications of the applied cantilever</i> .....	115
	Appendix C - <i>Transitions between layers on AFM images (<math>\mu\text{m}</math> scale)</i> .....	116

# 1. Introduction

## 1.1. Motivation

This research project was conducted in the cross-discipline research field of brain biomechanics and injury mechanics, focusing on the mechanism and outcomes of traumatic brain injury (TBI). TBI is an intracranial injury caused by impacts or angular accelerations of the head such as a violent blow, a bump, a projectile, or blast shockwaves, inducing an instantaneous displacement and deformations, as well as a relative motion between the brain (cortex) and the skull (cranium). Neuronal injury itself occurs because of the resulting strains inside the tissue. TBI has a high incidence rate of fatal and non-fatal hospitalizations. The average number of such injuries in the United States is approximately 175 to 200 per 100,000 according to the CDC (2011). Research focusing on TBI is expected to yield important results in the fields of contact sports, sports injuries, general injury mechanics, military and defense engineering, automotive safety and in general health management [1]. It is important to understand the detailed mechanical behavior of the tissue and further explore differences in the exposure of certain layers or regions of the brain in case of injury.

The key approach to assess TBI mechanism is to create a detailed model of the brain along with appropriate material modeling, and to understand in-depth sub-cranial anatomy. The essential part of the brain examined for this research is the outer shell of the human brain, the cerebral cortex, consisting of grey matter (GM). As several studies have shown, e.g. [2], [3], [4], [5], the resulting mechanical strains inside the brain, induced by a head injury, are responsible for the injury of the brain tissue on the microscale. On this basis, the mechanical response (i.e. deformation induced by stress waves) of grey matter (and even other parts of brain) to an applied dynamic load obviously depends on the viscoelastic properties and geometry (i.e. thickness) of cortex sublayers. Calculating the mechanical stretch or shear deformation at each layer is critical for studying the local damage in the cortex layer under various dynamic loadings. In addition, elastic properties and density of each layer determine the excess of load transmitted to other layers and to the white matter (WM). Namely, the transmitted dynamic force causes damage to axons in the WM and at the interface of white and grey matter [1].

With help of this research, it is approached to observe whether there is a difference in material properties between the particular grey matter layers. As a consequence, more detailed simulations could be built, and various types of mechanical behavior could be observed in different layers of the grey matter cortex, along with identification of layers which are more vulnerable, taking in account their important functions. Important is to be able to conclude particular functional damages from the exposure of certain layers to mechanical strain.

## **1.2. Objectives**

One of the aims of this research is to examine the cytological architecture (cytoarchitecture) of the grey matter neocortex in detail, by obtaining stained microscope images of brain samples, and to be able to distinguish between different layers of the neocortex.

It is intended to set up an atomic force microscopy (AFM) instrument for the purpose of conducting nanoindentation experiments on a brain sample, and thus obtaining elastic and viscoelastic material properties of different neocortical layers.

Furthermore, the outcomes of the material experiments shall be employed to build a local model containing the detailed structure of the 6 layers, and simulate results based on an existing finite element (FE) head and brain model. As a result, differences in mechanical properties and exposure to vulnerability can be compared among the layers.

## **1.3. The structure of this thesis**

This master thesis will be structured as follows: after a brief introduction about the goals of the work and the problem field which called for specific solutions making this research evolve, previous achievements in studying the field of grey matter material properties, the biological constitution of the layers, the mechanical behavior of the brain in the case of accidental injuries, and experimental studies utilizing atomic force microscopy will be introduced and discussed. Afterward, various background knowledge required for this research will be unfolded, starting with the basic anatomy of the brain and the description of the grey matter layers in detail. This will be followed by expanding on the theory of elastic and viscoelastic mechanics, and the constitutive equations in detail which are required to describe properties of biological materials, especially grey matter, and understand their mechanical behavior.

Further, the theory of atomic force microscopy and its utilization for measuring mechanical properties of materials will be introduced and explained. The introductory part of this thesis finally ends with a brief introduction to accidents and injury biomechanics to understand which kind of impacts is the head and the brain exposed to, providing the basis for injury simulations used to assess the mechanical behavior of grey matter.

In the following methodology part, the working process of sample preparation, imaging, and yielding material properties by AFM measurements will be described. The methods for sample extraction and preparation and the utilization of microscopy for extracting images for the assessment of grey matter structure will be described. Additionally, the utilization of AFM and the measurement protocols for yielding both elastic and viscoelastic properties (as different methods are used to extract the two kinds of properties) will be introduced, following by an explanation of the calculations and statistical methods required to yield the needed properties from the measurement data. This will be followed by the description of the conducted FE simulations, such as the building of the local model and analysis of the output results.

After the description of the methods utilized to conduct this research, the yielded results from the measurements, experiments and calculations will be presented. Descriptive statistics, plots, and images will be introduced, and significant gains and novelties resulting from the measurements will be presented providing plots. In the following section, the results will be discussed, with important statements helping to interpret this research considering its accuracy and significance, emphasizing the role of present study in the field of brain injury mechanics and as a basis for further studies. Suggestions will be made for further expansion of this topic. Finally, conclusions will be drawn about the achievements of this research.

## **1.4. Literature review**

### **1.4.1. Indentation measurements**

Different kinds of biological tissue samples have been examined for mechanical properties by indentation, since Oliver and Pharr [6], [7], along with subsequent contributions of Cheng et al. [8], set the basics of modern computational assessment of spherical indentation of soft materials; these papers provide important precedents and preliminary knowledge for my work.

Ebenstein et al. conducted a study on different viscoelastic plastics employing nanoindentation [9], with a subsequent study on biological structures, such as fibrous and calcified tissues [10]. Cheng et al. executed spherical indentation measurements on different soft, hydrated viscoelastic materials [11]. Since then, several kinds of biological materials have been examined by nanoindentation: mice cartilage [12], human amyloid fibrils [13], human living cells [14], human cardiomyocytes [15], porcine vocal folds [16]. Specific studies have also been conducted regarding measurement techniques and precision, comparing different cantilever stiffness and tip diameters [16], expanding on experimental errors of AFM measurements [17].

#### **1.4.2. Material models for grey and white matter**

Galford et al. already studied the viscoelasticity of the brain and different tissues of the head compartment in 1970 [18]. Since then, newer and newer approaches have been employed with the development of computational methods. Ruan et al. [19], along with Miller et al. [20] employed the Prony-series constitution of viscoelasticity for brain tissue in impact studies. Recently, the more specific hyperelastic Ogden-theory [21] for soft elastic materials has been successfully established and validated for modeling grey and white matter tissue nonlinearity [22]. It has been employed in studies of Miller et al. [23], [24], Budday et al. [25] and Kleiven et al. [4] for creating more precise brain material models. One of the most extensive studies has been conducted by Franceschini [26], who assessed all aspects of hyperelastic material modeling of the brain tissue both in theory and experimentally, and suggested a model of porous, fluid saturated, nonlinear soft solid model with small volumetric compressibility. However, establishing and employing such a complex material model is not realizable for simulations. A hyper-viscoelastic model, based on the above studies and explicitly suggested by [27], is a well-established approximation of the material behavior of grey and white matter.

#### **1.4.3. Measurement of grey and white matter properties**

On purpose of extracting parameters for the above material models, indentation measurements on grey and white matter tissues have been conducted in different studies. Assessment of brain mechanical properties mainly focused on the difference between GM and WM material properties, in rat cerebellum [28], bovine brain [29], porcine brain [30], [31] and human cadaveric brain [25], [32], where Finan et al. [32] additionally examined regional variability and Qian et al. [25] focused on variability depending on different indenter velocities.

The most recent technique for measuring viscoelastic properties is employing magnetic resonance elastography. One of the first studies in this field was published by Green et al. in 2008 [33], followed by more specific researches by Freimann et al. [34], Klein et al. [35], Murphy et al. [36] and Hiscox et al. [37]. Despite the enormous advantage of possible *in vivo* examinations, this method still has considerable limitations, as no distinction between different regions, or between grey and white matter can be made on the macro- or microscale.

#### **1.4.4. Cellular constitution of the neocortex**

Although the different layers of the neocortex have not been evaluated in previous studies regarding microscale mechanical properties, it has been well known since the works of Brodmann (1909) [38] and Vogt (1910) [39], [40], who described and mapped the tissue structure of the layers first in detail, that there are remarkable differences in the cytoarchitecture and myeloarchitecture (arrangement of dendrites and axons) of the neocortical GM between layers and between different regions. The first detailed study and map regarding the myeloarchitecture of the brain were published by Vogt [39], followed by several detailed studies from the Vogt school [40], [41]. Meanwhile, Brodmann studied the cytological architecture of the brain and divided it into functional areas based on the density, shape, and distribution of cells, defining the layered structure of the grey matter [38]. Cecile and Oscar Vogt studied the connection between architectonics and functionalities of the brain (1919). Following their path but already using modern technology, Zilles and Amunts conducted a more extensive research on the architectonic mapping of the brain [42], along with Schleicher et al. [43]–[45], who distinguished between functional areas based on their in-depth tissue architecture [46]. Palomero and Zilles used different special methods to assess cyto- and myeloarchitecture, and receptor density in different regions of the neocortex [47].

Holtzmann et al. examined the effect of CO<sub>2</sub> overdose on the stiffness of harvested brain tissue, gaining important prospective knowledge regarding the condition of the cellular network and its relation to mechanical stiffness [48]. Likewise, Freimann et al. [34] and Klein et al. [35] studied the effect of neurogeneration and degeneration due to different pathologies on the mechanical strength of the cellular network, also providing important preliminary knowledge.

### **1.4.5. Functionality of layers**

A more detailed assessment of the cellular structure of the neocortex has been executed by Huttenlocher et al. [49] and Thomson et al. [50], who examined functionality based on pyramidal cell density, neuronal density and connectivity, and created schematic functional maps based on the cytoarchitecture and connectivity of pyramidal cells and interneurons. These researches provide important input to the structural differences of grey matter layers.

### **1.4.6. Studying of accidental injuries of the head**

Nahum et al. [51], Zhang et al. [52], Hardy et al. [53], and Kleiven et al. [4] provided the basis of head model establishments and simulation of accidental injuries. Additionally, several more detailed *in silico* simulations have been built (e.g. [54]) to study the exposure of different brain regions to mechanical stresses and strains in the case of certain head impacts. A considerable effort has been made to apply important mechanical measures such as strain state or acceleration as predictors to assess injury criteria [2], [5]. Additionally, Saboori et al. examined the effect of the subcranial architecture (meninges) on the mitigation of brain injury in detail [55]–[57].

## **2. Anatomy and Histology**

### **2.1. Brain**

The human brain is the most important organ of the Central Nervous System (CNS), being in control of the sensory, motoric and information handling functions. The building bricks of the brain on the cellular level are as much as 100 billion neurons and 10-50 trillion neuroglia [58].

The brain is located in the skull (cranium). Inferiorly, through the brain stem, it extends into the spinal cord from which it evolved by protruding into the cranium. The spinal cord and the brain together build the CNS [58]. As it is pointed out in [58], “*The CNS processes many different kinds of incoming sensory information. It is also the source of thoughts, emotions, and memories. Most signals that stimulate muscles to contract and glands to secrete originate in the CNS, specifically in the brain.*” (p. 454).



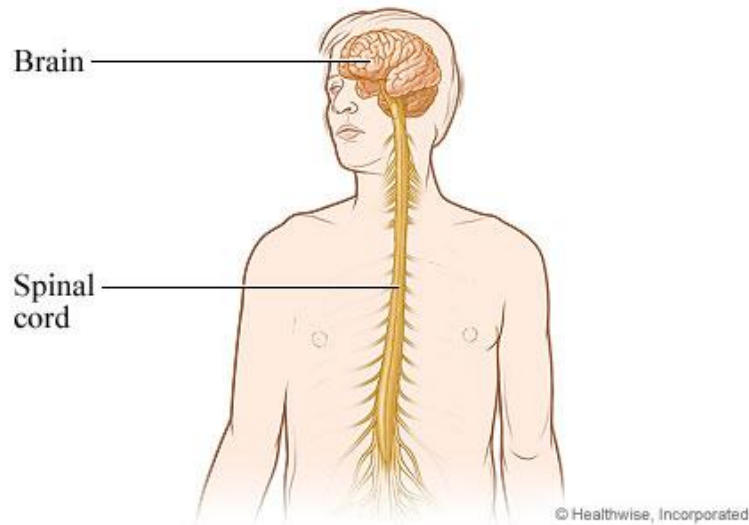


Figure 1: Organization of the central nervous system (Source: myhealth.alberta.ca)

### 2.1.1. The function of the brain

The human brain has an essential function in the CNS, as the central unit of all the intellectual and emotional information flow and storage (memory). As discussed later on, different regions and parts of the brain are responsible for different particular functions, acting in synchrony, controlling the body [60].

### 2.1.2. Structural and mechanical properties

The weight of the brain varies around 1300 – 1500 g depending on sex, age and other factors such as diseases. The volume of brain tissue (GM and WM) inside the head compartment shows a likewise variation due to age and sex, between 1200 – 1500 cm<sup>3</sup>, filling almost the total intracranial volume of 1400 – 1600 cm<sup>3</sup>. The rest of the volume is filled by the subcranial structures between the skull and outer rim of the brain as well as the ventricles inside the brain [61], [62], [63], [64].

The head with the brain inside can be depicted as a multi-layered structure, starting with the scalp (5 – 7 mm) on the outer surface of the cranium (hair-bearing skin, subcutaneous connective tissue, muscle, and fascial layer), followed by the loose connective tissue, periosteum, and the cranium (skull) itself, an external capsule of bone, which provides fixation, stability and mechanical protection [1].

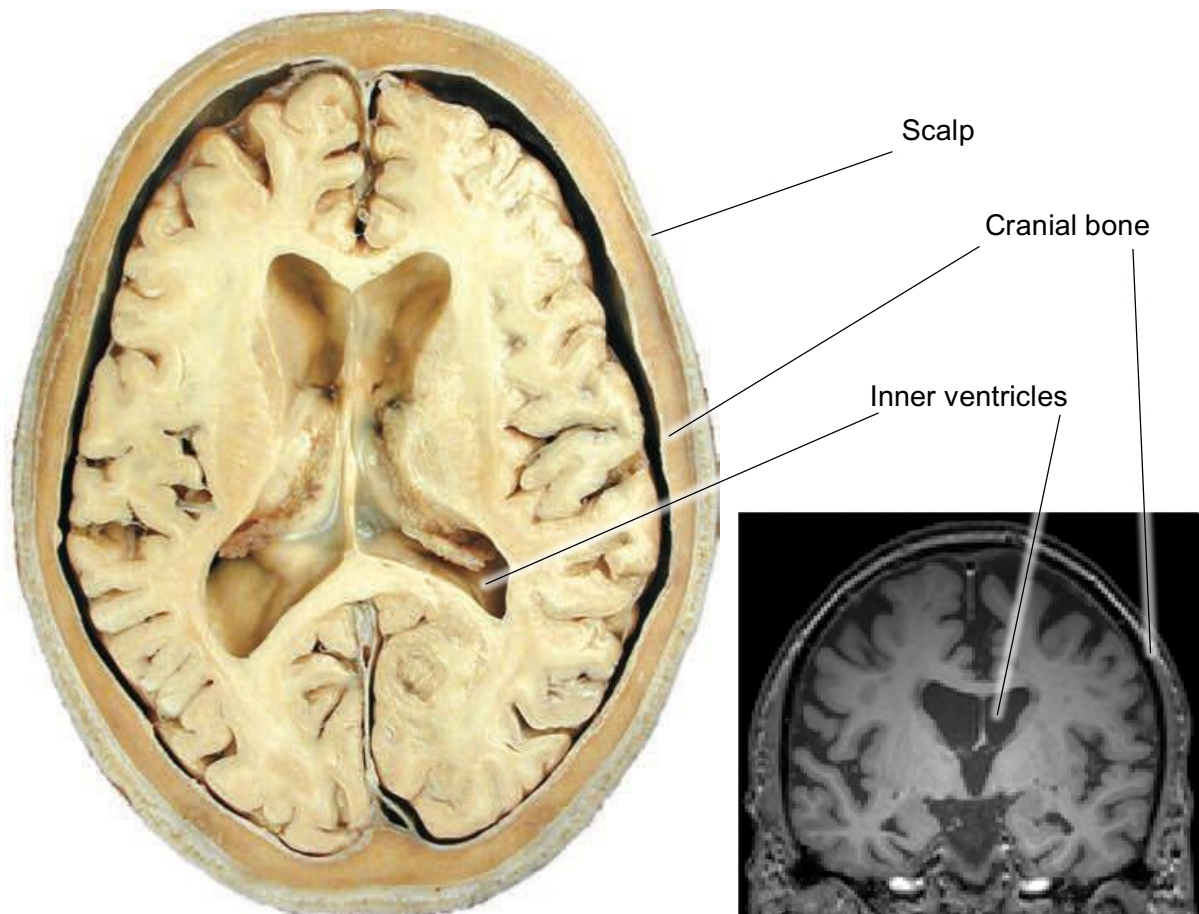


*Figure 2: left, superior view of transverse section of brain, showing the ventricles inside the brain as well as the space between the brain and skull [59]; right, coronal view of the head compartment on an MR image, used to approximate volume [125].*

The gap between the brain and the cranium is filled by a layered structure of fibrous connective tissue (meninges) which account for the mechanical protection (damping). The meninges consist of the dura mater, a doubled connective tissue layer on the inner surface of the skull, the arachnoid layer, built by strands of collagen-rich tissue, separated by a thin subdural space from the dura mater; and the pia mater tightly covering the surface of the brain cortex (Figure 3). The space between the arachnoid and pia mater, known as the subarachnoid space (SAS), is filled with cerebrospinal fluid (CSF), with abundant bridges of collagen pillars reaching from the arachnoid layer into the pia mater [56]. CSF is a liquid with high water content, continuously circulating through the cavities of the brain, the ventricular system [59]. The meningeal structure, embedded in CSF which the brain floats in, along with the capsuling bone of the cranium, act and support together as a shock absorber for mechanical loading in rapid movements of the head [55].

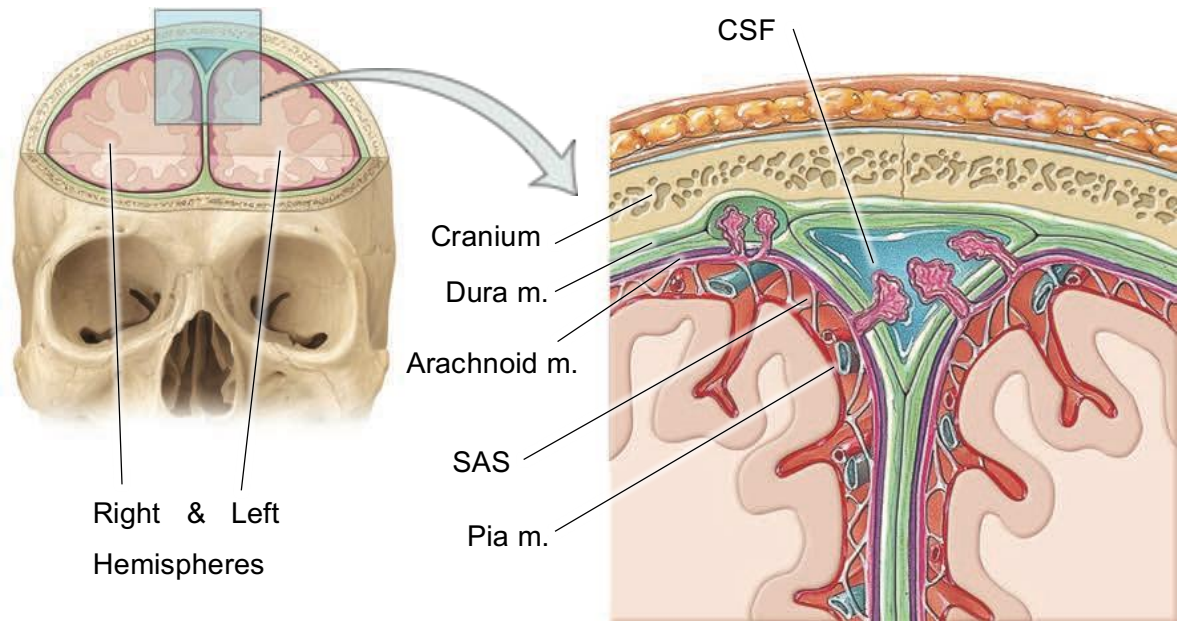


Figure 3: Subcranial architecture of the brain in detail [59].

On the macroscale, the brain is divided into the cerebrum, brainstem, and cerebellum. The term cerebrum is generally used to include the paired cerebral hemispheres and the diencephalon (between brain) (Figure 4) [59].

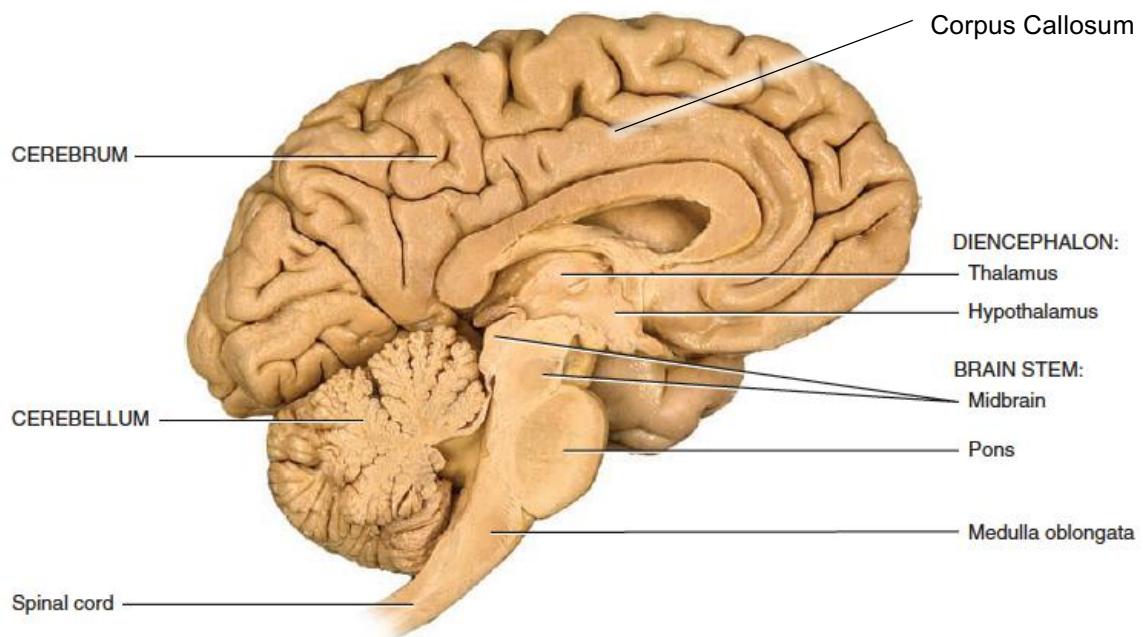


Figure 4: Main structural parts of the human brain [59].

### 2.1.3. Cerebrum

From the three structural parts of the brain on the macroscale, the cerebrum is the part containing this work's areas of focus. The cerebrum comprised of the paired cerebral hemispheres (Figure 3), and the diencephalon [58]. The cerebral hemispheres consist of the cerebral cortex, built mostly by GM tissue [58], which will be our primary field of investigation. A voluminous mass of internal white matter lies under the cerebral cortex. The corpus callosum, consisting of fibrous WM, connects the cortices of the two hemispheres as a commissure (Figure 4) [58]. The cerebral grey and white matter is essentially built of neurons, nerve fibers, and neuroglia. Their detailed constitution is discussed in the following chapters.

## 2.2. The cerebral cortex

The cerebral cortex comprises the outer shell of the cerebrum, representing about 40% of the brain by weight. It consists of a convoluted structure of grey matter, at a thickness of 2 – 4 mm. 90% of the cerebral cortex comprises of neocortex in today's humans. The neocortex is the embryonically most recent evolvement of the cortex, which, excessively enlarged, distinguishes higher mammals, such as today's humans from our ancestors, providing the capacity of problem-solving and rational thinking. The neocortex comprises of GM arranged remarkably in a layered structure [59].

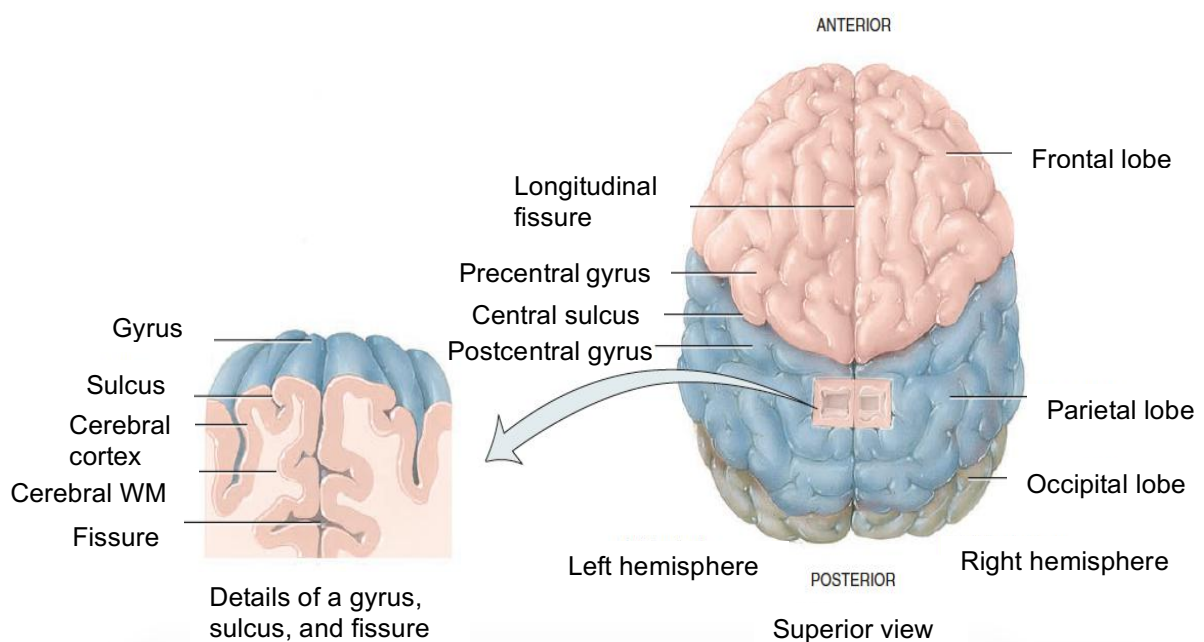


Figure 5: Structure of gyri and sulci of the cortex [59].

As it is described in [59], “*During embryonic development, when brain size increases rapidly, the grey matter of the cortex enlarges much faster than the deeper white matter. As a result, the cortical region rolls and folds on itself.*” (p. 547). The convoluted structure of the neocortex create ridges called gyri (s. gyrus), and grooves called sulci (s. sulcus). A deep, distinct sulcus is called a fissure. The sulci and fissures divide the neocortex into four major lobes: the frontal, temporal, occipital, and parietal lobe (Figure 5) [59]. Our research is executed on a sample from the frontal lobe [59].

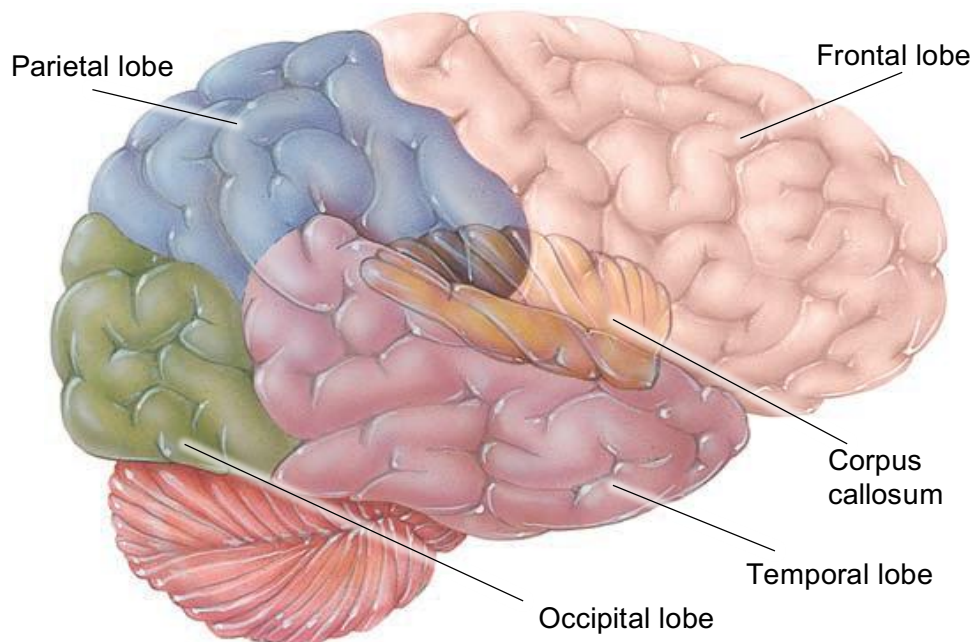


Figure 6: Lobes of the cortex [59].

The cortex can be further divided into functional areas, after Brodmann [38]. Based on Brodmann’s representation, our area of focus lies on the prefrontal cortex (Figure 7). As it is pointed out in [59], “*The prefrontal cortex (frontal association area) is an extensive area in the anterior portion of the frontal lobe that is well developed in primates, especially humans...*” (p. 554). It is explained in [59] that “*The prefrontal cortex is concerned with the makeup of a person’s personality, intellect, complex learning abilities, recall of information, initiative, judgment, foresight, reasoning, conscience, intuition, mood, planning for the future, and development of abstract ideas*” (p. 554).

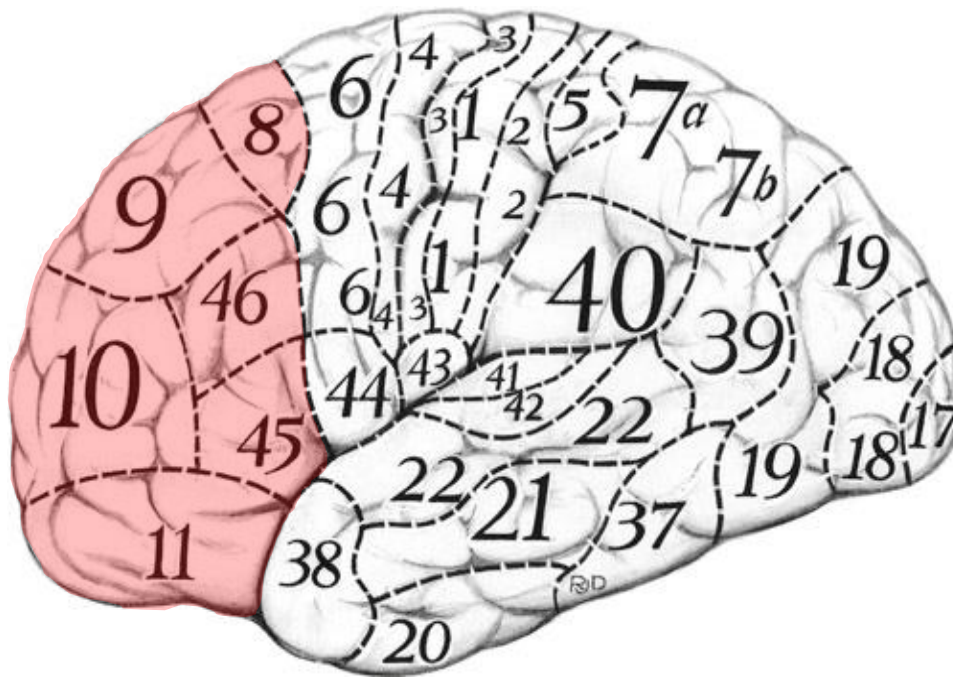
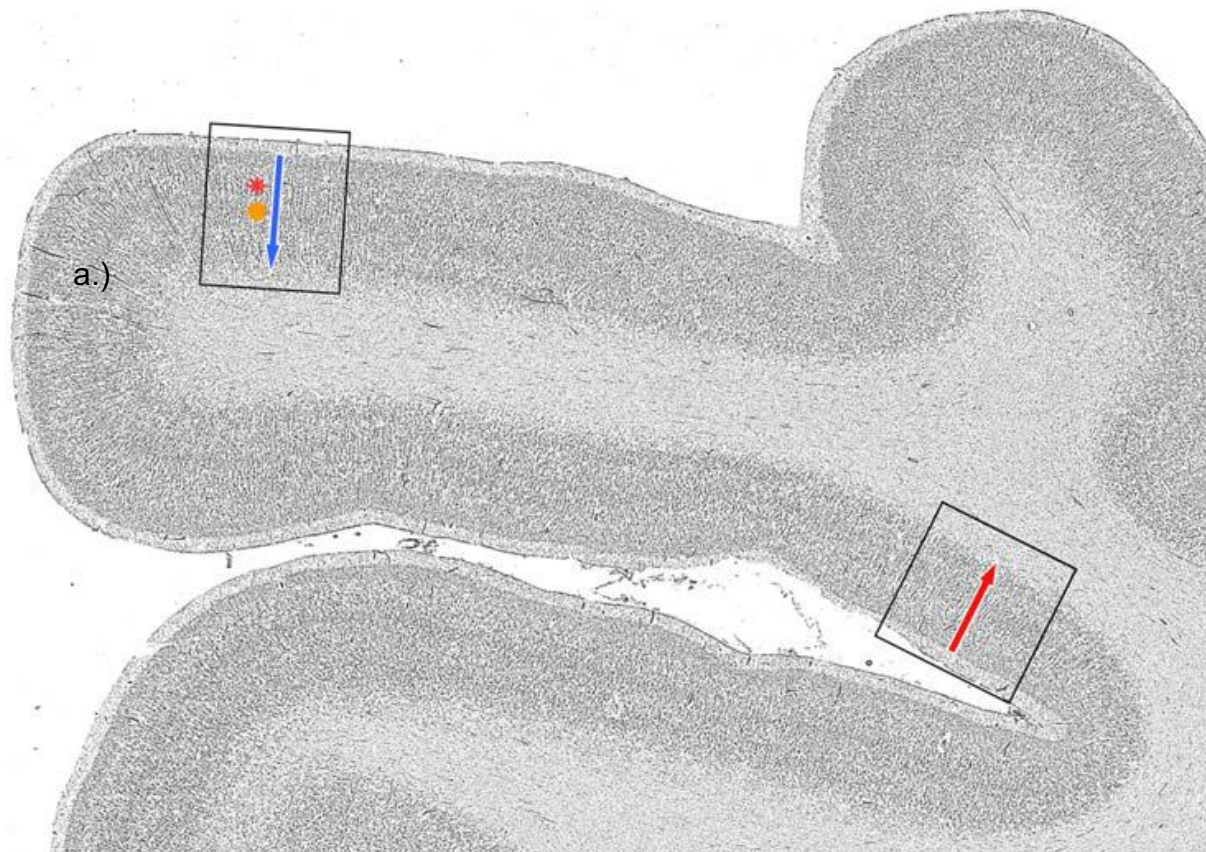


Figure 7: Lateral surface of the cerebral cortex of the left hemisphere, Brodmann's areas indicated by numbers [58]. Prefrontal area additionally outlined with red

### 2.3. Constitution of GM and WM

While white matter is composed mostly of neurons having myelinated axons (which provide the whitish color), grey matter mostly contains unmyelinated axons and dendritic branches. The darker, grey color of the tissue is caused by the presence of a significantly higher amount of cell nuclei [59]. Pertaining GM consistency and integrity is critical: it has been proven that a significant loss of GM occurs with age [65]. Additionally, cortical GM and WM, is more exposed to higher, more concentrated loads; the resulting strain concentration in the sulci regions can be correlated with neuronal degeneration [66]. The underlying mass of WM, especially in the corpus callosum, is rather in danger of neuronal disruption due to rotational accelerations [2].

The most conspicuous structural feature of the grey matter neocortex is its organization into layers which are oriented parallel to the surface. This organization has been first studied by pioneers Vogt [39] and Brodmann [38], who created structural and functional maps of the brain based on the constitution of the neocortex. They indicated layers based on their cyto- and myeloarchitecture with Roman numerals. They also distinguished different functional regions of the neocortex, based on the layered structure, indicated by Arabic numerals [38], [39].



b.)

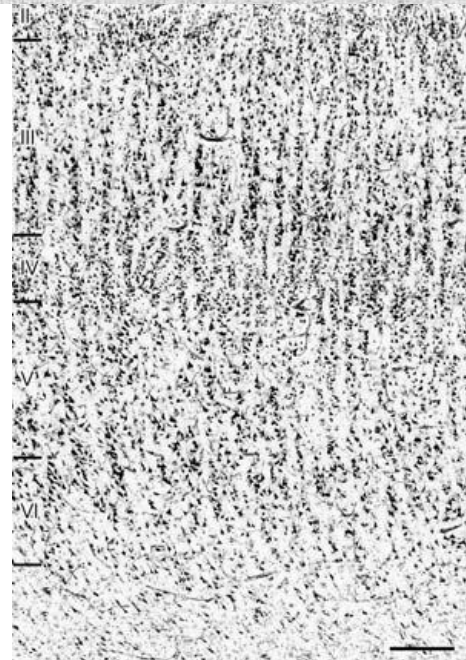


*Figure 8: a.) A histological section through the cortex surrounding the superior temporal sulcus. Arrows indicate the depth of the GM neocortex, starting from the pia mater. Point of the arrows indicate the start of white matter [45].*

*b.) a magnified microscopical image of the cytoarchitecture of the neocortical layers Roman numerals indicate the layers starting from the pia mater [45].*

### **2.3.1. Layers of the GM neocortex**

A laminated organization of the cortical neuronal tissue can be observed in almost all vertebrates. Nevertheless, the mammalian neocortex has evolved to a much more sophisticated and elaborated architecture, having at least 6, but often 9-10 distinguishable laminae [67].

The most important feature of the mammalian neocortex is the prevalence of the so-called pyramidal neurons. These are to be found exclusively in mammals, and it has been proven, that their presence corresponds to the cognitive abilities of humans. Their organization in the laminated structure is essential to understand brain function in different areas [68]. The laminated structure results from the varying density of cell nuclei (cytoarchitecture) as well as from the varying density of neural network (myeloarchitecture) across the cortex [60].

The laminated architecture and neural constitution vary additionally among different regions of the cortex. To be able to identify and describe layers all around the cortex, a nomenclature has been introduced by Brodmann (1909), using Roman numerals directly corresponding to each specific type of layers. The layers are named after their cellular constitution, and numbered starting from the pia mater, across the depth until white matter [38]:

- I. Molecular; containing axon terminals building a plate of branches
- II. External granular; containing only smaller, non-pyramidal cells
- III. External pyramidal; pyramidal cells prevail, along with other cells
- IV. Internal granular; only non-pyramidal cells and a dense myelin band
- V. Internal pyramidal; sparsely populated large pyramidal cells and myelin band
- VI. Multi-form; various neuron types along with large pyramidal cells

On Figure 9, the detailed cyto- and myeloarchitecture are shown, with some remarkable features of particular layers. Each layer is characterized by its cellular constitution which also determines their function. The hypothesis of this study is that the material properties of the neocortex change across the layers of GM due to the histological differences. The basis for this assumption is given by numerous studies (e.g. [29]) which have proven that material properties of GM and WM differ from each other, along with demonstrated differences of GM and WM material properties of different regions of the brain (e.g. [32]), based on histological variations.

## **2.4. Neuronal architecture**

The cytological and structural organization of the layers correspond to their specific function in the mammalian neocortex. Each layer has its particular connectivity through terminating neurons from other layers and from the white matter, as well as through having origins of efferent neurons projecting towards other layers and parts of the brain.



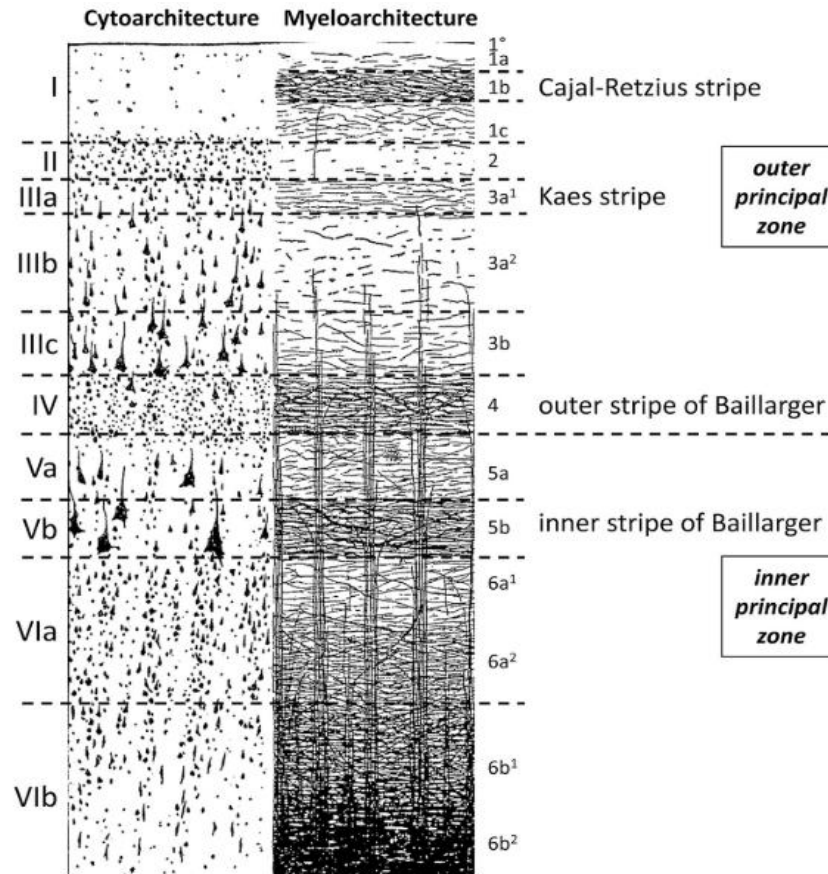


Figure 9: Cyto- and myeloarchitecture of cortical layers. Myeloarchitectonic features highlighted on the right [69]

The complex structure and functionality are realized by an interaction and collaboration of various types of cells having a defined function. Neurons and neuroglia represent the basic unit of the nervous tissue. Neurons have the essential functional role of transferring information, and building networks, glia have a structural and biological supporting function, e.g. building the myelin sheath of axons, nourishment, and chemical protection. The neuron is a highly specific type of cells, capable of conducting electric action potentials along the membrane of its cellular processes (dendrites, axons) to transfer information [59].

Neurons excite each other by transferring action potentials across synapses, building a network of information flow, along with transferring excitation and information to other types of cells e.g. muscle cells, executing a controlling function. The neuronal cell body (soma) comprises of the regular cell constituents similar to other cell types; a nucleus and basic functional organelles, membrane, and cytoplasm. The soma can reach a size from 5 to 135  $\mu m$ .

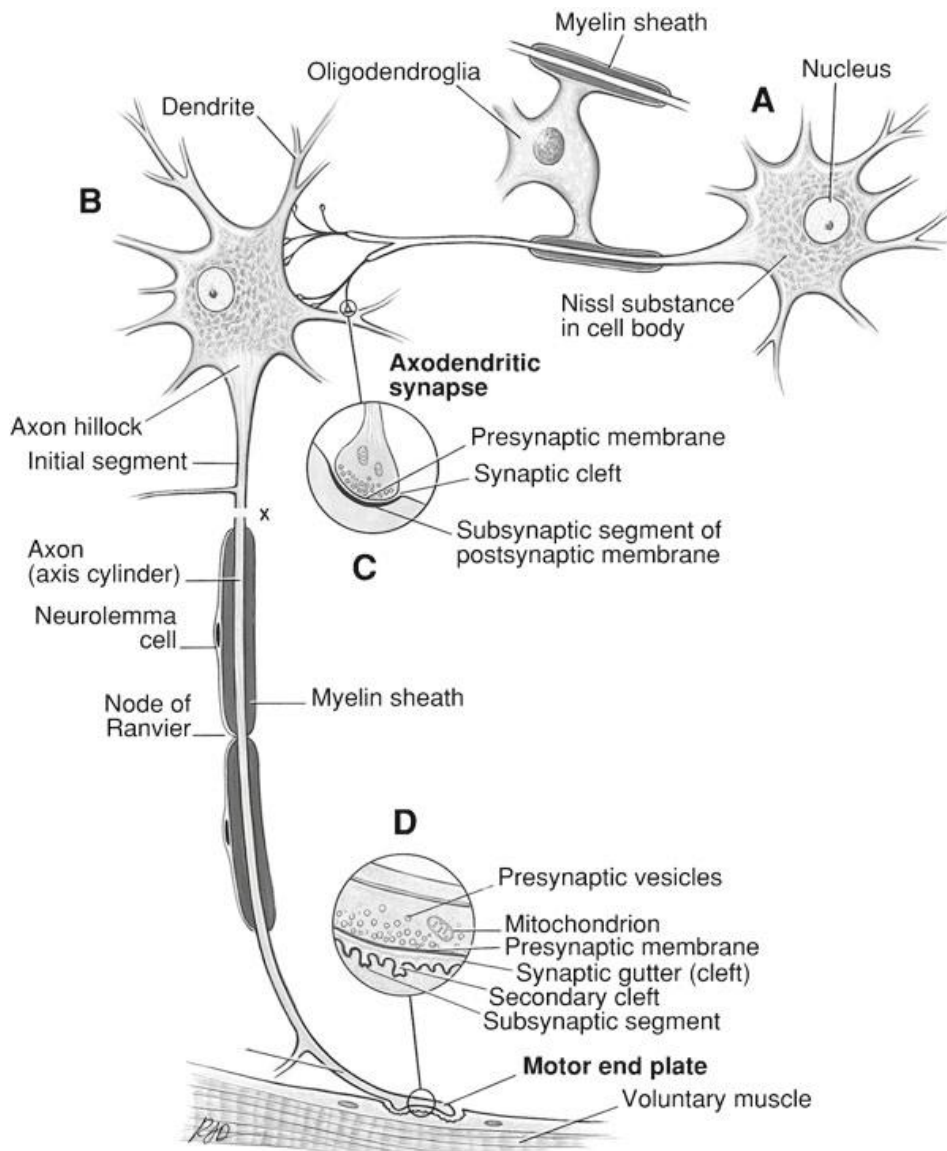


Figure 10: Neuron, with receiving synapse, connecting to a muscle [58]

Additionally, unlike other cell types, the cell forms elongated, thin, cylindrical processes: one single axon, and several dendrites, which propagate potentials towards other cells and make an excessive branching and connectivity possible. Axons reach a length of several centimeters. The cytoskeleton of neurons provides mechanical support to the processes and the soma, and provides the mechanical strength of the cell, with the help of microtubules [58].

Neurons establish connections within the neural network and to other cells by synapses, which are the receiving or input portions of a neuron. The contact sites or synapses between two neurons can be locally distinguished as axon-soma, axon-dendrite, or axon-axon contacts. Neuronal axons in bundles build nerves which transport and reach with information into distant parts and of the body through the spinal cord (peripheral nerves) [58].

The prevailing neuronal cell types of the neocortex are pyramidal, and granular (non-pyramidal) cells, characterized by the shape of their cell body, and dendritic organization. Pyramidal cells, present in all layers but the first, constitute the majority of cortical neurons [58].

The most important glial cells of the cortex are astrocytes. Although they are 5-25 times smaller than neuronal cells, they are present in a higher number. They are characterized by short branched processes reaching and connecting different functional units (vessels, neurons, other cells). Their microfilaments provide a stiff mechanical structure, maintaining the chemical and biological environment where neurons can exert their function well [59].

An overview of the neuronal constitution of the neocortex is provided in Appendix A.

### **2.4.1. Pyramidal neurons**

Pyramidal neurons are present in all mammals being the most numerous excitatory cell type, and the predominant cell type in layers II, III, and V [58] of the neocortex. Especially, in the superior middle frontal gyrus, pyramidal cell size is approximately  $300 \mu\text{m}^2$  [70], implying an estimated diameter of  $17 - 20 \mu\text{m}$ . The diameter of rat pyramidal processes range from  $0.8 - 3.2 \mu\text{m}$  according to Nevian et al. [71], whereas human pyramidal axons (of myelinated sensory neurons) can reach a diameter of  $20 \mu\text{m}$ . The length of the processes can range from  $1 \text{ mm}$  up to several centimeters, reaching to other regions of the brain [58].

Pyramidal neurons, unlike other neurons, are characterized by two distinct dendritic trees: several basal dendrites emerge from the base, and apical dendrites from the apex of the soma. Collateral branches of dendrites run across the cortical thickness and terminate at the first layer, except for layer VI pyramidal neurons, which do not reach layer I. The extensive branching of dendritic trees allows a single neuron to communicate with thousands of other neurons [58].

Pyramidal cell nuclei are present in all layers except I (terminating axons, but no soma). Layer II/III pyramidal neurons branch extensively both in layers II and IV, whereas Layer V neurons do not have significant branches in neighboring layers [72]. These findings might be important to understand the pattern of the density of neural network through the cortical depth, implying eventual correlations to material properties.

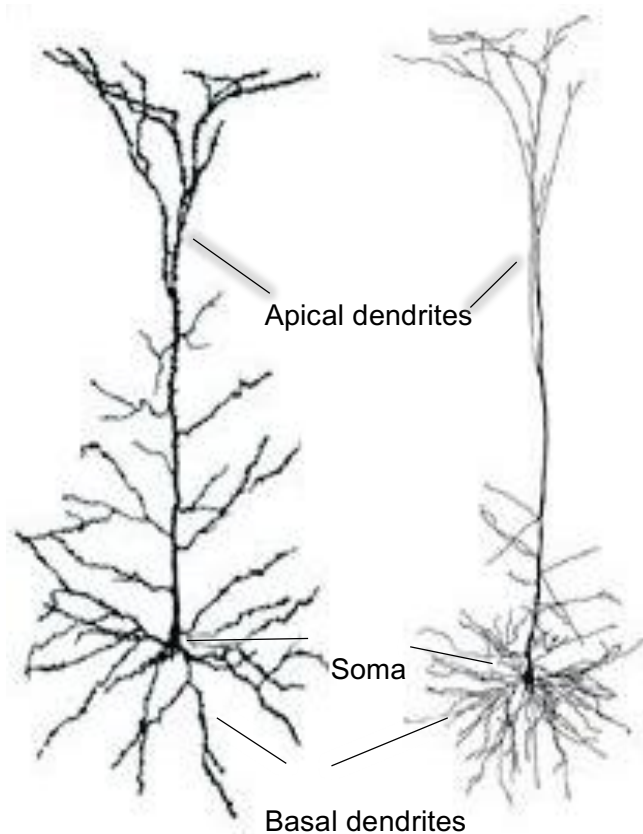


Figure 11: Images of real pyramidal neurons of cortical layer II/III (left) and V (right) [126]

### 3. Head biomechanics

This thesis is written on a research conducted in the field of head injuries, aiming to predict and better assess the outcome and severity of brain tissue injuries. Thus, it is important to expand knowledge about accidental injuries and specifically expand on head impacts.

#### 3.1. Head injuries

The most important and also most critical injuries are those sustained by the nervous tissue in the human brain, caused by displacement and distortion of the neural tissue. For the connections and the specific network between nerve cells cannot regenerate the way other cells (muscle, epithelial cells) can, brain injuries are among the most severe injuries [59]. As brain injuries commonly occur due to head trauma, it is important to excessively study the injuries and the protection of the nervous tissue in the head compartment.

Among the types of head injuries, an open injury, where the dura mater is affected, is distinguished from a closed one where the dura mater remains intact. Regarding the injury of

the brain, a diffuse injury is not concentrated in one location, as it is in the case of the neural disruption in the white matter. A focal injury on the other hand is focused to a well-defined location, resulting in hematomas and contusions inside the cranium. A hematoma is a bleeding due to the rupture of one or more blood vessels. Three different types are distinguished, epidural (above dura mater), subdural (in the subdural space, rupture of e.g. cortical or bridging veins), and intracerebral (blood inclusion in a sulcus or inside the cerebral nervous tissue) [1].

The brain injuries on which this study concentrates are closed focal head injuries (no penetration of the cranium) caused predominantly by dynamic loadings, under a duration of 200 *ms*. Focal injuries occur at the site of impact (coup injury), with neurological damage localized to that area [1]. This can occur wherever force is transmitted through the skull, mostly in the anterior-posterior direction [73]. Along with the coup, a countercoup injury occurs at the opposite side of the brain to the impact, in the line of the load vector [1].

Non-contact injuries are caused by pressure and stress differences (tensile/compressive loads) inside the brain tissue caused by sudden translational and angular acceleration/deceleration of the head. Apart from that, the relative motion of the brain with respect to the skull can not only result in contusions on the cortex, but also cell damage if the inner surface of the skull is hit. If there is a significant rotational component in acceleration, tissue structures will torque and twist, and thus shearing can occur. This results in diffuse axonal injury (DAI), which is one of the most severe outcomes of a traumatic brain injury (TBI) and leads to coma in most cases [1]. Often the exact site of occurrence of the injury is unknown and therefore the treatment and prevention of complications are difficult. That is why it is important to better understand and more precisely simulate these types of injuries by building detailed models and understanding behavior of different tissues, to be able to assess the consequences of different types of impacts.

### **3.2. Traumatic brain injury**

Traumatic brain injury occurs by definition when a mechanical impact of the head leads to a pathological condition of the brain. These head impacts mostly occur due to traffic or other accidents, and assaults. TBI accounts for very high annual costs of medical care (est. \$50 billion), along with the greatest number of years lived with disabilities resulting from a trauma. Intangible costs due to a TBI event are remarkable as well, such as the long-term loss of productivity [73].

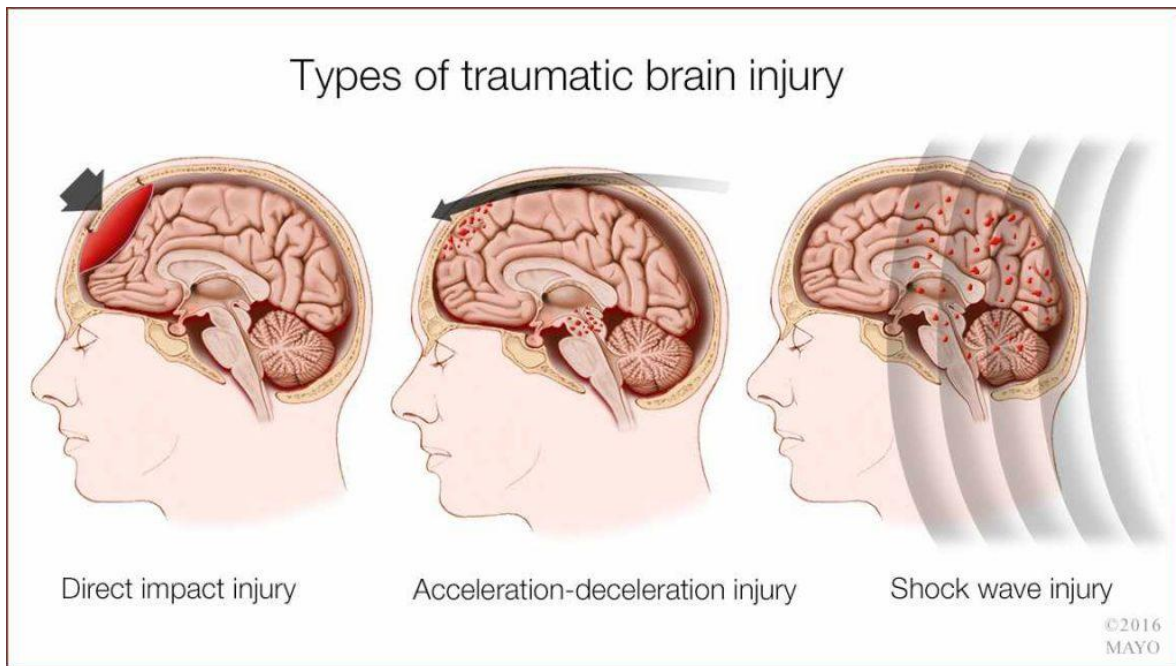


Figure 12: Types of head impacts leading to TBI. source: [www.mayoclinic.org](http://www.mayoclinic.org)

An estimated 1.7 million TBI events occur annually in the US, representing a considerable health issue. Of all the injury-related deaths in the United States, TBI was a contributing factor 30.5% of the time. The reason for TBI is fall related at the first place, followed by injuries resulting from strikes and traffic accidents. Falls prevail in children and the elderly, whereas traffic accidents prevail in the age group of young adults [74].

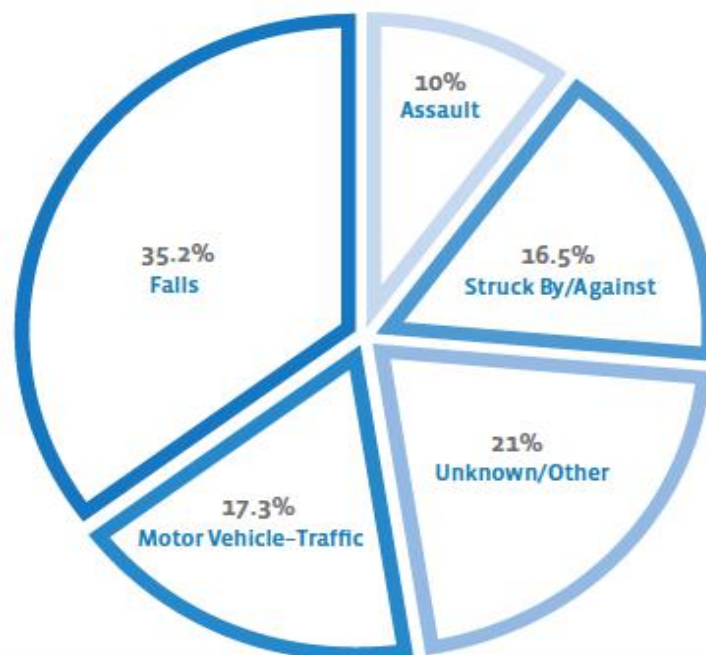


Figure 13: Estimated average percentage of annual TBI-combined emergency visits, hospitalizations and death by external cause, US 2002-2006 [74].

The most frequent type of TBI is mild Traumatic Brain Injury (mTBI): it is a complex pathophysiologic process induced by a mechanical impact. Its hazard lies less in the primary acute injury and resulting symptoms (short time loss of consciousness, impaired brain functions), from which the patient usually recovers fast, in a few days. Secondary effects are more dangerous, as they often occur days or even weeks after a mTBI event, while patients are unaware of the dangers in most cases. If not carefully treated, a mTBI through its secondary effects can induce despaired thinking abilities, emotional disturbances, memory loss and other chronic neuronal diseases which are irreversible. This is due to the dysfunction of the cells and the unregulated biochemical environment following the injury, including changes and fluctuations in the intracranial pressure and brain arterial pressure [73].

Along with traffic accidents, the other major source of accidental head injuries is sports-related accidents. Depending on the type of sport, the prevalence of head injury varies strongly. There are particular sports where mTBI is a major issue, such as football, handball, or boxing [1]. These are mostly mild injuries (no loss of consciousness), though, when occurring repeatedly, mTBI individuals often suffer from severe long-term consequences, if left untreated. Brain degeneration diseases can be induced, such as chronic traumatic encephalopathy (CTE). CTE is a disease for which awareness just have been raised recently, as the occurrence of mental disorders among professional football players in the USA has been increasing, which suggested a correlation between frequent head impacts and degenerative disorders of the brain (GM loss). Since then, several studies have provided proof for this correlation [66], [75]–[77]. Additionally, it has been shown that the excess of neural degeneration is higher in the sulci regions, where the strain is reportedly greater at the time of injury [66]. While the primary effects of a mTBI damage cannot be treated yet, secondary effects can be monitored and treated in the long term, focusing on minimizing secondary brain injury, by maintaining and controlling a healthy intracranial environment, especially the intracranial pressure (ICP) (chemically, pharmacologically, by pressure evacuation methods/craniotomy), and oxygenation levels [73].

### **3.3. Trauma biomechanics**

Injuries are a major source of health deficit implying several indirect problems in everyday life and society such as in productivity, causing high legal and medical expenses. While any damage caused by a chronic long-time exposure to an adverse influence, such as high workloads is considered to be an injury, a major source of unintentional injuries are unexpected singular

events: accidents (intentional injuries are suicidal or criminal acts or battlefield events). Accidents, specifically traffic related, are the leading cause of premature death in the US, and the 5<sup>th</sup> cause of death among all ages. Yearly 1.2 million die, 50 million get injured (WHO) [1].

It is very important to understand how accidental injuries happen due to different circumstances, to be able to take preventive measures and gain knowledge about specific treatment methods. Concerning the fact that most accidental injuries are sustained in connection with motion, injury mechanisms can be studied with the discipline of biomechanics, and understood better. Accidents are sudden events, a mechanical exposure duration is a fraction of a second, and human defensive reaction is often delayed. Thus, it is very important to assess, how the energy gets dissipated, and how the human body is exposed to a mechanical load. Cadaveric studies as well as *in silico* simulation of computational models play an important role in this regard [1].

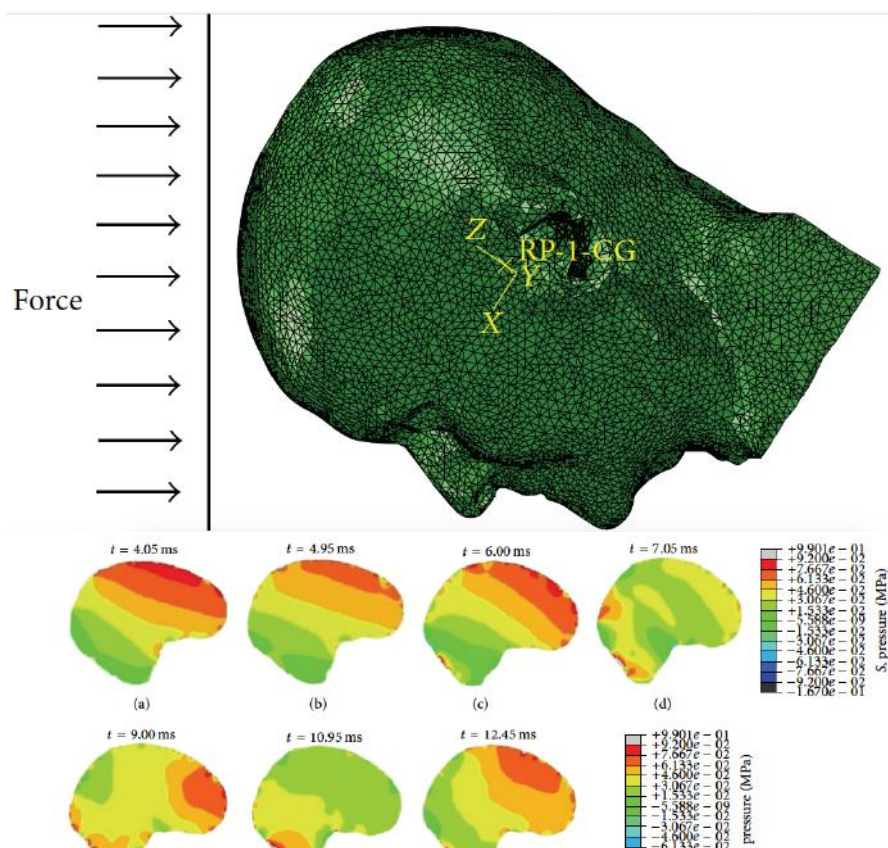


Figure 14: FE model of an impacted head by Yang et al., and resulting stress states over time [54]

With the help of these experiments, specific traumatic events can be reconstructed and analyzed, gaining important future knowledge for prevention and treatment. To be able to develop preventive measures, the identification of injury risks is crucial. After statistical assessment, defensive and preventive structures, mechanisms, protocols can be developed, as



well as appropriate safety equipment can be constructed. Tests and studies are conducted either in a simulation environment, e.g. by applying Finite Element Methods (FEM), or in experimental environment, employing standardized test procedures, set by regulations of the UN Economic Commission Europe or Federal Motor Vehicle Safety Standards USA. These tests mostly involve modeling the motion of the body in traffic accident situations [1].

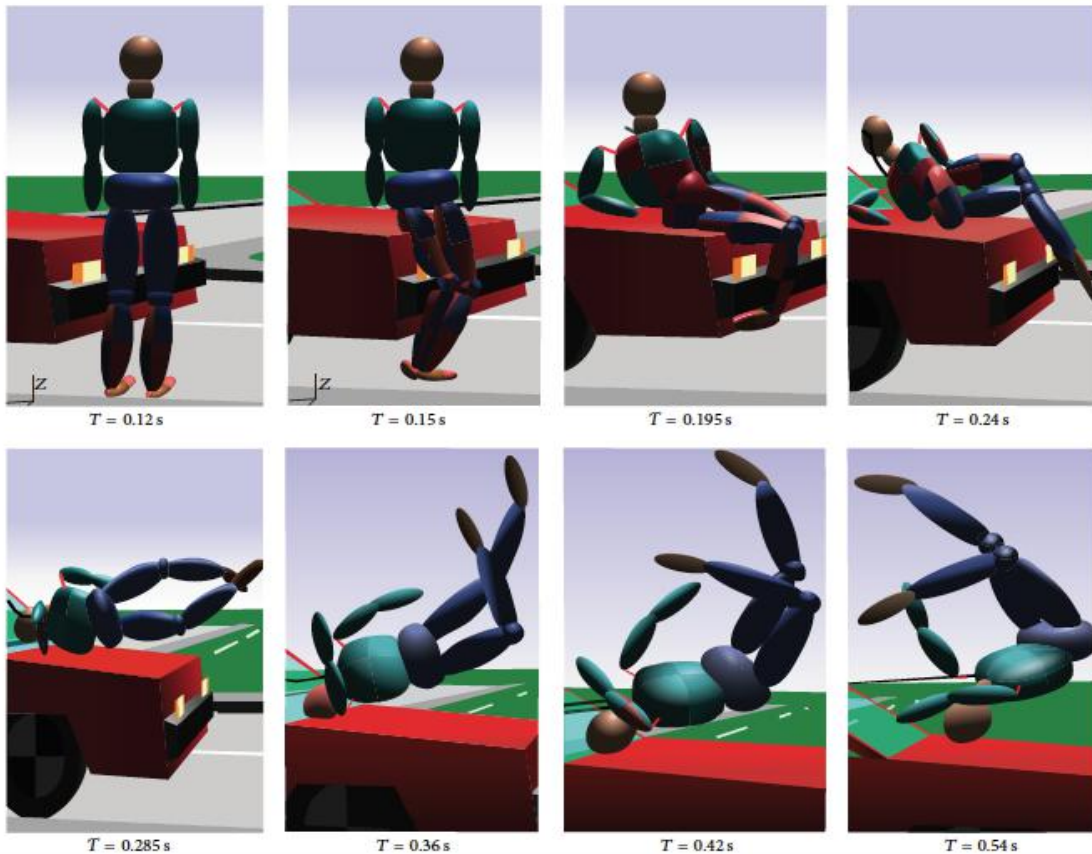


Figure 15: Schematic simulation of the kinematic model of a pedestrian hit by a car [54]

The basic environment of biomechanics is defined by rigid body as well as by continuum mechanics. Rigid body mechanics study the movement (kinematics) and the effect of forces acting on the body (dynamics). If combined, both disciplines establish the field of kinetics, the movement of bodies induced by acting external forces. Basic quantities of kinetics include mass ( $m [kg]$ ), time ( $t [s]$ ), position ( $r [m]$ ), inertia ( $I [kg \cdot m^2]$ ) and angular velocity ( $\omega [1/s]$ ) [1]. A rigid body system can be described by a finite number of differential equations, resulting from the two principal equations of equilibrium applied to each member of the system, eventually applied in the form after Lagrange [1]:

$$m \cdot \frac{d^2}{dt^2} \vec{r}(t) = \sum_i \vec{F}_i(t) \quad (1)$$

$$I \cdot \frac{d}{dt} \vec{\omega}(t) = \sum_i \vec{M}_i(t) \quad (2)$$

Where  $\vec{F}_i(t)$  are forces,  $\vec{M}_i(t)$  momentums acting on a body. In the case of deformable solids observed as a continuum, with basic the quantities velocity ( $v(t, r)$  [ $m/s$ ]), and mass density ( $\rho(r, t)$  [ $kg/m^3$ ]) following kinetic equilibrium is implied from the basic conservation and equilibrium principles of continuum mechanics [1]:

$$\int \underline{s} dA + \int \rho_0 \underline{b} dV = \frac{d}{dt} \int \rho_0 \underline{v} dV \quad (3)$$

With stress tensor  $\underline{s}$  in every point integrated over the surface  $A$ , vector of internal body forces  $\underline{b}$  and velocity field  $\underline{v}$  integrated over the volume  $V$  of any sub-region. Both approaches are essential for this research as well, whereas the focus lies mainly on continuum mechanics of deformable solids, concerning material equations and stress/strains states of the brain tissue as a continuum. Continuum mechanics deals with the behavior of deformable masses, materials, stresses strains in a field (density, velocity, location vector field) resulting in nonlinear relationships. A system in continuum mechanics has infinite numbers of degrees of freedom (DoF): every point in the mass has to be described. Therefore, discrimination of the problem is employed to get finite elements and to be able to obtain solutions with numerical methods [1].

Numerical methods, thanks to today's computational advancement, are more and more effectively used. More detailed simulations can be made because the computational effort gets smaller with high-performance processors and supercomputers. The discretized representation model of a continuous system can thus be analyzed. Also, with the help of advanced imaging systems, MRI and CT, it is possible to acquire accurate 3D models of the human body. The FEM applies a finite number of discrete elements (e.g. hexahedrons, tetrahedrons) to comprise and approximate the desired geometry of the continuum. This yields a finite DoF implied by the number of nodes, as well as finite equations to describe the system.

Several measures which describe the system are computed as a result, e.g. the stress and strain distribution. In the case of a dynamic simulation, these can be followed through time history [1].

### 3.4. Head impact mechanics

Impacts have been simulated by several researchers, experimentally with drop head studies [51], [53], or *in silico* [4], [54], [78], [79]. A head impact is a short impulse of force acting on a defined site on the head, causing an acceleration or deceleration impulse. The duration of the impulse and the peak acceleration is critical in the outcome of the injury [1].

Several factors determine the excess and the type of injury resulting from a head impact. It has been aimed to yield measures regarding these factors. For instance, in boxing, peak forces resulting from strikes can reach 6860 N. More practicable is to apply the acceleration as a measure: impacts causing mild or severe concussion exceed a rotational acceleration of 5022 1/s [1]. Besides yielding knowledge of the causal measures such as peak impact force or peak rotational acceleration, researchers strived to establish generalized criteria for assessing brain injuries, for each impact event is different and hard to reproduce. The most employed one, the head injury criterion (HIC), identifies the most severe part of an acceleration pulse [5]:

$$HIC = \left( \left[ \frac{1}{t_2 - t_1} \int_{t_1}^{t_2} a(t) dt \right]^{2.5} \cdot (t_2 - t_1) \right)_{max} \quad (4)$$

with  $a(t)$  an acceleration pulse of the impact given in  $g$ -s, and any possible time interval  $t_2 - t_1$  included in the entire duration of the impact. Thus, HIC predicts the excess of injury by assessing two parameters, acceleration and its duration over time [5]. With the help of HIC, threshold values for different injury classifications on a standardized scale can be made, e.g. a probability of skull fracture can be assessed [1].

While HIC has been sufficient to analyze head impacts and accidental injuries in general, a higher need for more elaborated methods for brain injury assessment has emerged recently. More sophisticated criteria have been worked out lately by studies of Fernandes et al. [5], and McAllister et al. [2], who associate stress and strain states in the brain with occurring injuries. With criteria based on strain levels, injuries can be studied in much more detail, focusing on specific types or locations of neuronal injuries inside the brain. Understanding the exact strain distribution inside the brain helps to prevent impacts by developing protections which reduce the acting forces and accelerations and thus resulting strains inside the brain. This can be reached by padding, damping of the acting forces, or by promoting material destruction, of the protection (helmet), improving energy absorption, and by inducing mild deceleration.

In this study, injury criteria have been chosen to be assessed based on the resulting strains inside the brain in our simulations. The first maximum of the logarithmic principal strain is applied, based on [2], which imply a 50% probability of concussion with 0.15 strain in the corpus callosum (one of the critical sites of DAI), or define concussion by reaching 0.35 strain. Besides, a strain threshold of 0.1 is defined for the occurrence of mTBI [5].

Fernandes et al. highlight the Cumulated Strain Damage Method (CSDM) presented by Bandak and Eppinger [80] to evaluate the strain related damage within the brain, providing the possibility to quantify the mechanical damage in axonal components based on a strain state, in FE applications [5]. The method is based on a threshold value of strain. The strain state resulting from a simulation is given at each time increment, and the volume of all elements that have experienced a principal strain above the prescribed threshold is calculated. Based on a critical strain level of 0.15, suggested by [81], it is proposed that a CSDM level of 5 (% of brain volume experiencing above-threshold strain) corresponds to mild DAI, and a CSDM level of 22 corresponds to severe DAI. A concussion is predicted by 50% probability, for a level of 55 [5].

Strain levels are obtained by FE simulations of the head. One of the important factors for building a representative head model is to model the exact geometry of the cortical structures and other parts of the brain. This has been recently established in several studies by employing high-end imaging technologies [32], [54], [82], [83]. The second critical factor in building the head models for simulation is the appropriate application of material properties to different structures of the head, for these play a crucial role in the mechanical response to an impact load. The constitutive equations based on the applied material models define the strain state and time-dependent deformations resulting from an impact. Often, in the case of biological tissues, materials demonstrate hyperelastic nonlinear, viscoelastic behavior [84]. A head impact is a non-linear, dynamic event, hence a linear material representation is insufficient in most cases.

### **3.5. Material models**

Unless we exclusively analyze the kinematics of a rigid body system, material properties play an important role in both the static and dynamic behavior of the system. In this case, the kinetic behavior of a body is highly dependent from its material constitution. Also, the inner mass of the body can be analyzed for fatigue, load, and deformation of the body on the whole. This assessment is carried out by introducing stresses and strains as variables for the inner mass

(continuum) which are connected to the external load on and deformation of the body, in a way, that considering the law of static equilibrium, at any given cross-section of the mass at any given time, the stress state on the section surface has to be equal to the external load. Stress and strain in a mass are dependent from each other, and their relationship is based on the material properties of the mass. From the equilibrium conditions and equations of motion (dynamics), definitions for the stress state can be yielded. From the displacement of the points of the mass (kinematics) relations for the strain state can be derived. Constitutive equations, influenced by material properties, define the relationship between the stress and strain state of the mass [85].

### 3.5.1. Elasticity

Elastic material behavior is characterized by a linear constitutive relation between the stress and strain state of the material, defined by the elasticity tensor  $\underline{\underline{C}}$  having only constant components. This relation is called Hooke's law, with  $\underline{\sigma}$  and  $\underline{\varepsilon}$  as 6x1 vectors containing all stress and strain quantities for a 3D-state [86]:

$$\underline{\sigma} = \underline{\underline{C}} \underline{\varepsilon} \quad (5)$$

This relation implies that in every point of an elastic solid, stress and strain are related linearly, and are independent of time. The constant components of the elasticity matrix can all be defined by using any two parameters of the following [86]:

$E$  – Elastic modulus, the proportion of uniaxial stress to strain

$\nu$  – Poisson's ratio, the proportion of the axial stretch to transverse shrinking

$G$  – Shear modulus, the proportion of shear strain to shear stress  $G = \frac{E}{2(1+\nu)}$

$K$  – Bulk modulus, measure for the compressibility of a material  $K = \frac{E}{3(1-2\nu)}$

A Poisson's ratio of 0.5 implies an incompressible solid [86].

In a rheological model, the elastic relation is represented as a spring, responding linearly with a stretch to an applied load. To be able to apply a linear elastic relation, the case must allow for the assumptions of Cauchy: displacements remain insignificant, and the strain components remain small with respect to unity. Based on these approximations, linear elasticity is a strongly simplified material model. In reality, its applicability is limited in many cases.

Most natural materials deviate from Hooke’s law and additionally demonstrate more complex, time-dependent (viscous), nonlinear (hyperelastic), or irreversible (plastic) behavior.

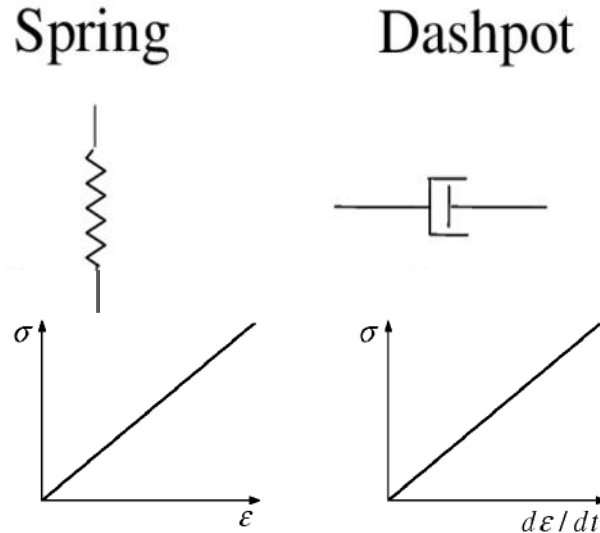


Figure 16: Elastic spring (left) and viscous dashpot (right) rheological models of material behavior, with the corresponding stress-strain relationship

### 3.5.2. Viscoelasticity

Viscoelastic materials exhibit viscous characteristics along with elastic properties. Unlike the elastic relation, the stress in a viscous mass depends not on the extent, but on the rate of deformation, thus it is a time-dependent relation, which is expressed in 1D with the dynamic viscosity  $\eta$  [ $Pa \cdot s$ ] as [86]:

$$\sigma = \eta \dot{\epsilon} \quad (6)$$

Viscoelasticity refers to a broad spectrum of mechanical material behavior, from the domain of purely viscous fluids to purely elastic solids like rubber or metals. In the family of viscoelastic materials, mostly organic compounds, biological materials as tissues or wood, plastics, and concrete are remarkable. Their behavior is strongly influenced by the loading conditions as well as the environment in terms of temperature, chemical environment [87].

Both the stress and strain in a viscoelastic material are time-dependent. One characteristic behavior based on that is creep: the viscous “flow” of a material. It is represented by the change in strain over time under application of constant stress. It can be well described by a continuously increasing elongation of a rod under constant tensile stress for example, compared

to an elastic rod, which would have a constant elastic elongation [87]. This calls for a time-dependent modulus  $E(t)$  satisfying the relation:

$$\varepsilon(t) = \frac{\sigma_0}{E(t)} \quad (7)$$

Along with creep, relaxation behavior is prevalent, which is the change in stress over time under application of constant strain (Formula 8). Taking the rod-example, this would mean an application of a constant elongation (strain), under which the load would decrease over time. Overall time dependency of a material's stress and strain state is described as viscoelastic [87].

$$\sigma(t) = \varepsilon_0 E(t) \quad (8)$$

A viscoelastic material can be rheologically modeled by a combination of elastic spring and viscous dashpot elements, as seen in Figure 17 a.

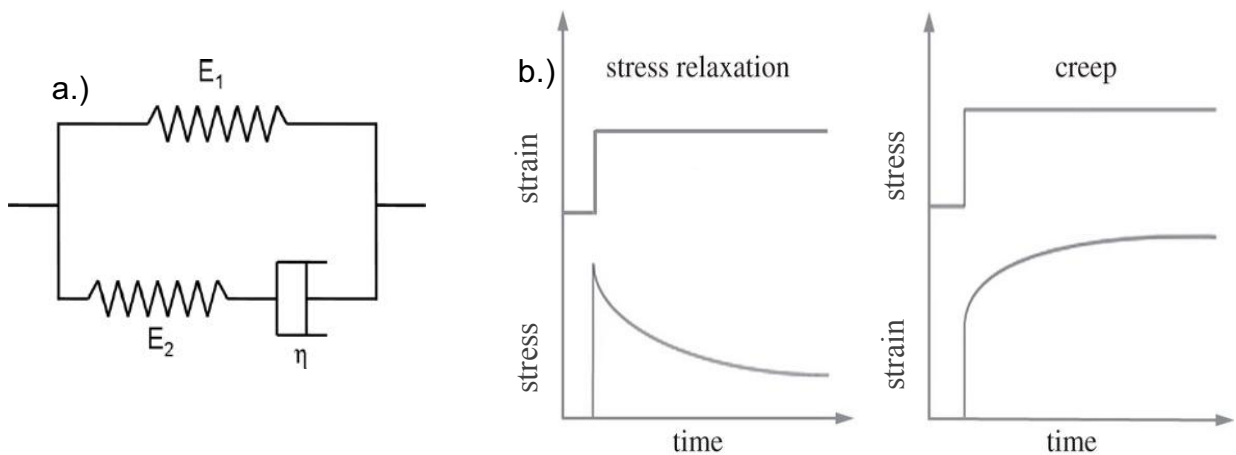


Figure 17: a.) Kelvin-Voigt rheological model of a viscoelastic solid. b.) relaxation and creep behavior

With the help of this model, relaxation and creep behavior can be illustrated, by applying constant step deformation or load, respectively (Figure 17 b). The constitutive relation is implied with a Boltzmann superposition integral, which contains all the deformation history at all times  $\tau$ , and as such, can describe the actual state of the material properties, in every point, in every direction of an anisotropic sample (Formula 9).

$$\underline{\underline{\sigma}}(t) = \int_0^t \underline{\underline{C}}(t - \tau) \frac{d\underline{\underline{\varepsilon}}}{d\tau} d\tau \quad (9)$$

Similar to the elastic case, the constitutive matrix can be filled by using two viscoelastic functions, whereas this anisotropic tensor relation is rarely used. In practice, most materials can be considered being isotropic, so that the expression simplifies, and the constants, as well as interrelations for isotropic elastic materials  $E, \nu, G, K$ , can be utilized and varied over time. Thus, the viscoelastic relaxation functions  $E(t), \nu(t), G(t), K(t)$  are yielded, which are preferred to be employed as engineering expressions, than in tensors. This implies e.g. for the uniaxial tension [86]:

$$\sigma(t) = \int_0^t E(t - \tau) \frac{d\varepsilon}{d\tau} d\tau \quad (10)$$

and for shear stress [86]:

$$\sigma(t) = \int_0^t G(t - \tau) \frac{d\varepsilon}{d\tau} d\tau \quad (11)$$

The variation of the Poisson's ratio over time is insignificant in certain cases and can be approximated as constant ( $\nu$ ). In this case, a biological tissue, especially with high water content, is nearly incompressible ( $\nu \approx 0.5$ ), and this incompressibility is not subjected to changes over time, for it is assumed that the condition of the tissue sample is steady during the experiments. Thus, the effort of using two independent viscoelastic functions can be avoided, and simple relations follow [86]:

$$G(t) = \frac{E(t)}{2(1 + \nu)} \quad (12)$$

$$K(t) = \frac{E(t)}{3(1 - 2\nu)} \quad (13)$$

For the evaluation of the convolution integrals in the constitutive relations, the viscoelastic functions have to be defined. Relaxation and creep experiments, as well as relations following from the Kelvin rheological model imply, that  $E(t)$  demonstrates exponential behavior [85]:

$$E(t) = E_0 e^{-\frac{t}{\tau_r}} \quad (14)$$

with the relaxation time  $\tau_r$ , which characterizes the time needed for a viscous phase to recover from shear stresses, and is proportional to the viscosity of a material [85]. In reality, materials demonstrate more complex behavior which cannot be approximated by a single exponential function undergoing most of its decay within a single time decade. Real materials relax and creep over many decades on the timescale.



Therefore, it is better to construct a series of exponential functions, yielded from more sophisticated rheological models (Kelvin-elements in series) and the resulting differential equations. Thus, a generalized expression can be obtained, formulated as a sum of exponential functions with corresponding relaxation times:

$$E(t) = E_{\infty} + \sum_1^n E_i e^{-\frac{t}{\tau_i}} \quad (15)$$

with the equilibrium modulus  $E_{\infty}$ , which describes the material behavior in the static phase where the viscous components do not have any more influence. The sum in (15) is called a Prony-series, which can be applied to approximate the relaxation modulus of more complex materials which consist of multiple phases, such as composites or biological materials [86].

It is proven that the relation  $E_0 = E_{\infty} + \sum_1^n E_i$  holds at the origin, by setting  $t = 0$ , yielding the instantaneous modulus  $E_0$ , which is expressing the initial purely elastic response of the material. Thus, a more descriptive representation of the relaxation modulus is:

$$E(t) = E_0 - \sum_1^n E_i (1 - e^{-\frac{t}{\tau_i}}) \quad (16)$$

applied for shear:

$$G(t) = G_0 - \sum_1^n G_i (1 - e^{-\frac{t}{\tau_i}}) \quad (17)$$

It is convenient to eliminate the absolute levels of the modulus parameters  $G_i$ , to yield a dimensionless expression, by normalizing by the instantaneous response  $G_0$ :

$$g(t) = 1 - \sum_1^n g_i (1 - e^{-\frac{t}{\tau_i}}) \quad (18)$$

This is the normalized Prony-function, simply to characterize by providing only the dimensionless parameters  $g_i$  and corresponding time constants  $\tau_i$ , called together as Prony-pairs [88].

In real materials the viscoelastic behavior is nonlinear, for the characteristic material properties (e.g.  $E(t, \varepsilon(t))$ ) are dependent not only from the time, but also from the actual stress or strain state. However, in most cases when testing for viscoelastic properties, the assumption for Quasi Linear Viscoelasticity (QLV) separating strain- and time-dependence must be made to be able to yield parameters and describe the behavior.

To be able to employ QLV, the only assumption to be made is that the shape of the relaxation function is the same at all strain levels, thus eliminating the influence of strain on the absolute quantities in viscoelastic functions [86]. This enables the use of dimensionless Prony-series, which describe solely the characteristics of the exponential decay of viscoelastic functions. This approach has been proven feasible even in the case of complex biological tissues [25], [89].

### **3.5.3. Hyperelasticity**

In the case of special soft solids, the material behavior cannot be effectively described with the assumption of small displacements, and small strains, as assumed in a linear elastic Hookean case. For instance, in the case of a real uniaxial tension of a soft elastic material, the cross-section, and the resulting apparent stress state at any given time is not constant [27]. These materials exhibit hyperelasticity, that is, they can undergo large deformations and displacements under load, with little volumetric change (near incompressible) [90].

To describe hyperelasticity, many models have been developed recently: physically motivated models are those of Arruda-Boyce and Van der Waals. More widespread are phenomenological models using a polynomial (order  $N$ ), such as Mooney-Rivlin (1st order), Neo-Hookean (1st order) Yeoh (3rd order) (Abaqus/Explicit Advanced techniques, 2005). In general, an isotropic hyperelastic incompressible material is characterized by a strain-energy density function  $W$ . Mathematical models have been developed which derive material constants from the minimum strain energy density, such as Fung, Gant, Ogden. While the Fung and the more elaborate Gent models are appropriate for soft tissues with high collagen fiber content dominating their stiffness, such as skin and arterial walls, they could not be applied for brain tissue [22].

## **3.6. Material properties of GM and WM**

To be able to model impacts and assess stresses and strains in a simulation, the materials needed to be modeled as close to reality as possible. Often in the case of biological tissues, materials have to be represented by nonlinear material models. Most cases in biomechanics deal with the skeletal, movement-related problems, with bone, muscle and tendon tissues, comprised of elastin and muscle fibers being the building bricks of these materials, and enabling an assessment by strong simplifications to linear elastic cases. However, in this case, the nervous tissue is not so simply described, being a very soft, and structurally heterogeneous material.

A precise representation is needed, as close to reality as possible, for one major goal of this thesis is to identify differences in the material properties of distinguishable layers of the grey matter neocortex, to be able to create more precise simulations.

### 3.6.1. Elastic properties

Although, as described above, real brain tissues differ from a purely elastic behavior, in this study experiments for the elastic properties will also be conducted, to obtain knowledge about the overall stiffness of the different layers of the tissue, focusing on its variation. Additionally, in a lot of applications, e.g. constructing a functionally graded material model, or in the case of an assessment of overall stiffness at instantaneous loads, it is practicable to apply only the elastic model, whereas the other material models are more complicated and non-constant, making them ineligible for several applications.

The near incompressibility of the tissue is represented by a high bulk modulus (Formula 19), found experimentally first by Stalnaker and McElhaney [92], validated and implemented by Kleiven et al. [4], along with several other researches since then [79], [82], [90], [93].

$$K = 2.19 \text{ GPa} \quad (19)$$

Brain elastic moduli have been observed in different species to lie between 1200 – 2000 Pa depending on location and measurement method. The most recent values for the human brain have been provided by [29], who found the average elastic moduli of 1.895 kPa ± 0.592 kPa (WM) and 1.389 kPa ± 0.289 kPa (GM). Using the relation (13), this implies a Poisson's ratio to lie approximately in the range of  $\nu = 0.49999985 - 0.49999999$ , whereas a novel study has shown that a slight variation of the brain's Poisson's ratio does not have a significant influence on the material response [94]. In practice, the approximation of  $\nu = 0.5$  is often employed, e.g. in the case of the relationship (12), where a slight variation of  $\nu$  does not influence the order of magnitude of the other parameters.

### 3.6.2. Hyperelastic properties

The hyperelastic behavior of brain tissue, pronounced in Chapter 3.5.3, cannot be described by the fiber-related Fung or Gant models, for tissues having large aggregates of cells and high lipid content, are defined by their cellular structure and not by the fiber content [22]. This also

supports our primary hypothesis in this study, that the cellular pattern of the grey matter layers implies differences in the material properties of the layers. Mihai et al. describe the phenomena which subject the brain tissue to be modeled as hyperelastic, in [22]. Most of the mechanical test data available for brain tissue in the literature are fitted with the hyperelastic model developed by Ogden [21] for rubber-like materials. As found by Franceschini [26], after conducting a broad experimental study on brain tissue, the loading and unloading uniaxial curves follow the Ogden nonlinear elastic theory of rubber. Rashid et al. [27] also implies that up to 0.3 strain, an Ogden model is perfect for modeling the hyperelastic behavior of brain tissue. Since then, this theory has been successfully validated and employed, in [23], [25], [84]. The theory of Ogden expresses the strain energy density  $W$  as

$$W = \sum_n \frac{\mu_i}{\alpha_i} (\lambda_1^{\alpha_i} + \lambda_2^{\alpha_i} + \lambda_3^{\alpha_i} - 3) + \frac{1}{2} K (J - 1)^2 \quad (19)$$

with the Ogden parameters  $\alpha_i$  and  $\mu_i$ , fitted to the principal strain invariants  $\lambda_1, \lambda_2, \lambda_3$ . Kleiven et al. [4] exhibit that a second order approximation is sufficient for the brain, and derives following parameters from the experiments of Franceschini [26]:

$$\begin{aligned} \mu_1 &= 53.8 \\ \mu_2 &= -120.4 \\ \alpha_1 &= 10.1 \\ \alpha_2 &= -12.9 \end{aligned}$$

### 3.6.3. Viscoelastic properties

Galford [18] already studied the viscoelasticity of brain tissue in 1970. In the following studies, it has been explicitly suggested to model the viscoelasticity of the brain with Prony-series [26], [27]. Recently, several studies have successfully employed models using the Prony-series to describe its viscoelastic behavior [19], [20], [32]. In [25] and [32] it was found to be sufficient to apply a 2-term Prony-series to describe brain shear modulus for computer simulations, whereas Kleiven et al. applies a 6-term series in [4]. Most of the above studies suggest the combination of hyperelastic and viscoelastic models to completely describe brain behavior, for the tissue exhibits both phenomena.

## 3.7. Experimental measurement of material properties

### 3.7.1. Measurements for elasticity

Elastic properties are conventionally measured by tensile tests. In 1D, an elongated body of the material (bar, rod) is embedded at both ends and a tensile load is applied. The load and elongation are measured and by the geometrical characteristics, stress and strain values are calculated, from which the elastic modulus can be assessed. (Hooke's law, uniaxial tension). In a biaxial test, a tether or thin shell is subjected to a 2D stress/strain state, again, from the registered stresses and strains, the material constants can be computed.

### 3.7.2. Measurements for viscoelasticity

Viscoelastic properties require more complex measurements due to time-dependency, such as creep or relaxation tests (Figure 17), where either the sample is subjected to an instantaneous constant load  $\sigma_0$  and the elongation behavior  $\varepsilon(t)$  is registered over time (creep), or the stress decay  $\sigma(t)$  is registered over time subjected to a constant elongation/strain  $\varepsilon_0$  (relaxation) [85]. From a relaxation decay, the time-dependent relaxation modulus can be extracted using (8):

$$E(t) = \frac{\sigma(t)}{\varepsilon_0} \quad (20)$$

This method has been employed by [28], [30], [48], and [95]. Time dependency also implies frequency-dependency in the case of a cyclic loading of the material. To assess this behavior, cyclic, oscillating creep/relaxation experiments are conducted to assess the storage and loss modulus which represent the elastic and viscous part of the material properties, respectively [86]. Additionally, it is possible to measure viscoelasticity by compression and indentation tests. For instance, indentation punch tests can be employed to compute formula (20), by registering force over time after applying a constant indentation depth (displacement).

### 3.7.3. Indentation measurements with AFM

The above-described methods are complicated to apply when it comes to special materials, such as biological tissues, being a multi-scale composite structure, consisting of cells, fibers, proteins, water, often being too microscopic and vulnerable to be able to conduct conventional tensile experiments. Hence, a successful alternative is provided by micro- or nanoindentation.

Nanoindentation provides a high load resolution, fine depth-sensing capabilities, and can be used to characterize the local mechanical behavior in heterogeneous microstructures [95]. Indentation tests have been originally established for measuring hardness and plasticity of different, mostly hard materials, first by Brinell. In the case of traditional indentation, a probe of known geometry is driven to approach and puncture the surface of the material applying a given force or displacement, then retracted. The residual trace of the indenter head in the material is assessed visually in its geometrical shape, which is then associated with a hardness number. Today's instrumented indentation (with digital control equipment and precision measurement instruments) enables monitoring and controlling load and displacement on the nanoscale [95].

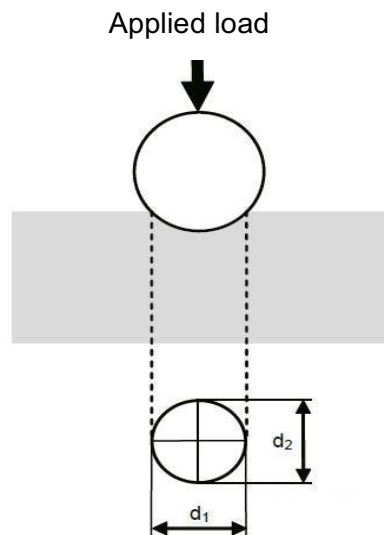


*Figure 18: Brinell's indentation test scheme*

The utilization of the Atomic Force Microscope as an indenter has just emerged recently as a method for creating high-resolution force-displacement data by exerting an approach and retract motion of the indenter head and assessing deformations, surface interactions, and topography. Appropriate mathematical models (e.g. by Hertz) and embedded fitting functions allow for deriving material properties and other mechanical data [96]. The function of the Atomic Force Microscope is based on a soft, thin cantilever with a known stiffness, with a tip on its end with a known geometry (mostly pyramidal shape). This cantilever is attached to a head, the displacement of which can be precisely controlled vertically, with movements induced with the help of a piezo crystal installation (z-direction movement). The head can also exert controlled movements in x and y directions. The position of the sample plate bedding can be manually adjusted as in a classic microscopic setting.

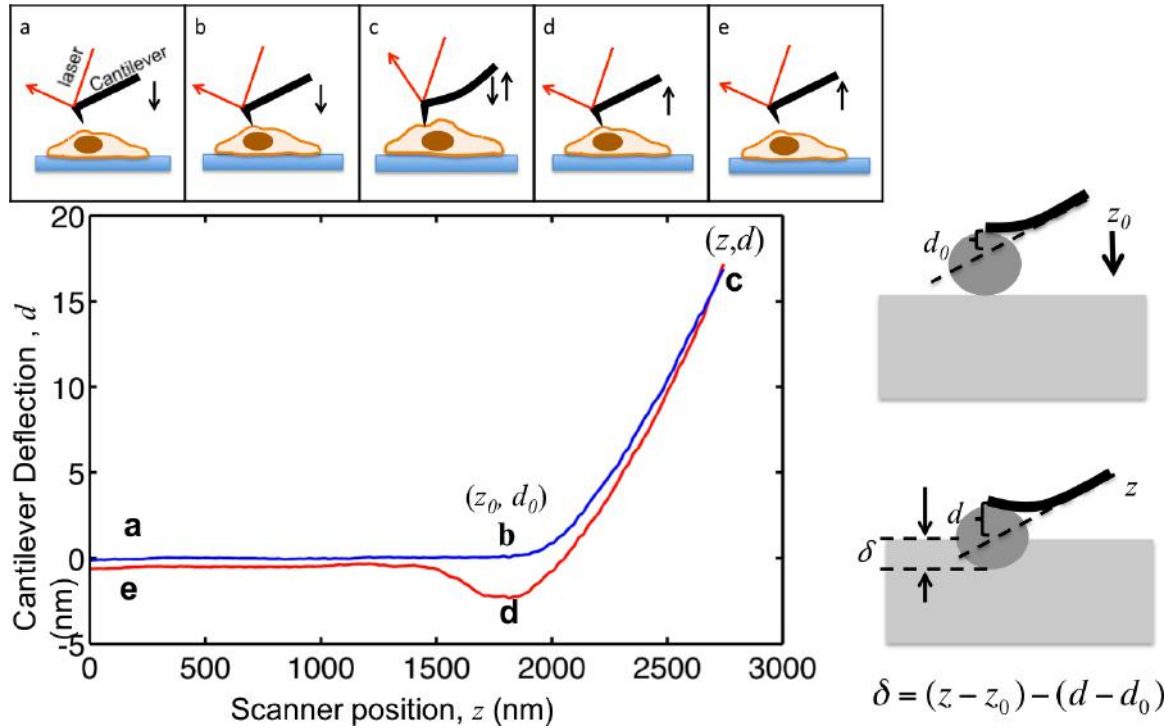


Figure 19: Scheme of indentation theory, with piezo position  $z$ , depth  $\delta$ , and deflection  $d$  [14].

The light beam of a super-luminescent diode source is directed onto the cantilever end which has a reflective coating which reflects the light through a lens system onto a position sensitive detector (Figure 19). Thus, the slightest movements of the cantilever tip can be captured by the displacement of the reflected beam on the detector. After calibration, various quantities such as the load on the cantilever or the depth in the case of indentation can be concluded from this input, depending on the purpose of use [97]. With AFM nanoindentation,  $z$ -depth in  $nm$  and loads in  $nN$  are possible, making it applicable to measure thin films and tissue samples.

An AFM nanoindenter can be utilized to create a force-displacement plot at a fixed  $x$ - $y$  position, by a controlled  $z$ -displacement of the cantilever head causing the tip to approach the surface and indent the sample to a defined depth. During this procedure, the contact force is measured, which emerges by the resistance of the sample material to indentation. From the force-displacement data, material properties, such as the elastic modulus  $E$  can be concluded. For a sharp pyramidal tip causes errors in the measurements and often damages soft and thin samples, a spherical tip is commonly used for tissues, having a radius on the  $\mu m$  scale. A spherical tip is advantageous, due to the lowest caused stress and strain in the material among all tip geometries, which allows for small strain assumption and the application of classical Hertzian theory when computing elastic stiffness. A prevailing procedure is to construct a spherical indenter tip by attaching a colloidal microsphere on a tipless cantilever [96].

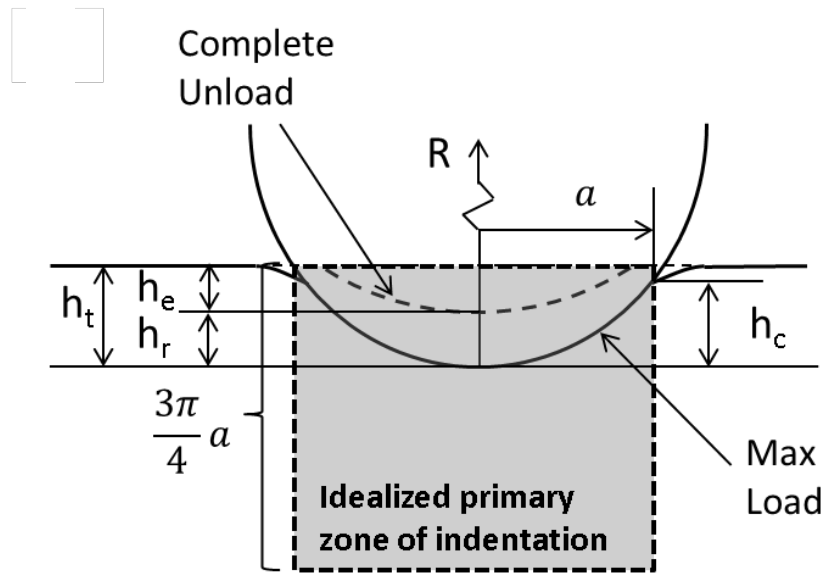


Figure 20: Spherical indentation scheme, with indentation radius  $a$  and contact depth  $h_c$  [95].

In Figure 20, the theory of spherical indentation is demonstrated.  $R$  is the indenter radius,  $h_t$  is the total depth of indentation measured from the original surface,  $h_e$  is the elastic height, which corresponds to an elastic reversible deformation,  $h_r$  is the residual height corresponding to a plastic residual deformation. The contact radius  $a$  is an important measure to represent the real contact surface between the sample and the indenter probe.

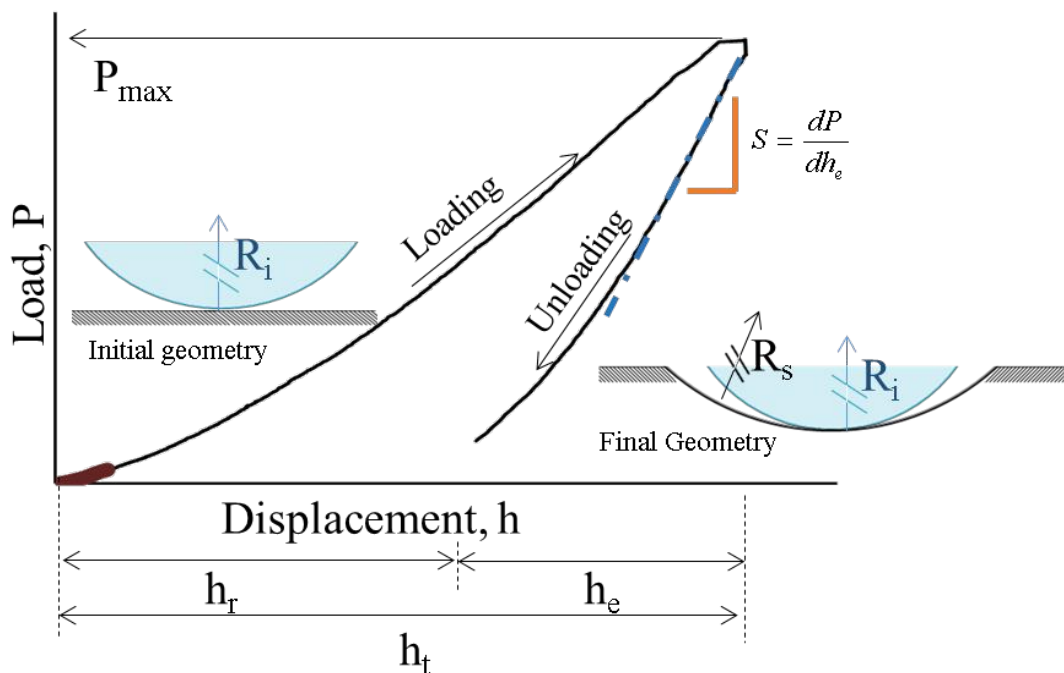


Figure 21: Schematic force-displacement plot and corresponding indenter positions, with the slope of the unloading curve  $S$ , equaling the contact stiffness  $k$  [95]



The resulting force-displacement plot from a spherical indentation is pictured in Figure 21. After being neutral in the approach phase, the cantilever bends and takes on load as it pushes onto the surface of the sample, then unloads when turning into the retract phase. Hertz [98] provided the following relationship between force and displacement under the assumption of small strains/depth:

$$F(t) = \frac{4}{3} \frac{E}{(1 - \nu^2)} R^{\frac{1}{2}} h^{\frac{3}{2}}(t) \quad (21)$$

Once a force-displacement plot is constructed, the primary quantity to be measured on the plot is the contact stiffness  $S$ . This can be extracted as the linear slope fitted to the beginning of the unloading curve (Figure 21). There is a consensus since the study of Pharr, that this part of the curve has to be assessed for elastic measurements, as it represents the elastic behavior of the material at the most accuracy [7]. Since then, this method has been successfully applied in several studies [6], [29], [95]. Based on equation (21), the slope can be derived [8]:

$$\frac{dF}{dh} = \beta \frac{2E_0}{(1 - \nu^2)} \sqrt{R h_{max}} \quad (22)$$

$$S = \beta \frac{2E_0}{(1 - \nu^2)} \sqrt{\frac{A}{\pi}} \quad (23)$$

Where Cheng & Cheng [8] introduces the experimental correction factor  $\beta = 1.02$ . With help of the contact stiffness  $S$ , the instantaneous elastic modulus can be expressed [6]:

$$E_0 = (1 - \nu^2) \frac{S}{2\beta} \sqrt{\frac{\pi}{A}} \quad (24)$$

with the contact surface  $A = \pi a^2$ . This describes the purely elastic behavior of the sample. The most widely used formula for computing  $a$  with the help of  $h_c$  was provided by Oliver & Pharr [6], suggesting an influence of the maximum indentation force  $F = P_{max}$  and  $S$ :

$$a = \sqrt{2R h_c + h_c^2} \quad (25)$$

where

$$h_c = h_{max} - 0.75 \frac{F}{S} \quad (26)$$

There is a disagreement with this method in a recent study by Cheng & Cheng [8] who suggest that the contact stiffness and maximum force are not essential in the computation of  $a$ :

$$a = \sqrt{2Rh_c} \quad (27)$$

$$h_c = \frac{h_{max}}{2} \quad (28)$$

In our measurements, both approaches will be computed and compared.

A nanoindenter also allows for registering forces, displacements on the time domain, as well as on the frequency domain. With the help of these functions, time-dependent force or displacement plots can be created by applying controlled displacement or controlled load, respectively, resembling a relaxation or creep test (Figure 22). This allows for the assessment of the viscoelastic properties of the sample material. Radok [99] implies that in the case of the viscoelastic problem, the same relationship between force and displacement can be applied, as in the elastic case (Formula 21). For instance, in the case of a relaxation experiment, the depth being constant, the modulus is time-dependent, as well as the registered force over time. This theory is commonly applied in viscoelastic indentation protocols e.g. [11], [30], [95].

This yields in the case of the shear modulus [100]:

$$F(t) = \frac{8}{3} \frac{G(t)}{(1-\nu)} R^{\frac{1}{2}} h_0^{\frac{3}{2}} \quad (29)$$

$$G(t) = \frac{3(1-\nu)}{8 R^{\frac{1}{2}} h_0^{\frac{3}{2}}} F(t) \quad (30)$$

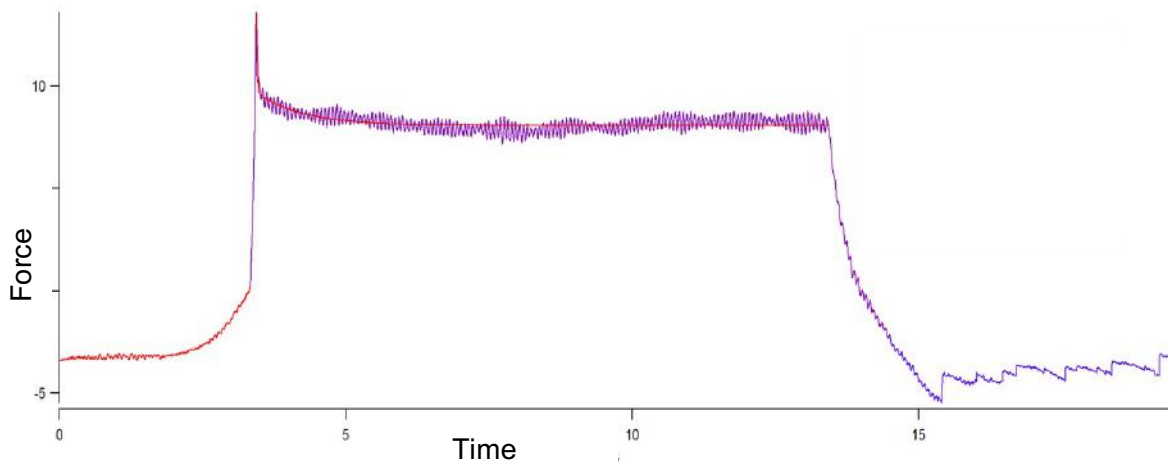


Figure 22: Force-time plot from a relaxation experiment conducted in current study by AFM indentation (compare with Figure 17 b.)

## 4. Employed experimental methods

### 4.1. Preparation of the sample

#### 4.1.1. Cadaver

To be able to obtain findings from our study at the closest to reality, we aimed to examine a sample of the human brain. A human brain cadaver has been obtained from the laboratory facility of CUNY school of medicine, Department of Pathobiology. The cadaveric brain had been extracted from a 67-years-old male and preserved in formaldehyde solution. A cubic cut-out segment has been extracted from the brain cortex of the right hemisphere, containing the grey matter neocortex and a significant amount of white matter. The location of the segment is at the frontal cortex, in the region of the superior/medium frontal cortex across the stretching ridge of the superior frontal gyrus, dorsomedial from the accessory superior frontal sulcus (acsfs), as shown in Figure 23. The sample lies within the region defined as *area 9* by Brodmann [38], and called as *area FD* by Economo & Koskinas [67] (Figures 25&26).

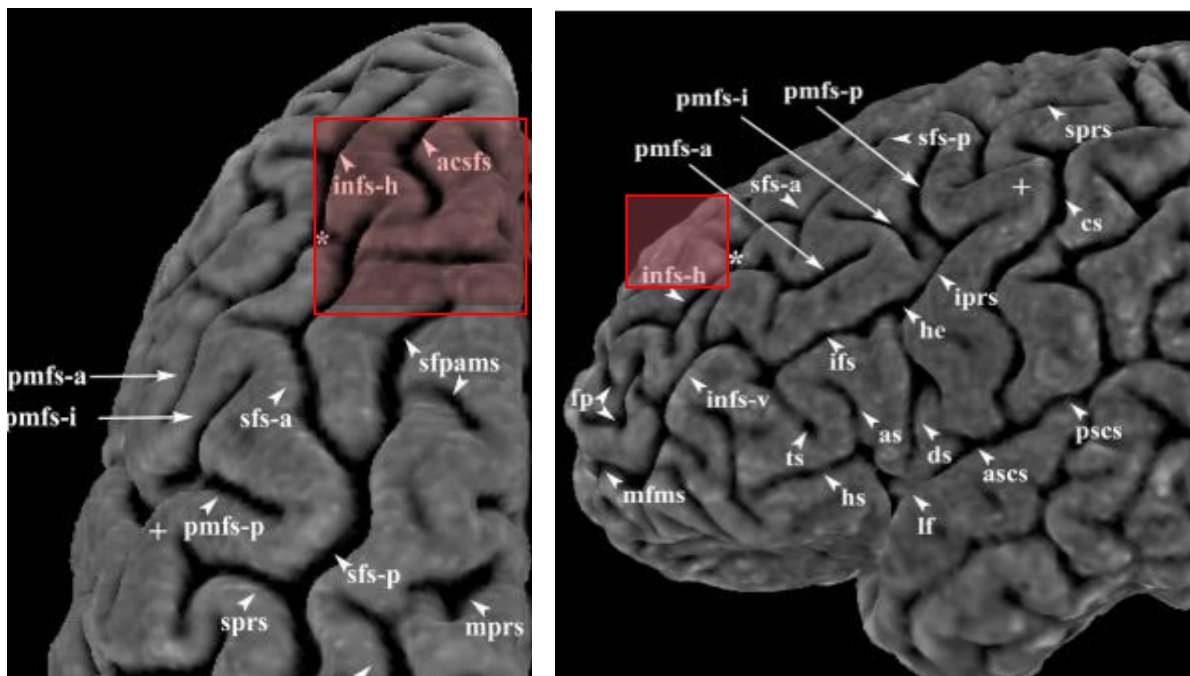


Figure 23: Extraction site of our segment illustrated on an image of the left hemisphere, by Petrides&Pandiy. Left, superior view, right, lateral view of frontal cortex [117].



Figure 24: Extraction site illustrated on an image of the anterior view of left hemisphere of the brain [117], and on a picture of the actual cadaver used in current study (superior view, right hemisphere).

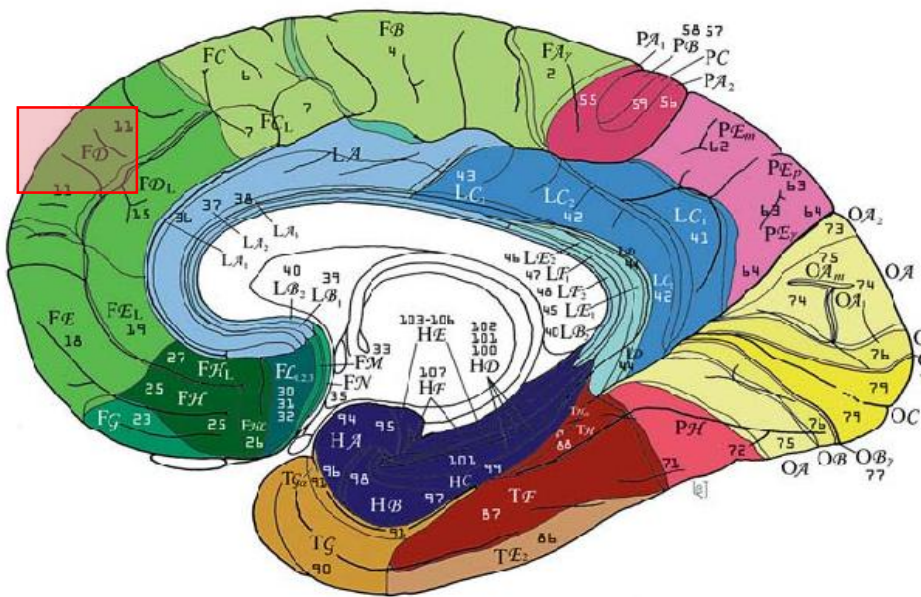


Figure 25: Extraction site illustrated on the brain map by Economo & Koskinas [67].

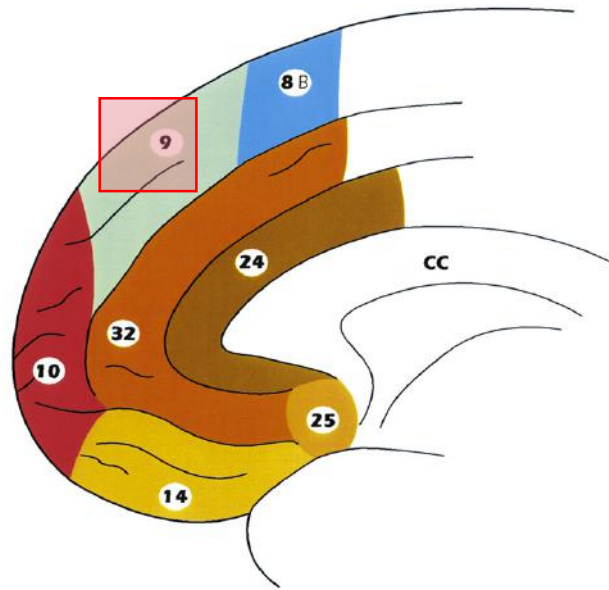


Figure 26: Extraction site illustrated on a map made by Petrides & Pandiya after Brodmann [117].

The cubic segment ranges 30 mm in medial-lateral width, it has a depth of 25 mm towards the white matter, as well as an approximate dorsoventral range in height of 22 mm. The cut-out was placed in water, sealed and stored in a cool environment.

#### 4.1.2. Preparation and segmentation

From the extracted piece of the frontal cortex, several thin slices with the thickness on the micrometer scale were planned to be obtained. One slice was needed to be stained and analyzed under a microscope for visual assessment of the tissue structure. One other slice would be needed for the AFM nanoindenter measurements. Besides these, additional slices were prepared to serve as reserve backup samples for each purpose.

#### 4.1.3. Microtome slicing

A microtome device was utilized to obtain samples for microscopic analysis. A microtome has a very precise cutting mechanism with controlled alignment of a rolling blade, allowing for adjustment of cut thickness on the microscale. To be able to cut soft materials, like biological tissues, such as our segment of brain tissue, the material had to be immersed and embedded in paraffin wax.

First, a cut of a complete gyrus had been extracted from the cubic cut-out segment with a razor blade, having a width of 21 mm, a depth of 18 mm, and a thickness of only 5 mm, to fit in the processing unit for waxing (Figure 27, left). The automated vacuum tissue processor Leica ASP 300S (Leica Microsystems Nussloch GmbH, Nussloch, Germany) was utilized. The tissue sample was washed with 100% denaturated alcohol, cleared, and bathed with paraffin wax Histoplast LP (Richard-Allan Scientific, Kalamazoo, MI, USA) at 60 °C. The specimen which was thus immersed with paraffin wax was put in a container of the same paraffin wax at 60 °C, and left to solidify (Figure 27).

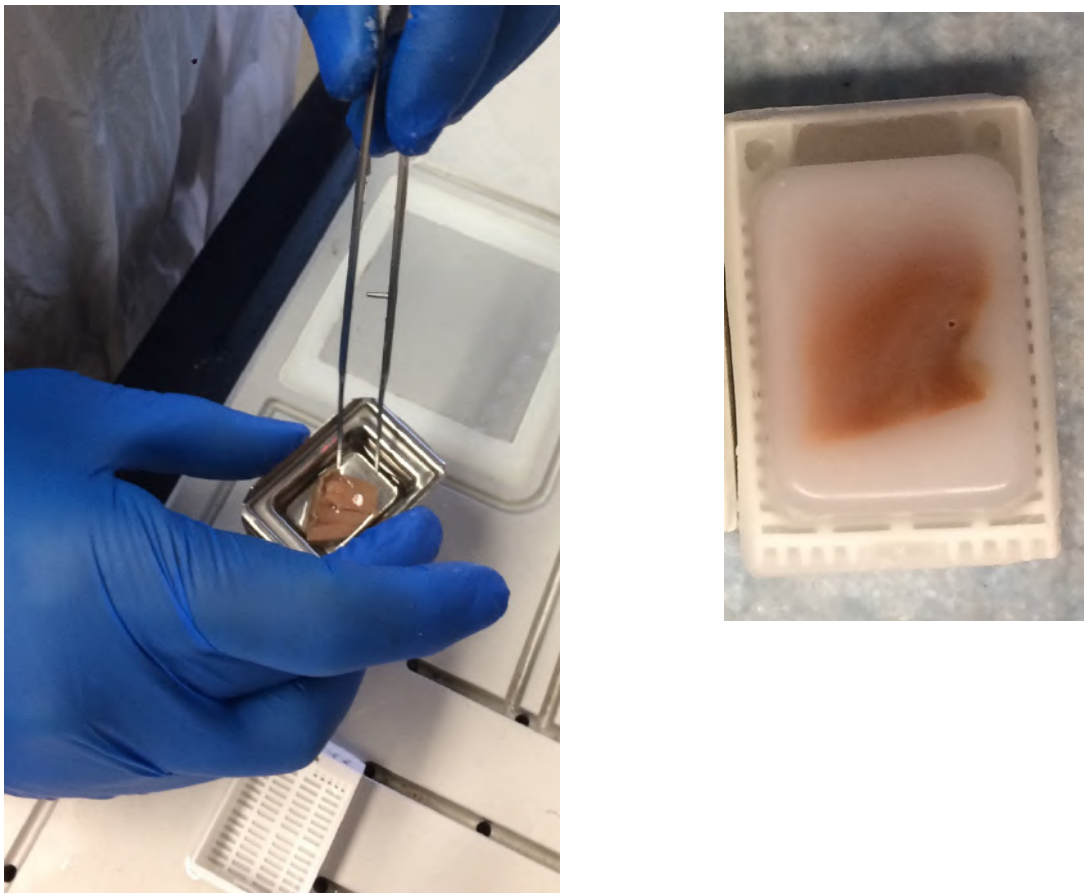


*Figure 27: Immersing in paraffin wax(left), and immersed solidified sample, ready to be sliced (right)*

Thus, the specimen had been prepared in a solid wax cube for slicing in the microtome (Leica RM 2265, Leica Biosystems Nussloch GmbH, Nussloch, Germany). Three slices of 1.5  $\mu\text{m}$  thickness were produced in the microtome for microscopic analysis, and one 12  $\mu\text{m}$  slice for the indentation. The slice for the indentation had to be the thickest possible, to be able to reach a sufficient maximum indentation depth of 1  $\mu\text{m}$  and still being able to approximate the sample having an infinite thickness, to be able to apply Hertzian theory [98]. Still, transparency had to be preserved for in the AFM, thus, the thickness had to remain under certain boundaries.

Apart from that, the microtome can only be utilized without errors under a certain thickness, if not, errors in the surface integrity and homogeneity would occur. Thus, a sample thickness of  $12\ \mu\text{m}$  could be yielded by preserving surface continuity, transparency, and sufficient depth in thickness. The slices were cut after each other so that the neighboring slices resemble basically the same specimen having the same tissue structure and material properties. The aim of this procedure is to be able to make precise visual microscopic observations of the exact same sample as the one that the AFM measurements would be conducted on.

The obtained slices were laid on a conventional glass plate and washed out from paraffin wax. The three Microscopic slices were stained with hematoxylin-eosin (H&E) stain and hermetically covered with a transparent thin covering plate, thus prepared for microscopic analysis. One of them would be the microscopic sample, two of them would serve as backup samples. The two were not needed during our study.



*Figure 28: Specimen prepared for microscopy, with H&E staining*

The thicker slice determined for indentation analysis was also washed out from paraffin and put into filtered water for storage. It was aimed to cause the least artifacts in the phase of sample preparation so that the slice determined for indentation had not been stained, neither had it been left embedded in paraffin. Thus it was intended to preserve the realistic material properties at most. The tissue slice was then stored in its neutral state, without any foreign or chemical agents at  $15\ ^\circ\text{C}$  temperature.

## 4.2. Microscopy

The microscopic sample had been stained conventionally using H&E staining. This type of Papanicolaou staining combination is particularly suitable for differentiating and defining cell nuclei and distinguish them from the cytoplasm and extracellular matrix and visualize their structural details [101]. Harris hematoxylin stained the nucleus of cells in chromatin blue, highlighted the nuclear details of a cell, and left them transparent to be able to distinguish the cell wall while leaving the cytoplasm totally discolored. Eosin colored the nucleoli red, and stained cytoplasmic structures in varying shades of red to pink. With the combination of the two, the neural cell nuclei, colored dark purple, could be distinguished from the network of axons and dendrites, having light pink colors. Thus, the cells could be counted, and their density could be analyzed, as well as their shapes could be assessed to distinguish between pyramidal and granular cells, which would play a significant role in defining the cellular and histological structure and differentiate between layers.

The sample was examined under a ZEISS Axiocam HRc (Carl Zeiss micorimaging GmbH, Jena, Germany) microscope, and the tissue structure was visually analyzed, after post-processing with the software AxioVision (Release 4.8.2 SP2, Carl Zeiss microimaging GmbH, Jena, Germany). It was aimed to identify the six layers that would be present in this sample of Brodmann's *area 9*, as well as to assess cell types and cell density in each layer. 10x and 20x zooms were employed.

## 4.3. AFM measurements

Based on the theory discussed in Chapter 3.7.3. an AFM nanoindenter was utilized, to be able to conduct experiments on a dimension scale which, on the one hand, allows for differentiating between layers of the neocortex, and, on the other hand, for taking numerous distinct measurements across the layers of the grey matter having a width on a scale of  $100\ \mu m$ , and a slice thickness of  $12\ \mu m$ .

Forces in the order of nanonewtons were used, along with indentation depths on the  $100\ nm$  scale and indenter size of the  $\mu m$  scale. This allowed for a precise assessment of a small vulnerable material, which was expected to demonstrate a remarkable deformation under vast loads.



### 4.3.1. Instrument properties

We utilized the Atomic Force Microscope MFP-3D™ (Asylum Research, Inc, Santa Barbara, CA, USA) as an instrumented nanoindenter.

It is a complex system, which includes two monitors, a specially configured Dell computer, the SPM controller unit type ARC2, the MFP head, the MFP scanner and the standalone base which houses the optical system. It is most suitable for opaque specimens such as the current one [97]. The system was installed on a concrete slab ground floor, isolated from any noise and vibrations, and the ambient temperature was kept at 18 °C.



*Figure 29: External view of the installed AFM instrument utilized in the study (left), and the head being adjusted for the height (right)*

Both a top and a bottom view of the sample and cantilever could be realized in a dual-view base, with embedded 10x objectives as well as CCD-cameras both in the head and in the base for top and bottom view, and employing the fiber illumination system Fiber-Lite Mi-150R (Dolan-Jenner Industries, USA). The base additionally provided the stage for the sample, which could be moved manually in x and y directions with micrometer precision, so that the exact location of the sample under the cantilever tip could be set.

The head part included the cantilever holder, a top view camera and illumination source, and adjustment knobs for the position of the laser beam on the cantilever. The head unit was assembled with the base with the help of three indentations on the base, into which three pillars from the head reach and precisely took a fixed position. Thus the head had a stable x-y position and could be dismounted from the base anytime for slice manipulation. The height of the head could be adjusted vertically by adjusting the height of each pillar on the 0.1-micrometer scale (Figure 29 right, and Figure 31).

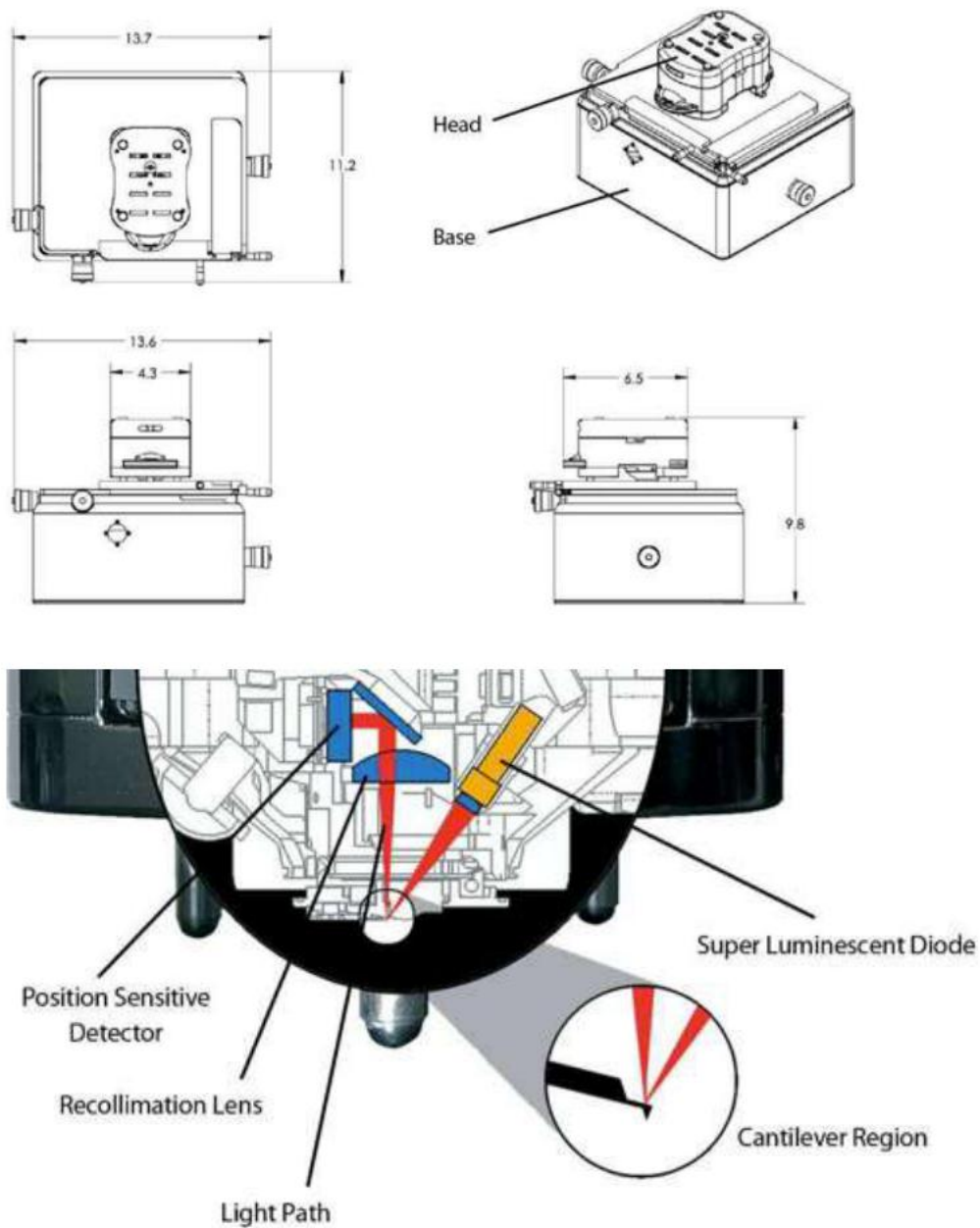
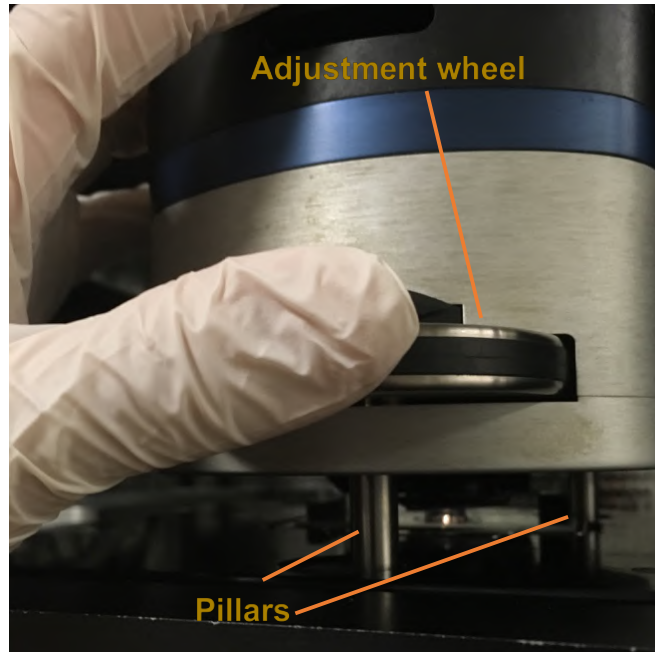


Figure 30: Schematic view of the parts (top) and function (bottom) of the AFM system [97].



*Figure 31: Adjusting the height of the head by turning the precision adjustment wheel*

The measurements took place with the cantilever and the specimen being constantly in an aqueous environment, to maintain the tissue consistency and hydration level. The reason for that is to avoid artifacts which would occur by only a short time of drying of the sample. Additionally, other erroneous effects such as surface adhesion and surface tension, common in the case of biological samples, could be diminished by immersion of the setup in water [97], as it is also applied e.g. by Budday et al. in [29]. The manual and protocol of the AFM instrument prescribe that the sample, as well as the cantilever, is totally immersed in the liquid in the case of testing in liquid. This is important as sometimes the liquid will not fill the whole space between the cantilever chip and the holder, and the beam of light will break on air/liquid boundaries, and not reach the photodetector [97].

#### **4.3.2. Choice of the cantilever**

A cantilever with a spherical tip had been installed into the cantilever holder. The cantilever parameters had been chosen specifically to our measurements. In order to reach sufficient accuracy in measuring the (visco-)elastic properties of a material, the choice of the cantilever had to be made carefully. The spring constant  $k$  (stiffness) of the probe cantilever must be identical to the contact stiffness of the sample  $S$  [97]. If the spring constant of the cantilever is more than 10 times lower or higher than that of the sample, the sensitivity of measurements is about 3 times lower, making the determination of the elastic modulus less accurate [13].

The sample contact stiffness was not exactly known beforehand; therefore, a probe stiffness was chosen which has the same order of magnitude as the expected contact stiffness. The limited availability of tipless cantilevers to be obtained for our purpose narrowed down the spectrum of choice. Also, it had been taken into consideration that a cantilever stiffness slightly higher than the sample stiffness is still more desirable than a lower cantilever stiffness being incapable of penetrating and indenting the sample.

Finally, silicon cantilevers having a nominal stiffness of  $0.29 \text{ N/m}$  (range  $0.13 - 0.6 \text{ N/m}$ ), type SICONG-TL-SIO2-D5 (Applied NanoStructures, Inc, Mountain View, CA, USA) had been obtained for the experiments. Technical data of the cantilever type is provided in Appendix B. The surface of the cantilever had a reflective gold coating.  $\text{SiO}_2$  silica glass spheres had been attached to the end of the cantilevers, having a nominal diameter of  $30 - 40 \mu\text{m}$ . The real apparent diameter, measured under the AFM instrument was found to be  $38 \mu\text{m}$  (Figure 33). One obtained cantilever probe was installed into the cantilever holder as prescribed by the instruction manual of the instrument, reaching  $11^\circ$  angle of inclination with respect to the x-y plane, to optimally capture the laser beam [97].

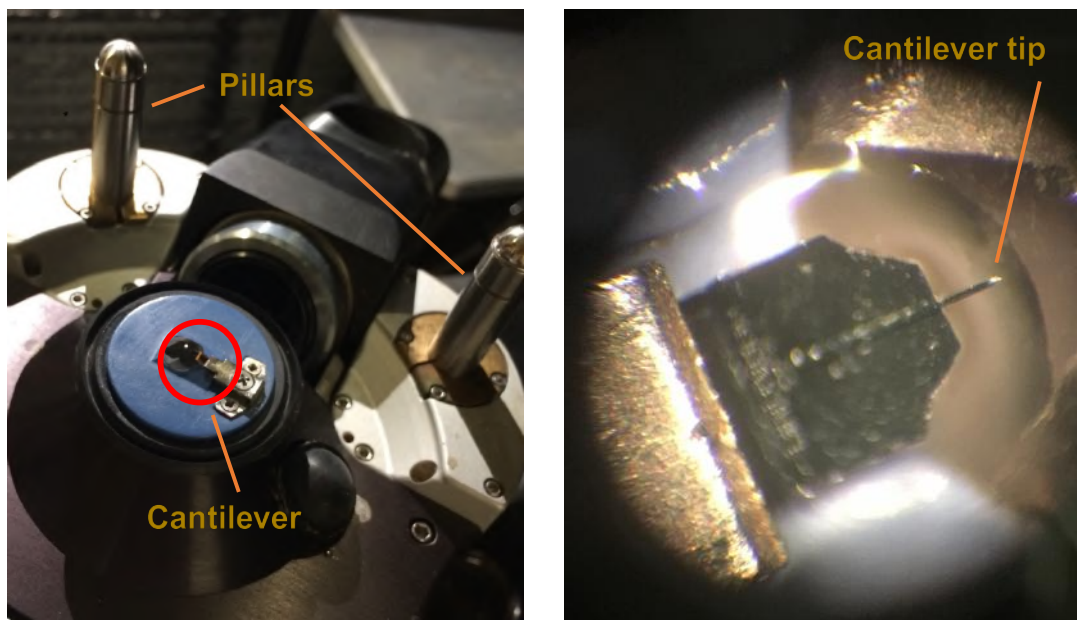


*Figure 32: Installed cantilever probe to the head slot (left, head lying upside-down), and view of the cantilever under a microscope with 10x magnification (right)*

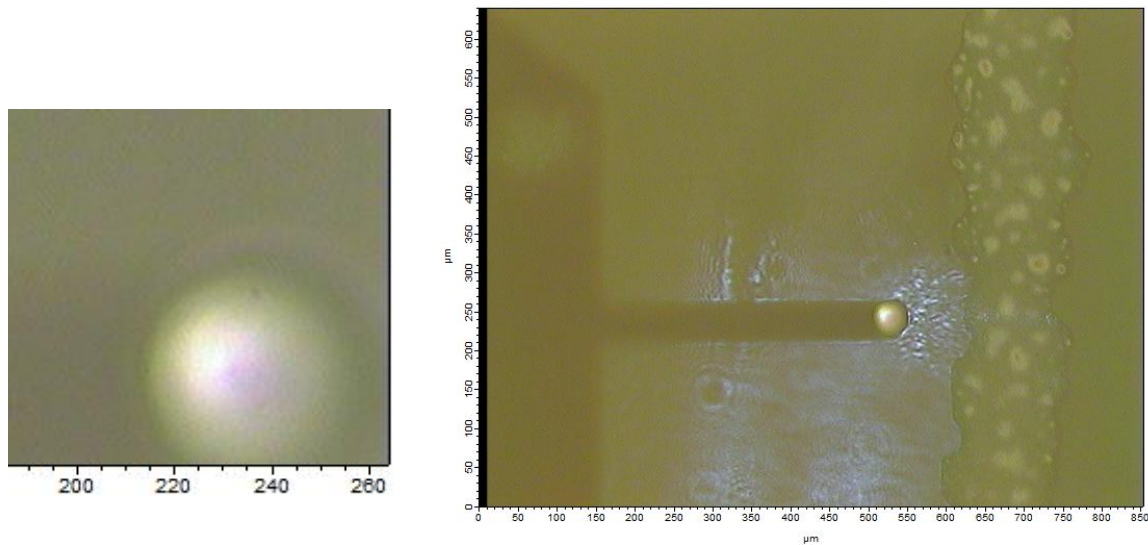


Figure 33: Visualization of the cantilever tip head under the AFM microscope (right), and measurement of the spherical diameter of the tip, on a micrometer scale (left)

### 4.3.3. Calibration

The instruction protocol of the instrument prescribes to calibrate the optical lever sensitivity (invOLS), which connects the value of the voltage signal generated in the photodiode for a given amount of cantilever deflection [97].

As the measurements took place in aqueous environment, the cantilever and the laser beam had to be calibrated in the same aqueous environment as well. The calibrations were meant to be made on a counterpart, or a calibrating sample, which represents a much higher hardness with several orders of magnitude than the cantilever probe [97]. Therefore, a transparent, blank glass slide was chosen to be most suitable for this purpose. It was important to have no compliance from any surface which the tip reaches so that any deflection of the laser signal and deformation of the cantilever would exclusively correspond to its stiffness properties. The slide was fixed to the base stage with magnets, and a patch of water was added on its surface, into which the cantilever was immersed as the head was slowly being laid into its place on its pillars. Thus, a neutral fluid environment was created, the same in which the experiments would take place.

On the computer, the software Igor Pro 6.37 (WaveMetrics, Inc. Portland, OR, USA) was initiated. At first, calibrations for the virtual deflection were executed: this means the coupling of the deflection signal (from the laser beam) with the Z-movement. Their relation is not constant, because the exact alignment of the light beam on the lever changes with z-movement.

This variation had to be gotten rid of by this first calibration because it would influence the invOLS calibration. The start point of the Z-movement was set to the furthest possible,  $-1.78 \mu\text{m}$ , as well as the *force distance* (the length of the Z-movement exerted from the piezo), to  $28.42 \mu\text{m}$ , so that a Z-range of  $30.1 \mu\text{m}$  was reached. With these values, a graph of the deflection of the signal on the traveled Z-distance was created, and the value of the slope was extracted. The software used this value automatically for the later calibration of the invOLS.

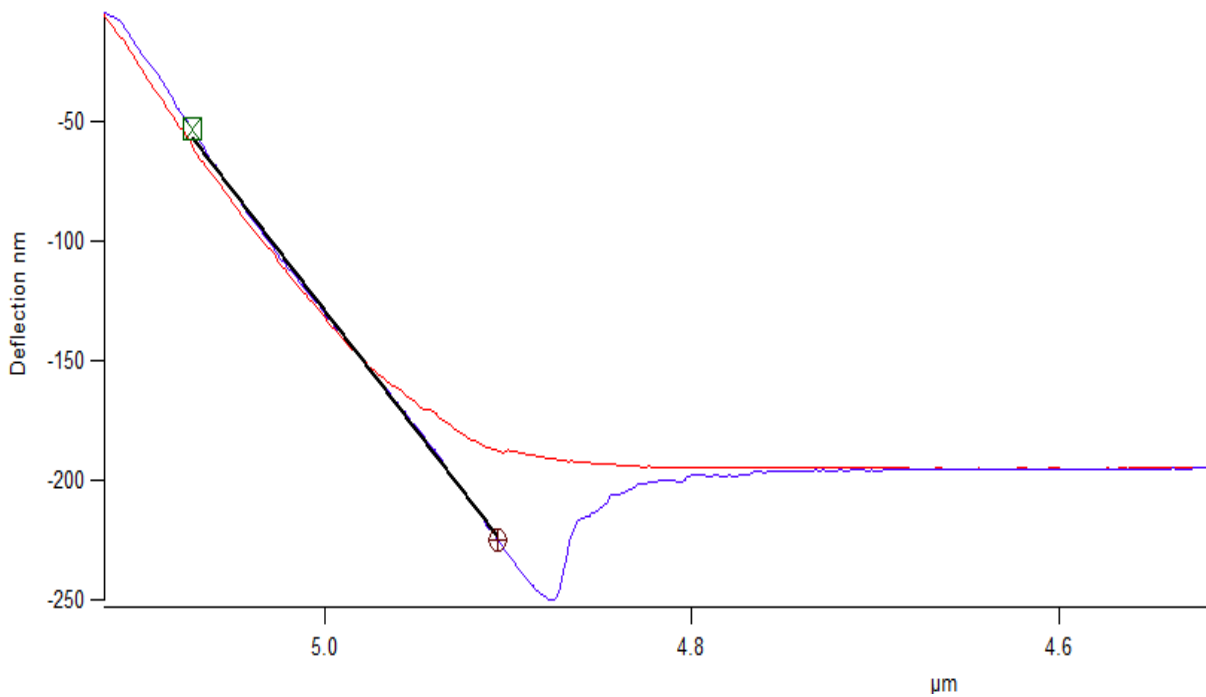


Figure 34: Resulting plot from the invOLS calibration

Second, the invOLS calibration itself took place. It is a similar procedure, except that the cantilever had to be carefully brought onto the hard surface of the slide this time, and a “blank indentation” had to be made with the *force distance* of  $1 \mu\text{m}$ . That is, the piezo demonstrated a movement of  $1 \mu\text{m}$  towards the surface, which produced a bending of the cantilever, as its tip was leaning on the surface. This produced an almost linear slope both in the approach and retract phase of the Z-motion, on the deflection – Z-distance plot. This slope generated the calibration value for the relation of the deflection with respect to the generated voltage signal at the light beam optical detector.

Last, the actual spring constant of the cantilever was determined by assessing the power spectral density (PSD) of the thermal noise fluctuations. This was done by inducing thermal noise and analyzing the resonance of the cantilever by the deflection signal. The signal was Fourier-

transformed by the software and the amplitude over the frequency was plotted. The first harmonic, the lowest frequency with the highest amplitude (power) was identified and fitted with an approximation function. From that, the spring constant of the cantilever was computed by the software, and yielded:

$$k = 280 \frac{pN}{nm} = 0.28 \frac{N}{m}$$

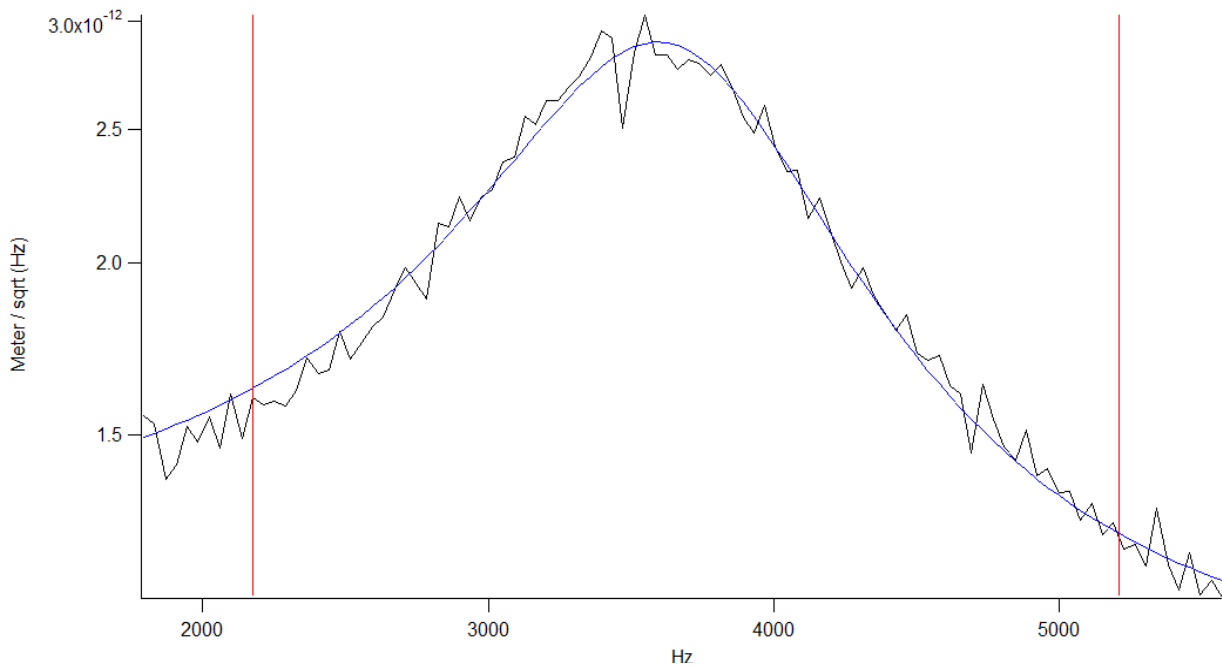


Figure 35: Thermal graph, fitted with a curve for the approximation of the cantilever stiffness

#### 4.3.4. Preparing the specimen

The specimen of a 12  $\mu m$  thick cross-section of superior frontal brain cortex on the glass slide was fixed on the stage of the base with two magnets, with the head unit not yet installed. The slide was positioned so that approximately the stripe of the grey matter would be under the cantilever. From a pipette, purified water in a careful but sufficient amount was added onto the surface of the specimen, to keep the specimen hydrated, and on purpose of the advantages of measurements in water, described in section 4.3.1.

The software has several interfaces, such as a real-time video screen of the CCD cameras, with the help of which the specimen and the cantilever tip position could be constantly observed. Using this feature, the specimen was positioned to bring the edge of the pia mater in the center.

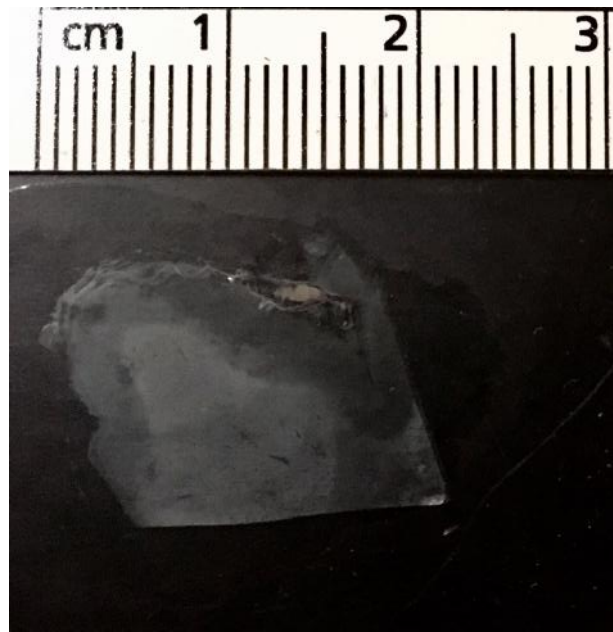


Figure 36: Cross section of the specimen prepared for AFM indentation

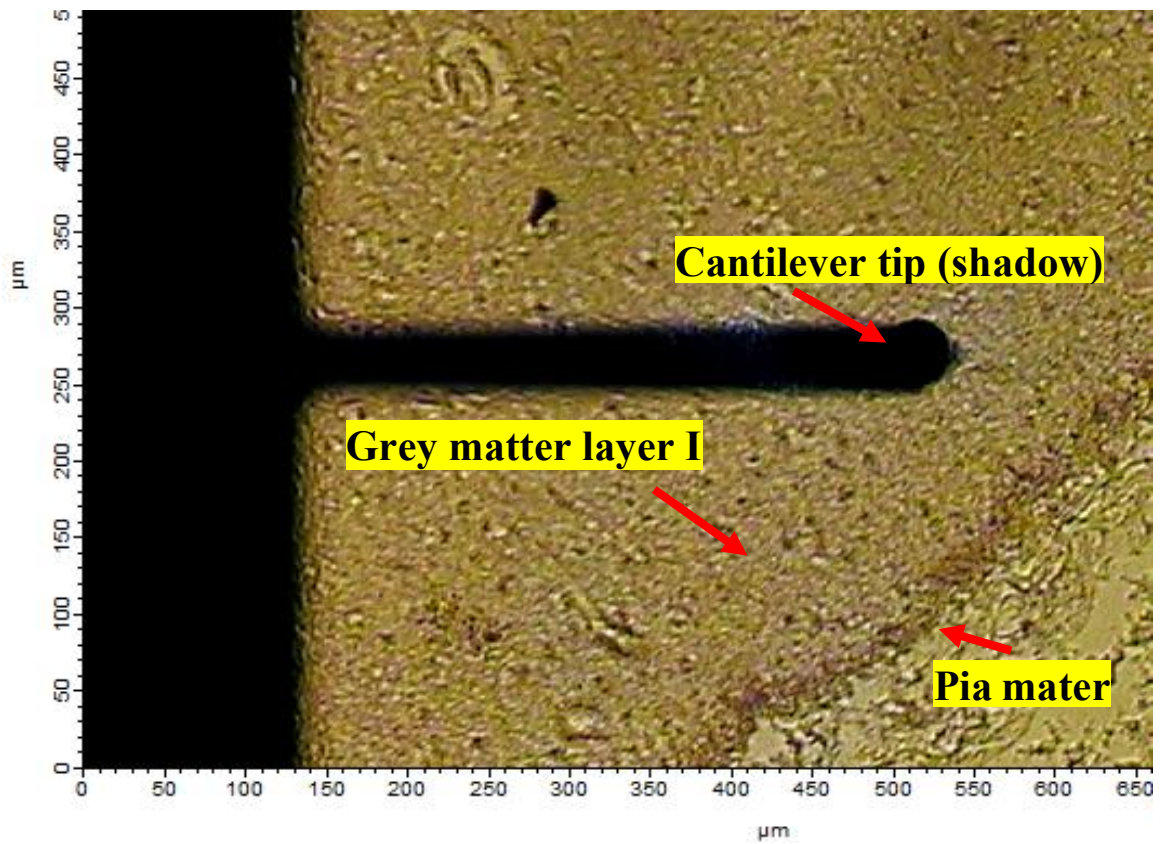


Figure 37: Image of the specimen under the AFM instrument, with pia mater, distinguishable layer I, and the shadow of the cantilever tip close to the specimen surface



The different layers of the grey matter neocortex could be identified and constantly assessed based on the knowledge gained from the microscopic visual assessment, of the exact same specimen. Measurements were to be conducted through the entire cortex cross-section, from Layer I to Layer VI, to obtain data from the 6 different layers of the neocortex. One series of measurements through the thickness of the neocortex, from I to VI, is declared as one sample. In Figure 37, the specimen is prepared for the first measurement on layer I, starting from the pia mater. In Appendix C, all images of the transitions between layers are provided.

The measurements had been designed as follows: six different regions were defined on the specimen for applying a measurement series across layers I to VI. These represent six different samples, (S1 - S6) of the specimen of the superior frontal neocortex. Each sample would represent a separate examination on the same area of the frontal cortex, and each would contain measurement data of all of the six layers. However, not all obtained data was feasible and usable, as we would experience later on.

## **4.4. Measuring the E-modulus**

The following procedure for conducting an indentation and creating a force-displacement curve was established: first, the tip was brought close to the surface, making sure that the neutral deflection stays zero, and constantly monitoring the piezo Z-voltage. Touching the surface is signaled by a change in the Z-Voltage, and the deflection Voltage (towards the trigger point of 0.1 V, suggested by [30]). If these values started to change, the tip would be already touching the surface of the sample. The tip was left at the point where the values are already altered slightly, to overcome any inaccuracies. Having the tip on the surface, the “single force” measurement could be initialized in the control panel of the software. Following parameters were set: the start distance, the *force distance*, displacement velocity, and trigger value.

### **4.4.1. Force distance**

While the start distance sets the position where the piezo would start approach, the *force distance* defines the distance both in approach and retract which would be covered under load by the piezo against the resistance of the material. This was one of the adjustments which were used to set the indentation limit, along with the *maximum measured force*, since we did not want to exceed a certain limit of depth, to be able to apply the theories introduced in 3.7.3.

It was important to be able to apply the approximation of small strains (under 0.1 [11], [32]), and consider the sample having an infinite thickness and volume, with respect to the indentation depth (max 10% of thickness [27]). Since we had a specimen thickness of  $12 \mu m$ , the maximum depth was defined as  $1 \mu m$ , which represents 8.3% of the thickness, which still was not actually reached in a lot of cases. The strain in the specimen undented by a spherical tip is computed by [95]:

$$\varepsilon_{max} = \frac{h_{max}}{2.4a} \quad (31)$$

based on the Hertzian theory of assumed elasticity [98]. Using (31), after computing  $a$  with formulas (25) and (26) with the indenter radius of  $19 \mu m$ , the  $\varepsilon_{max} = 0.1$  strain level allowed for a maximum depth of  $1.055 \mu m$  which coincided with the other constraint condition (max.  $1 \mu m$ ) regarding the depth.

#### 4.4.2. Trigger

After setting the displacement velocity, which is basically the speed for the approach and retract phase of the Z-piezo movement of the head, the trigger value was adjusted.

The value of any measurement variable could be used as a trigger (deflection in  $nm$  or volts, force, displacement, etc.) By default, if this pre-set value was reached during actuation, the approach ended and the retract phase would be initialized. If a dwell program had been set up, reaching the trigger level would mean the beginning of the dwell phase.

Basically, two kinds of measurements were conducted using these adjustment possibilities: one is called a “single force” measurement, with a complete, simple run of approach and retract. The end of the approach phase, which means the maximum traveled distance, is defined by a *maximum force* trigger. Although a trigger for the maximum depth of  $1 \mu m$  would be obvious, it could not be realized precisely, because the approach distance is in most cases not the same as the *force distance* and also not the same as the indentation depth. This is due to minor surface interaction forces and surface inhomogeneity or debris, which would have influence and would already trigger a load on the cantilever and signalize the beginning of the *force distance* traveled, when the material had not yet been actually penetrated. Thus, to have an unmistakable measure, the approach was allowed to have a straightforward run until it reached the *maximum force*, which was set to a value that would certainly be reached below a depth of  $1 \mu m$ .

After some preliminary measurements, this optimal trigger value was observed to be around a *maximum force* of 20 nN. In [28], it is suggested to set a 27.5 nN *maximum force* for a similar indenter diameter. For the sake of a safe measurement, 15 nN was set as the *maximum force* limit. This type of measurement was employed to obtain samples S3, S4 and S5.

The other type of measurement was the “indentation dwell”. In that case, the trigger was used to capture the moment of the beginning of deformation, when the indenter touches and takes up resistance load by the surface of the specimen. The touch signal was captured by a vast trigger force (S1, S2) or deflection voltage (S6, Table 1). The trigger was then used to initialize a pre-set indentation process, where an exact depth, along with load, hold and unload phases could be specified. In this case, the value of the *force distance* was used as an upper limit for the indentation. For instance, if the force trigger only started where a certain indentation depth of over 400 nm was already reached, more than an additional 600 nm indentation meant an overall depth exceeding the limit of 1 μm. This could be constrained by the *force distance*.

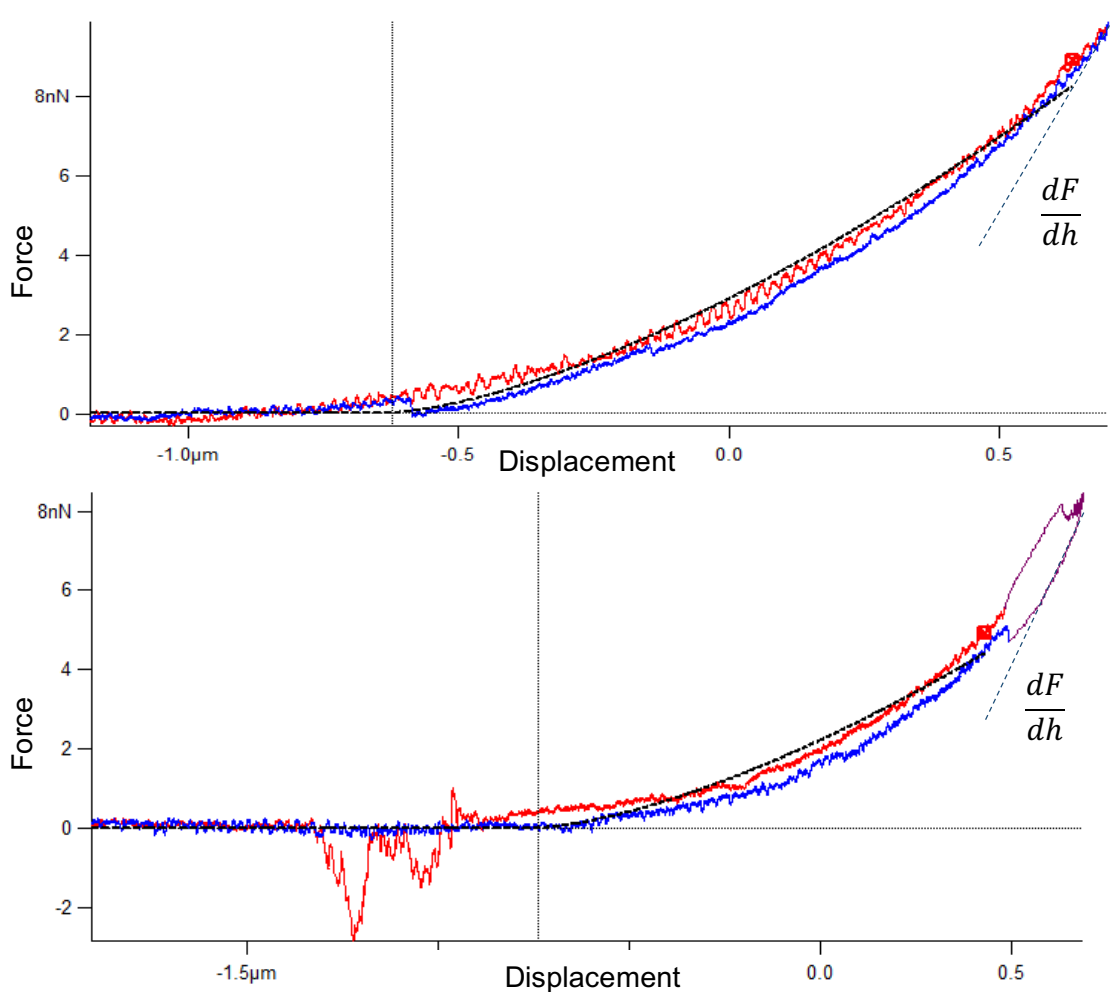


Figure 38: Force-displacement plots of "single force"(top) and "indentation dwell"(bottom) techniques

The two approaches were observed to lead to similar measurement outcomes and similar force-displacement graphs (Figure 38).

As described above, in Chapter 3.7.3, the elastic modulus of the material can be extracted by creating a force-displacement curve demonstrating an approach (load) - retract (unload) indentation, and measuring the slope on the initial part of the unloading curve [9], [15]–[17], [95], [102]. The slope was thus to be found on the initial linear segment of the unloading part of the indentation curve in the case of an “indentation dwell” measurement and on the initial linear segment of the unload/retract phase of a “single force” measurement (Figure 38).

To obtain reliable measurements from the slope, a fast unloading was essential in the case of the soft, viscoelastic material in this study to recall its purely elastic behavior, for it is known, that the instantaneous modulus  $E_0$  prevails at the shortest possible loading, when not letting for any creep behavior. According to Cheng et al. [8], a fast unloading is achieved when the time duration of linear unloading is about 0.1–0.01 times the relaxation time of a viscoelastic material. Although the measurements were executed with different approach and retract velocities, this constraint was always taken into consideration, using relaxation values of previous researches as expected values, although those reached from 1 to 40 seconds. In the discussion section (Chapter 0), the duration of the initial slopes will be compared to the obtained relaxation times.

Parameters	S1	S2	S3	S4	S5	S6
Start dist. [ $\mu m$ ]	15	23	23	23	10	23
Force dist. [ $\mu m$ ]	1	3	3	5	5	5
Preset max. force as trigger [nN]	-	-	25	15	15	-
Preset trigger	Force > 200 pN	Force > 500 pN	-	-	-	Defl. > 0.1 V
Preset max. displacement [nm]	800	800	-	-	-	1000
Displ. vel. [nm/s]	100	50	50	200	300	4000
k [N/m]	0.29	0.29	0.29	0.29	0.29	0.29

Table 1: Measurement settings employed in the case of the samples S1 to S6

The six samples were taken with the adjustments listed in Table 1. At the first three samples, different approaches had been tried out, whereas the second three measurements show up more consistent data, due to being conducted with already more elaborate setups.

Apart from that, the first three samples contained a lot of faulty measurements, and due to limited resources and time, a scarce amount of measurements could only be made. Some of them must have been canceled because of instrumental errors, or unfeasible results, such as an unusually high contact stiffness by several orders of magnitude.

#### **4.4.3. Calculation methods**

The force-displacement data for all measurements were collected on the system computer. Although the given software was capable of computing an approximate elastic modulus for force-displacement data, this built-in feature demonstrated a high proneness to errors. To obtain more exact results, Young's moduli were computed manually from the data.

Important variables for computation of the E-modulus were the actual full range of force increase ( $F$  [ $nN$ ]), not to be mistaken with the measured *maximum force*, and the actual full indentation depth ( $h_{max}$  [ $\mu m$ ]). Apart from that, the inclination of the initial unloading slope, (contact stiffness  $S$  [ $N/m$ ]) was employed.

##### **4.4.3.1. Zero contact point**

One of the calculation artifacts was caused by the unreliable identification of the zero contact point for the theoretical start of the loading segment by the software's algorithm. The zero contact point is an important measure on the force-displacement curve since the actual force and displacement ranges must be measured starting at the actual point of initial contact (displacement  $Z_0$ , Force  $F_0$ ), which often does not coincide with the measured max. values. In a lot of cases, adhesion and surface tension effects altered the zero-point identification. If those forces which act in the opposite direction had had to be overcome first, the curve started in the negative force range, and the indentation depth would have been counted from an earlier point than where the actual indentation started. If the deflection from the cantilever had been altered by these surface effects, it was a reason to produce a negative force value. According to Oliver and Pharr [6], built-in computational techniques for identifying the initial contact point by extrapolation algorithms produce unreliable data. They suggest the approach to observe the entire mechanical response of the system on the force-displacement plot [6].

For this purpose, the point of contact had to be identified at the point of the initial repulsion force, from which the slope of the curve starts to increase drastically. This method was successfully applied in [16] and [17] where, after identifying the point of initial contact, the curve was computationally upshifted, and the maximum force and depth ranges were extracted.

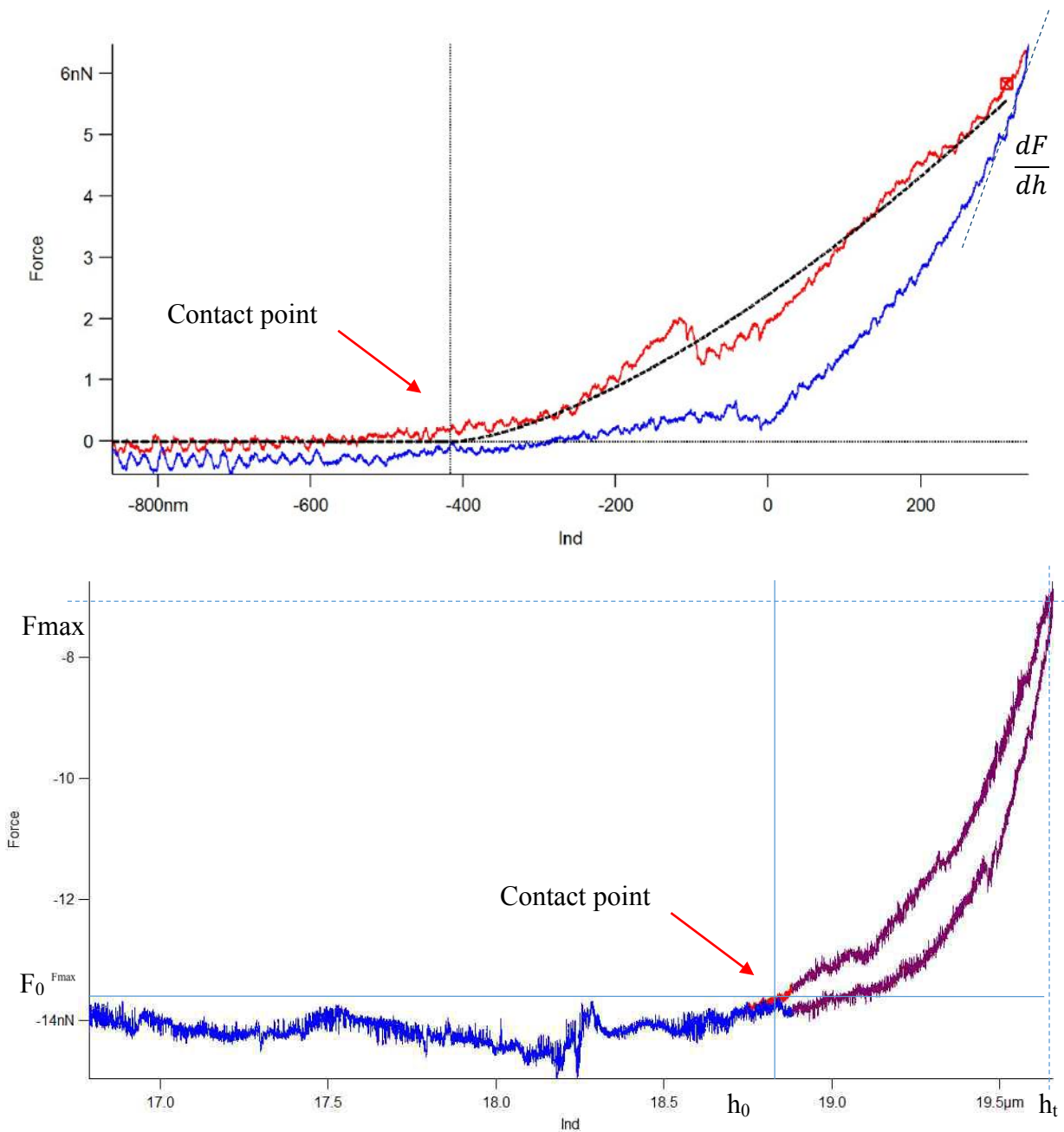


Figure 39: Force displacement plot with a reasonable zero-contact point with no need for correction (above) and a plot starting in the negative range with the need for manual zero-contact point identification (below)

#### 4.4.3.2. Computed variables

In current research, the computation of the actual measure of maximum force  $F$  was established manually, by simply extracting the absolute height of the force interval  $F_{max} - F_0$  (where  $F_{max}$  is the terminally measured maximal force). The actual indentation depth  $h_{max}$  was similarly measured from the beginning of the contact point of the curve, and the absolute value of the interval  $h_t - h_0$  was taken as the depth  $h_{max}$ . As introduced in 3.7.3 and 4.4.2, the measure  $S$  was extracted manually from the initial unloading slope, by building the ratio  $dF/dh$ .

#### 4.4.3.3. Young modulus calculation

For the calculation of the Young modulus, the formulae (24) was employed, including the variable  $S$  and the contact area  $A$  which is defined by the contact radius  $a$  and contact depth  $h_c$ . For the values of  $F$  and  $h_{max}$ , the corrected values discussed in 4.4.3.2 were utilized.

The contact depth  $h_c$ , and thus the contact area  $A$  and radius  $a$  were computed in two different ways, as discussed in 3.7.3, employing (25) and (26) in the classic Oliver-Pharr approach [6] on the one hand, and (27) and (28) based on the approach of Cheng [8].

#### 4.4.4. Statistical assessment

All statistical tests were implemented in the software Microsoft Excel for Mac, (Version 15.32, Microsoft Corporation, Redmond, WA, USA), additionally utilizing the add-in Real Statistics Resource Pack (Release 5.4, Copyright 2013–2018, Charles Zaiontz. [www.real-statistics.com](http://www.real-statistics.com)).

##### 4.4.4.1. Outliers

The raw measurement data was cleared from outliers, first within each of the samples. The process started with checking for normality with Shapiro-Wilk tests. If the data within a sample was not normally distributed, Chebyshev's test (see 4.6) was employed. If a normal distribution could be proven, a Z-test within a range of 2.5x standard deviation was utilized, as well as a complex Grubb's test.

Outlier data for E-moduli, detected by applying the above tests, were deleted from the samples.

#### 4.4.4.2. Comparative statistics

No significant difference between the Cheng and Oliver-Pharr method for computing  $E$  from the measured force-displacement plots was detected after comparing the values yielded by the two methods with one-way ANOVA within each sample. Nevertheless, the Oliver-Pharr method yielded slightly lower means at all measurements, lying closer to reality regarding experimental values provided by former studies [29]; thus, the values calculated by the Oliver-Pharr method were taken as valid and employed further in this study.

Then, ANOVA tests were executed for checking the difference of the E-modulus means between layers (I, II, ...VI) within each sample separately.

After checking the difference between layers inside each sample, the difference between the samples was checked by ANOVA. This assessment was carried out to examine whether it is possible to cumulate the data of different samples eventually. For this, the average value of each layer within a sample was taken, and from that, the average for one sample was built. This approach assured to avoid the artifact that some measurement series have more data points of a particular layer than the other series, which can distort the entire average of one measurement series thus making the different series incomparable to each other. Thus, having a mean value for each layer, the different measurement series (samples) were compared with an ANOVA test, by only employing the mean values for each layer in each sample as variables. As not all measurement series (i.e. samples) had feasible and usable data for all layers, sample S1 was canceled, due to having very few, stochastic data and high variance. Apart from that, the average of the sample was 3-4 times higher than the average of other samples, as it was apparent from the comparison (Chapter 5.2). From this point, S1 was excluded from the calculations and the results. To be able to check the difference between all samples S2...S6, the layers pulled into the ANOVA test had to be reduced to the ones which had values present in all samples. Thus, only layers I, II, and III were analyzed. ANOVA yielded difference with  $p < 0.05$  among the samples. Tukey-Kramer post hoc tests demonstrated that each of the samples S4, S5, S6 are different from S2 ( $p = 0.05$ ), and similarly from S3. S2 and S3 means were lying close to each other. Data for layers I, II, III, and V, were present in 4 samples, S2, S4, S5, and S6. Similarly, the comparison of averages was executed with ANOVA again, by using means of the four mentioned layers this time. The presence of a difference was detected again ( $p < 0.05$ ). Tukey-Kramer post hoc test yielded, that each of the samples S4, S5, S6 differ from S2 ( $p = 0.05$ ), which strengthened the former result, even when taking into account more layers.



S4, S5, S6 had reasonable mean values lying close to experimental values (see Chapter 5.2), considering former researches about general grey matter E-modulus [29], [48], lying in a range of 1200 – 2000 Pa. This implied that one cumulated group could be built, from the values of the samples S4, S5 and S6, having a cumulated average of 1.78 kPa, calculated from the mean of each layer.

After creating the cumulated data series, and assorting measurement data from the samples to the appropriate layer, the difference between the layer means within the new cumulated data series was checked, with one-way ANOVA test. The results will be discussed in Chapter 5.2.

## 4.5. Measurements for viscoelastic parameters

For the extraction of the viscoelastic properties, a procedure based on the methodology for viscoelastic relaxation discussed in Chapter 3.7.3 was implemented with the AFM instrument. As implied by several researchers [11], [30], [86], a relaxation experiment was built by creating a specific ramp for a pre-set indentation depth of 1  $\mu\text{m}$  representing a predefined strain and implementing it in an indentation setting on the AFM instrument. The ramp was constructed as follows (Figure 40):

- Phase 1: an increase of depth from 0  $\mu\text{m}$  to 1  $\mu\text{m}$ , in 0.1 seconds. Literature and theory, e.g. [86], [11], prescribe an instantaneous displacement for a relaxation test, represented by a Heaviside function. This could be realized at high accuracy by a sudden increase in displacement, 10  $\mu\text{m}/\text{s}$  in this case, as suggested by [30], which do not allow for time-dependent creep behavior at the increase of displacement.
- Phase 2: holding the displacement at the same value, 1  $\mu\text{m}$ , for 10 seconds. This was enough time to observe relaxation behavior at this amount of strain. The displacement was held constant by a control loop mechanism of the instrument, constantly measuring load and displacement on the piezo actuator.
- Phase 3: decrease of the displacement from 1  $\mu\text{m}$  to 0  $\mu\text{m}$ , in a slighter slope with a duration of 1 second. A withdrawal of the indenter in a slower pace is suggested by [30].

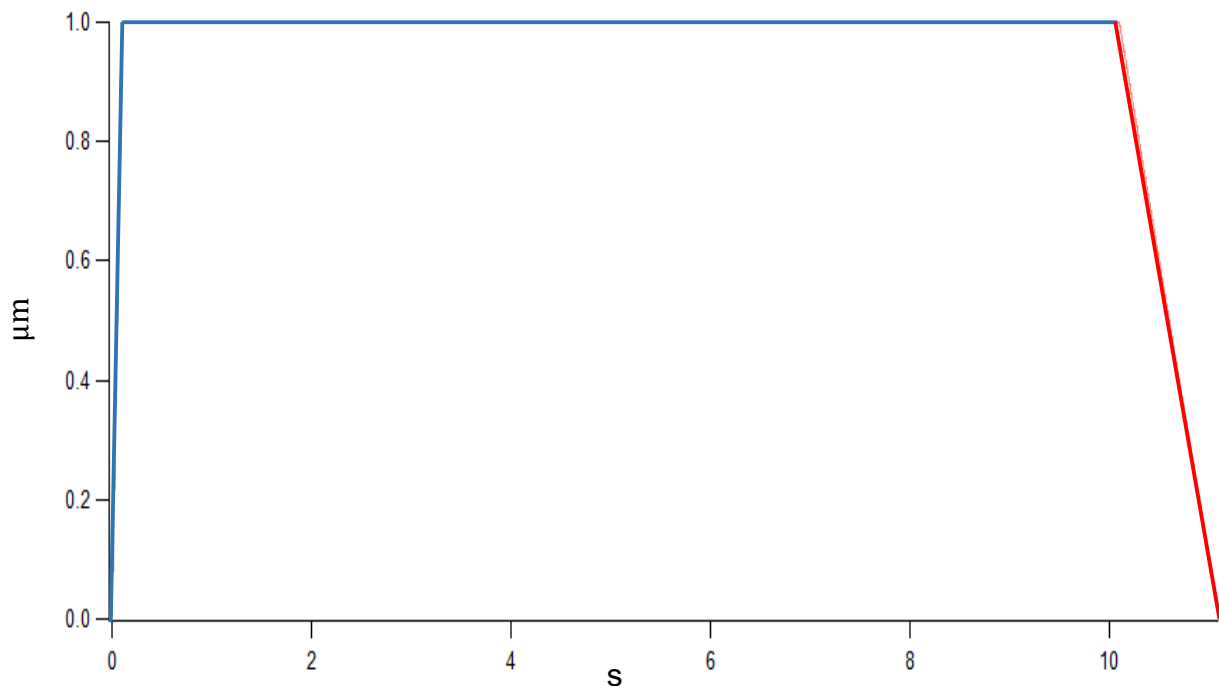


Figure 40: Constructed indenter ramp for relaxation experiments

Eight sample areas were identified on the specimen slice and examined including each layer on the specimen of the superior frontal cortex. The adjustments and parameters of the instrument had been pre-set as follows:

- the start distance was set to 15  $\mu m$ .
- The *force distance* was set to the highest possible, 5  $\mu m$ , to give enough range for the indenter in Z-direction, to reach the surface, indent it and reach the indentation depth of 1  $\mu m$ .
- The approach velocity was set to 1  $\mu m/s$ .
- To be able to identify the arrival of the indenter on the surface, the trigger control was set, using the deflection voltage signal to signalize a bending of the cantilever head when reaching the surface, by the voltage signal exceeding 0.1 *volts*. By reaching the trigger, the pre-set indentation ramp was induced.

The measurement procedure was carried out as follows:

- The tip was engaged and the neutral deflection value calibration was set to zero
- The tip was brought onto the surface, the touch signalized by the Z-Piezo value change in the software, as the neutral deflection goes up to 1 *volt*.
- Executing the measurement with the pre-set adjustments, by clicking “single force”
- After the ramp is over, the indenter retracts, withdraws. Moving to the next sample.

Time-dependent force plots were created utilizing the above protocol for all layers for all samples, in the software.

#### 4.5.1. Computational methods

As planned, the relaxation phase of the force-time  $F(t)$  plot at the hold part of the ramp, was aimed to be fitted with a sum of exponential functions, to obtain a Prony-series approximation. The start (end of the “jump”, sharp sudden decline, representing an initial elastic relaxation) and end (end of the nearly constant phase of the decay, just before the decrease step) of the interval on the curve was marked (Figure 41), and fitted in the software with a 2-term exponential function the form:

$$F(x) = Y0 + A1 \cdot e^{-\frac{x-x0}{\tau1}} + A2 \cdot e^{-\frac{x-x0}{\tau2}} \quad (32)$$

With  $x$  representing the time variable. To represent only that exact interval on the entire force plot, a shifted fitting function (shifted to the start of the relaxation decay,  $x0$ ) was utilized in the software. As a result, the slope before and after the relaxation phase is “cut out” of the consideration, and the parameters for the fitting function is only computed for the relaxation phase, not for the entire force plot.

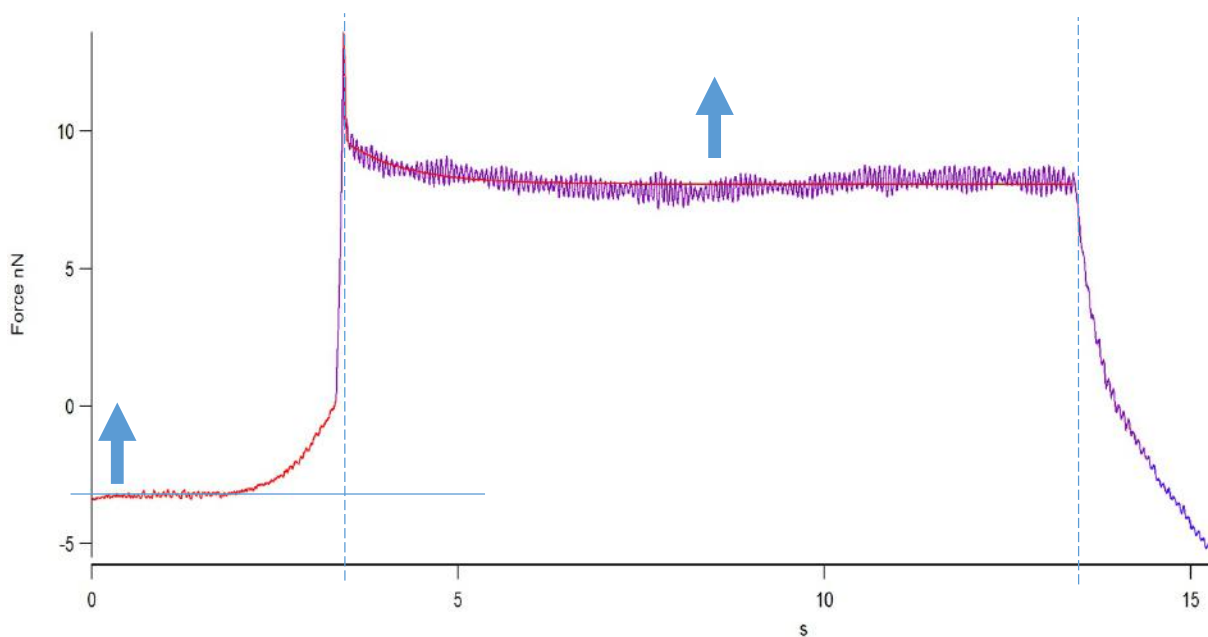


Figure 41: Resulting Force-Displacement plot from the relaxation experiments. Start and end of the relaxation phase is marked by dashed lines, as well as the zero-point upshift by arrows. The purple curve represents the captured behavior, where the red line is the exponential fitting to the curve.

#### 4.5.1.1. Zero-point correction

A zero-point correction had to be carried out, for the obtained curves were negatively biased on the force axis (Figure 41). This was due to the error that the initial value of the deflection signal, from which the force is computed, did not start exactly at zero. Using the photodiode knob, the neutral deflection value was set close to zero, but starting exactly from zero could never be realized. In this case, this causes a remarkable change, for we fit the decay at the hold phase and the absolute value of the function is influenced by the vertical bias. Therefore, it had to be shifted back to the zero point. At the approach, in the beginning, before phase one, no forces should have occurred on the cantilever (the curve is constant). However, if the plot started and remained constantly at a nonzero value (always somewhat below zero) before phase one, it had to be shifted back to zero subsequently. For this purpose, the value of the constant part of the curve in the approach phase was extracted and subtracted from the constant  $Y0$  of the fitting function. E.g. in the case of a  $-3 \text{ nN}$  downward bias as it appears in Figure 41,  $Y0_{new}$  would be:

$$Y0_{new} = Y0 - (3 \cdot 10^{-9}) = Y0 + 3 \cdot 10^{-9}$$

#### 4.5.1.2. Calculating the shear function

After carrying out the correction for all measurement data, the corrected raw fitting function  $F(x)$  was converted to an expression for  $G(t)$ , based on formula (30).

The parameters  $Y0_{new}$ ,  $A1$ , and  $A2$  were given as force values. These were converted to  $G$  shear stress values by formula (30), as suggested by Efremov et al. [100], who also substituted the time-dependent force values to the Hertz-formula, and obtained time-dependent shear functions.

After carrying out these calculations, shear functions were obtained in the form:

$$G(t) = G_{\infty} + G_1 e^{-\frac{t}{\tau_1}} + G_2 e^{-\frac{t}{\tau_2}} \quad (33)$$

With the time-shift already cancelled,  $G_{\infty}$  as the infinite modulus, two relaxation times  $\tau_1, \tau_2$ , and  $G_1, G_2$  as corresponding relaxation parameters. Reformulating to form (17) yielded:

$$G(t) = G_0 - G_1(1 - e^{-\frac{t}{\tau_1}}) + G_2(1 - e^{-\frac{t}{\tau_2}}) \quad (34)$$

Normalizing by the instantaneous modulus  $G_0$  yielded the general dimensionless form of the Prony-series, formula (18), as employed in [88]:

$$g(t) = 1 - g_1(1 - e^{-\frac{t}{\tau_1}}) + g_2(1 - e^{-\frac{t}{\tau_2}}) \quad (34)$$

Which is a dimensionless function of time, characterized by the Prony-pairs:  $g_1|\tau_1$ ,  $g_2|\tau_2$

For all measurements, these calculations were carried out and these 4 Prony-parameters (Prony-pairs) were extracted. These were later statistically wrapped up and used for the material models set up in the FEM simulations.

## 4.5.2. Statistical analysis

To yield representative and feasible information from the samples, the obtained data had to be analyzed not only within each layer but also collectively, to be able to detect eventual outliers, get an idea about the distribution of the data. Then, most importantly, an average was established for each layer.

### 4.5.2.1. Outliers

The raw measurement data was analyzed as one distribution and was cleared from outliers, based on different obtained variables of the data ( $Y_0$ ,  $G_1$ , or  $g_1$ ). The process started with checking for normality with Shapiro-Wilk tests, where it was found that none of the measurements were normally distributed. Therefore, Chebyshev's test (see 4.6) was employed for outlier detection. Additionally, negative modulus values, and values which were distinct with several orders of magnitude were sorted out.

After sorting out the first outliers from the data, first, using the variable  $Y_0$  of the raw fitting function, other variables ( $g_1$ ) became normally distributed and could be analyzed by more sophisticated methods. Thus, additional outliers were detected based on variable  $g_1$ , using Grubb's test.

Each data group of outlier data detected by applying the above tests were deleted from the samples.

#### 4.5.2.2. Comparative statistics

The cleaned data, focusing solely on the Prony-pairs, was organized by assorting the measurements of all samples to the corresponding layers, thus creating a measurement series for each layer.

On these groups, one-way ANOVA tests were conducted, checking for the difference of layer means of each particular Prony parameter of the four.

### 4.6. Statistical methods

The statistical calculations employed in Chapters 4.4 and 4.5 were carried out based on following procedures:

Chebyshev's test procedure for not normally distributed data was first conducted with  $p = 0.1$ , significance level, to roughly sort out outliers, then on the preliminary cleaned distribution with level  $p = 0.05$ , based on suggestions of Amidan et al. [103]. Afterward, a manual additional assessment was carried out by applying the range of 4 standard deviations, which keeps approximately 94% of the data inside limits, as suggested by Lohninger [104].

Normally distributed data were checked for outliers both with Grubb's test, which can only be employed for normal distributions and manually by applying a limit of 2.5 standard deviations, as suggested by Lohninger [104].

ANOVA was employed to compare the means of different layers, and to compare the overall means of samples, based on its proven success in similar applications [32], [105].

After yielding results for the presence of a significant difference by ANOVA, the particular distributions between which the difference is present were detected by post-hoc tests. According to [106], a Tukey-Kramer test is the most reliable in the case of different sample sizes. It has been employed for similar problems in [48] and [107] on the same field of research.

In case a Tukey-Kramer test was not eligible (because of a desired significance level  $p > 0.1$ ), as well as for double checks, Bonferroni corrected t-tests were employed (unequal variances, two-tailed), as applied by Qian et al. [31], and Finan et al. [32].

## 4.7. Computational methods

### 4.7.1. Global head model

A complete model of the entire head was used to obtain the stress state in the case of a random head impact. This model was created at CCNY using the MRI images of a human head, obtained from a cadaver of a human aged in their late fifties. The geometry of the model was generated in Solid Works 12 (Dassault Systèmes SE, Vélizy-Villacoublay, France) and Abaqus 2016 (Dassault Systèmes SE, Vélizy-Villacoublay, France) was employed for mesh generation and analysis. This model included a geometrical representation of the skull, dura mater, subarachnoid space (SAS) and the brain (Figure 42 ).

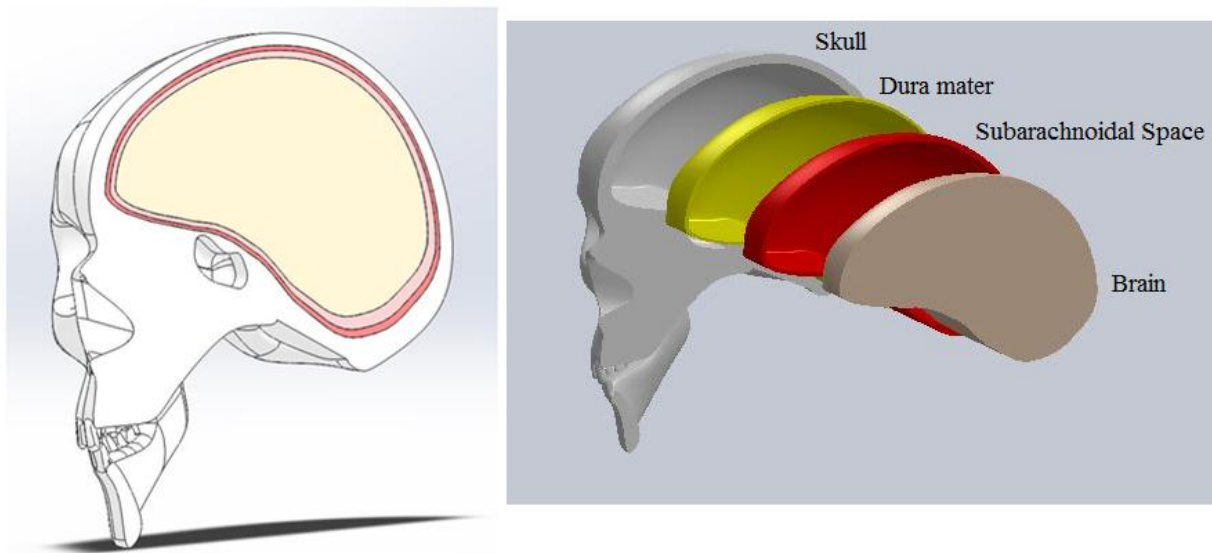


Figure 42: CAD-model of the human head used to build the global simulation of a head impact

The finite element model was validated based on Nahum's experimental data [51] where several cadaveric frontal head impact experiments were performed in a special setting, measuring certain quantities inside the head compartment as well as the acceleration pulses. In the case of the FEM model, the same experiments were carried out *in silico*, and the model found to be valid based on similar outcomes of the same impact setting.

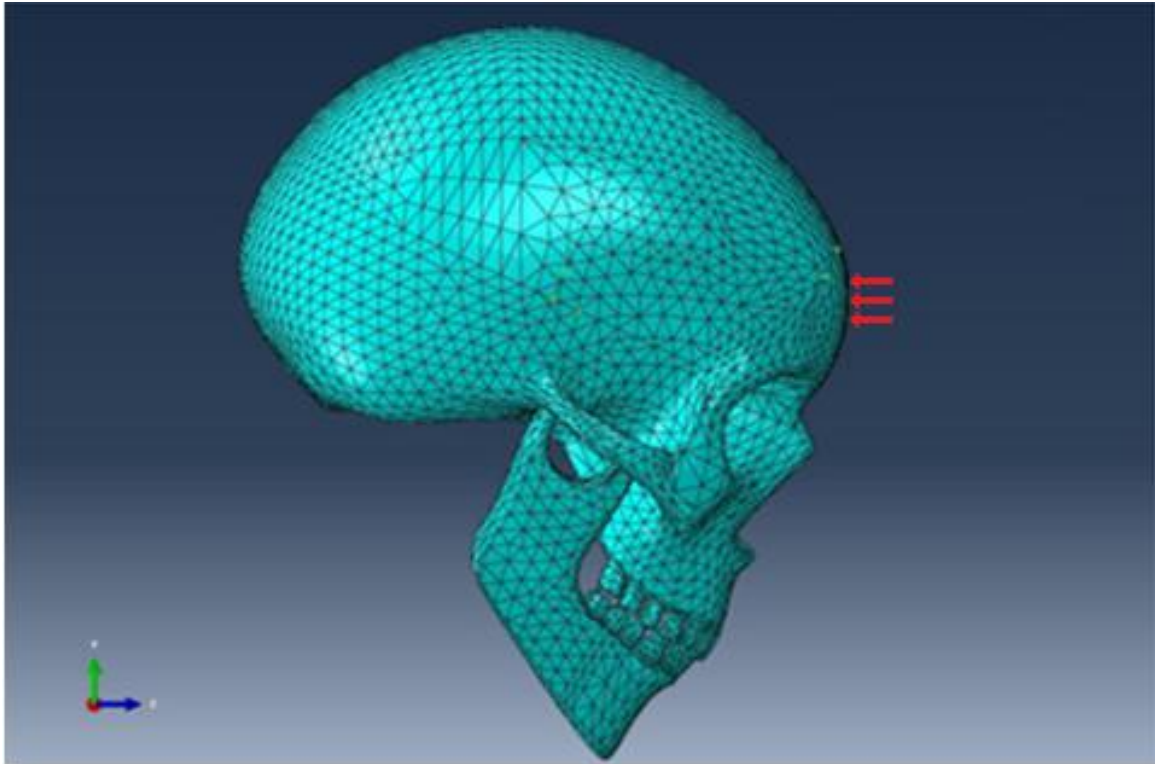


Figure 43: Validation of the FE-model in silico, after Nahum's test, applying a load on the forehead

The model was modified so that the brain resembles a size characteristic to the age of the cadaver from which the specimens for material experiments were obtained. This was achieved by scaling up a copy of the existing brain part by 1.03058. This results, in a residual 8.3% of extraventricular (cortical) CSF volume resembling the brain size of humans around 60 years old [61], [108].

#### 4.7.1.1. Meshing

The global model was discretized using tetrahedral elements C3D10M in the software Abaqus. The thin layers of meninges and brain cortex had to be carefully meshed to avoid distorted elements and singularities due to thin, often curved shell geometries. Thus, at these regions, a finer mesh than that inside the brain instance had to be used.

In the software, global element properties of a maximum size of 0.01 (10 mm), a curvature of 0.1, and a minimum size of 0.001 (as a fraction of the maximum) were applied.



Local seeds were applied at the skull-dura mater surface with the parameters 0.005, 0.1, 0.0002, for maximal size, curvature, and minimum size, respectively, for a proper discretization of thin shell geometries and small curvature radii. Similarly, at the SAS-Brain interface, the numbers 0.01, 0.1, 0.0001, respectively for the above parameters, were applied to allow the brain bulk geometry to have larger elements inside, meanwhile enabling much finer element sizes on the boundary, connecting to the finer mesh of the SAS and dura mater. At the site of impact, the global size of 0.01 was changed to 0.002, to yield a better resolution of the impact pressure load, resulting in lower forces spread to numerous nodes (Figure 44). A total number of 77 000 elements had been created by applying the above meshing parameters.

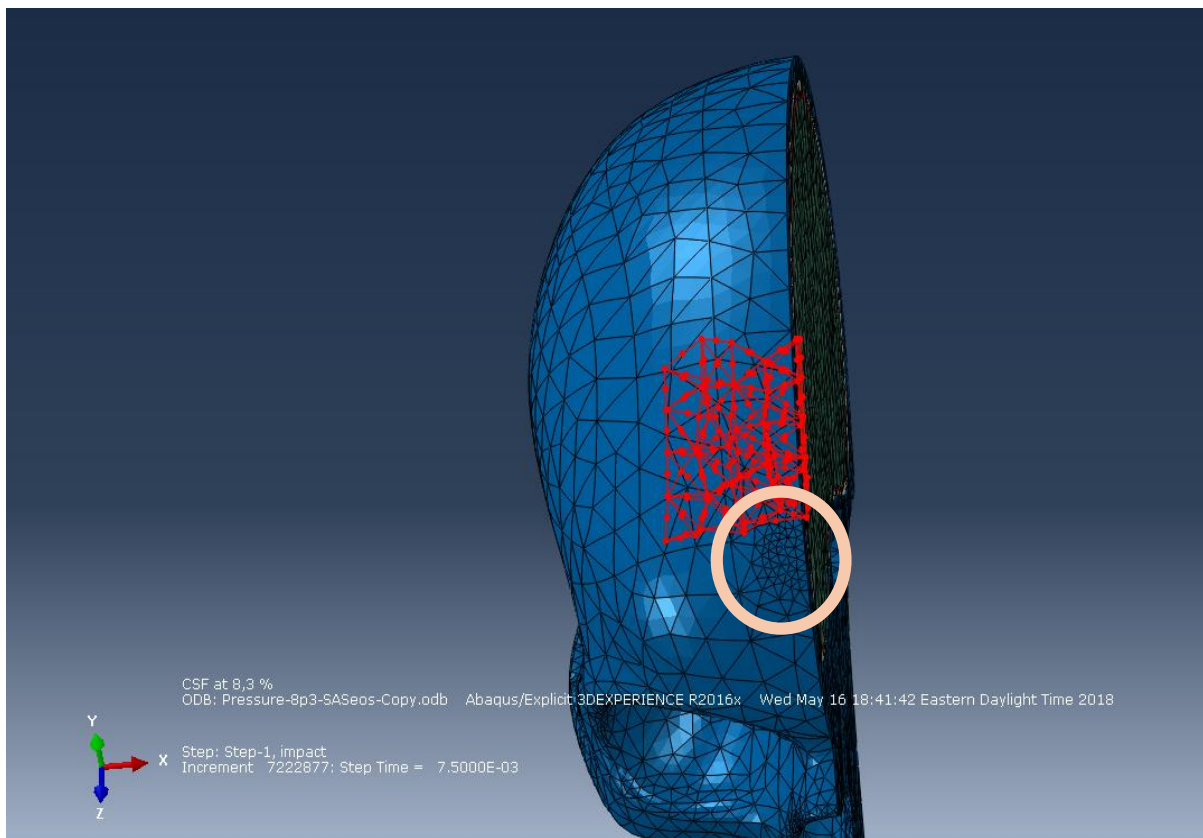


*Figure 44: Frontal view of the FE-model, with impact site marked by a circle, and element extraction site highlighted in red*

Explicit finite element method was applied to solve this problem. The boundary condition of the head model was assumed to be free between the head and the neck. To reduce the computational effort of the solution, only half of the model, using symmetry boundary condition at the half plane (restricted X translation, Y, Z rotation), was used.

The load was applied in the direction of the mass centroid, to eliminate any rotational effects. The simulated impact on the forehead, on a circular area of 8 mm radius (cut by the half plane of the head), was a pressure pulse, with 4.6 ms duration and a peak of 31 MPa (Figure 43 and Figure 44). This represents a case where the entire head is impacted by a force impulse having a peak of 6.5 kN, entirely resembling Nahum's case in [51].

#### 4.7.1.2. Applied material models

The material models of the dura mater and skull are completely sourced from the study of Asgharpour et al. [109]. The CSF filled SAS was modeled as a slightly viscous fluid. Studies show that fluid-like representation of CSF brings the most realistic results resembling Hardy's impact experiments [79], [90], [93], [110], [111], [112]. Additionally, a slight dynamic viscosity was applied [113]:

$$\eta = 0.00072 \text{ Pa} \cdot \text{s}$$

The fluidity was modeled for the dynamic case by the equation of state theory of Grüneisen, with the following Us-Up parameters [114]:

$$c_0 = 1650 \frac{\text{m}}{\text{s}}, \quad s = 1.92, \quad \Gamma = 0.35$$

For the brain density, the value  $1040 \frac{\text{kg}}{\text{m}^3}$  was applied [2], [27], [54], [94], [111], [114]. Hyperelastic material behavior was modeled with the parameters introduced in 3.6.2. Viscoelastic material properties of the brain were modeled with a general 6-term Prony-series developed for brain tissue, derived by Kleiven et al. in [4].

#### 4.7.1.3. Results from the global model

From the results of the global simulation, a cortical region of the brain part close to the surface was defined, resembling *area 9* of the frontal cortex, for which material parameters from our specimen were yielded (Figure 44 and Figure 45). A group of elements on the surface of the brain was extracted, as a shell with one element thickness (approximately 9 mm), having a rectangular shape with the size of 25 mm from medial to lateral side, and 35 mm in anterior-posterior direction (Figure 46).

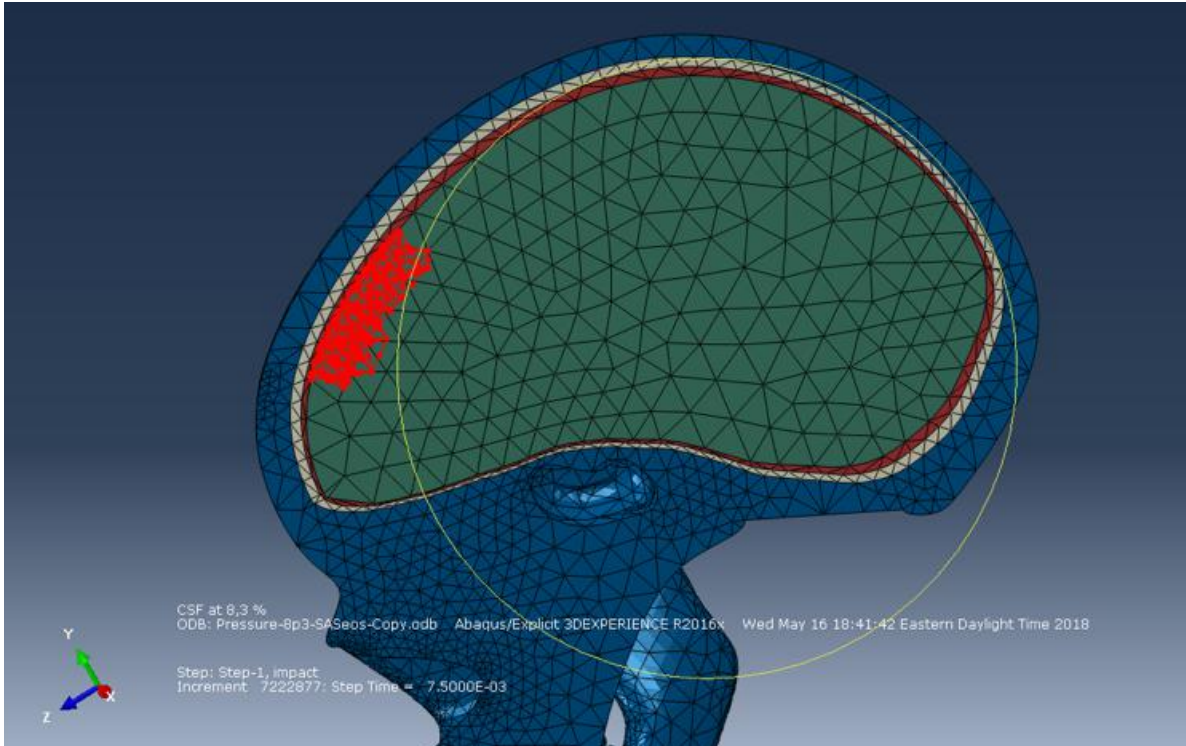


Figure 45: Medial view of FE-model of half head simulated as a global model, with highlighted area of extracted cortical elements

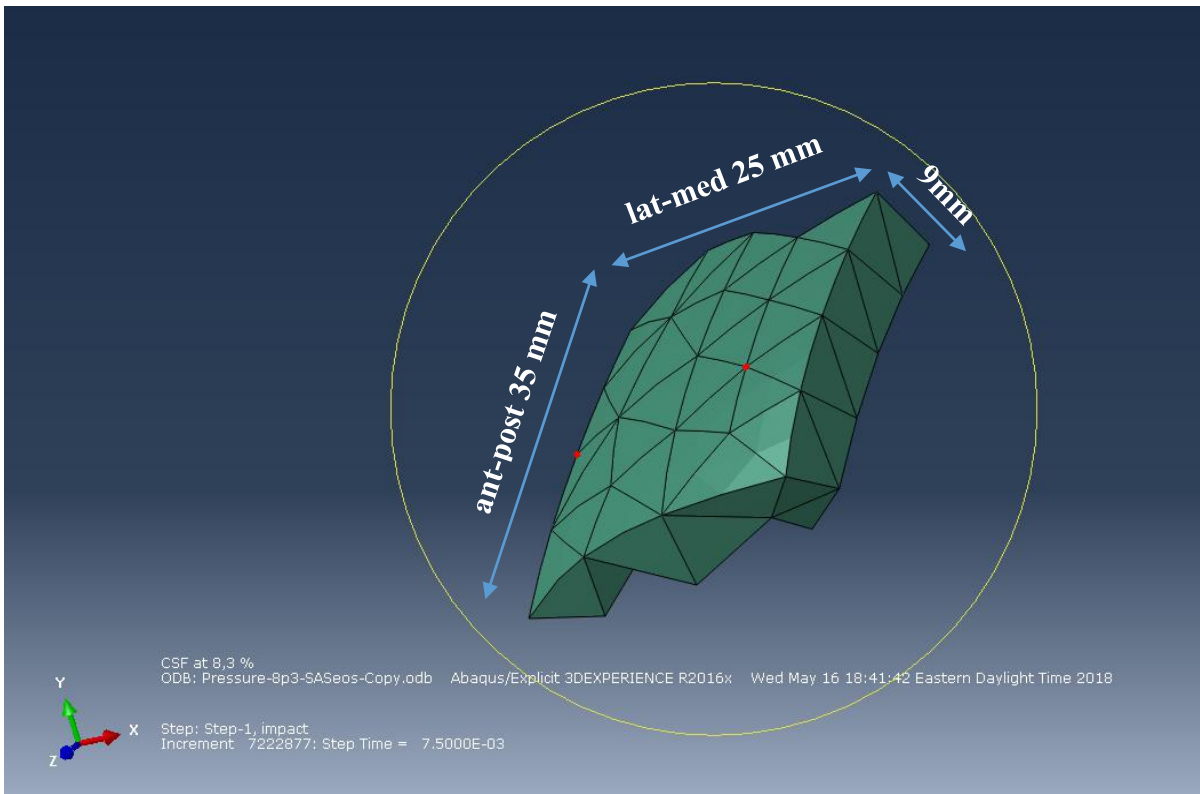


Figure 46: Extracted group of elements from the brain part of the mesh resembling the cortical region of area 9

For this section, the stress state on the boundaries was extracted, for all 4 sides, and the top surface. For this purpose, the time-dependent behavior of the von Mises stress from all elements comprising a side-surface was averaged, yielding a stress amplitude curve for each of the 4 sides and the top surface. The von Mises stress represents all principal and shear components of a stress state in one scalar value, that is why this was chosen to be used for a simple application. The directions of vectors of particular stress components would have been unknown and incorrect to apply to the local model, that is why that option had been canceled.

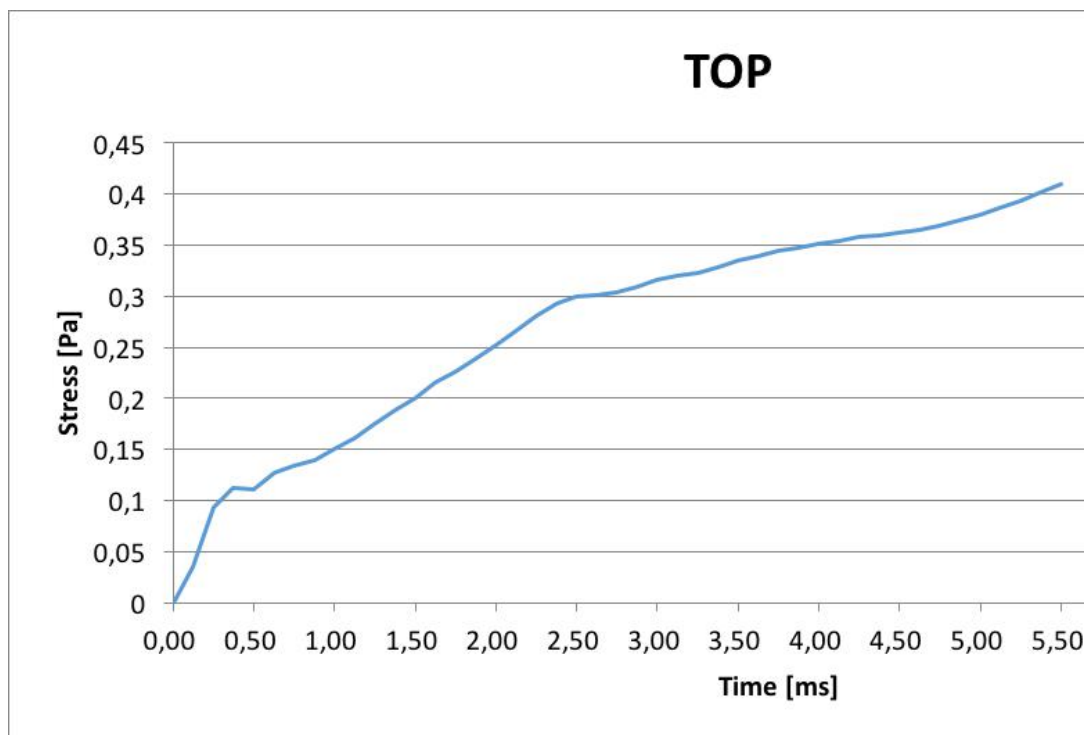


Figure 47: Curve of the von Mises stress state of the top surface extracted from the global model, applied as a load curve for the local model

#### 4.7.2. Local models

Two local models were constructed in Abaqus, resembling the overall size of the extracted segment from the global model.

First, the “study model” was constructed with a grey matter layer having six layers of following sizes, resembling the microscopic observations in the current study, being similar to [67]:

- I: 210  $\mu m$*
- II: 180  $\mu m$*
- III: 780  $\mu m$*
- IV: 210  $\mu m$*
- V: 450  $\mu m$*
- VI: 870  $\mu m$*

The rest of the thickness (6.3 mm) until the bottom surface was applied to have white matter.

Second, the “control model” was built with an unlayered grey matter, having the overall GM thickness of 2.7 mm (by summing the layers), and a rest of 6.3 mm thick white matter.

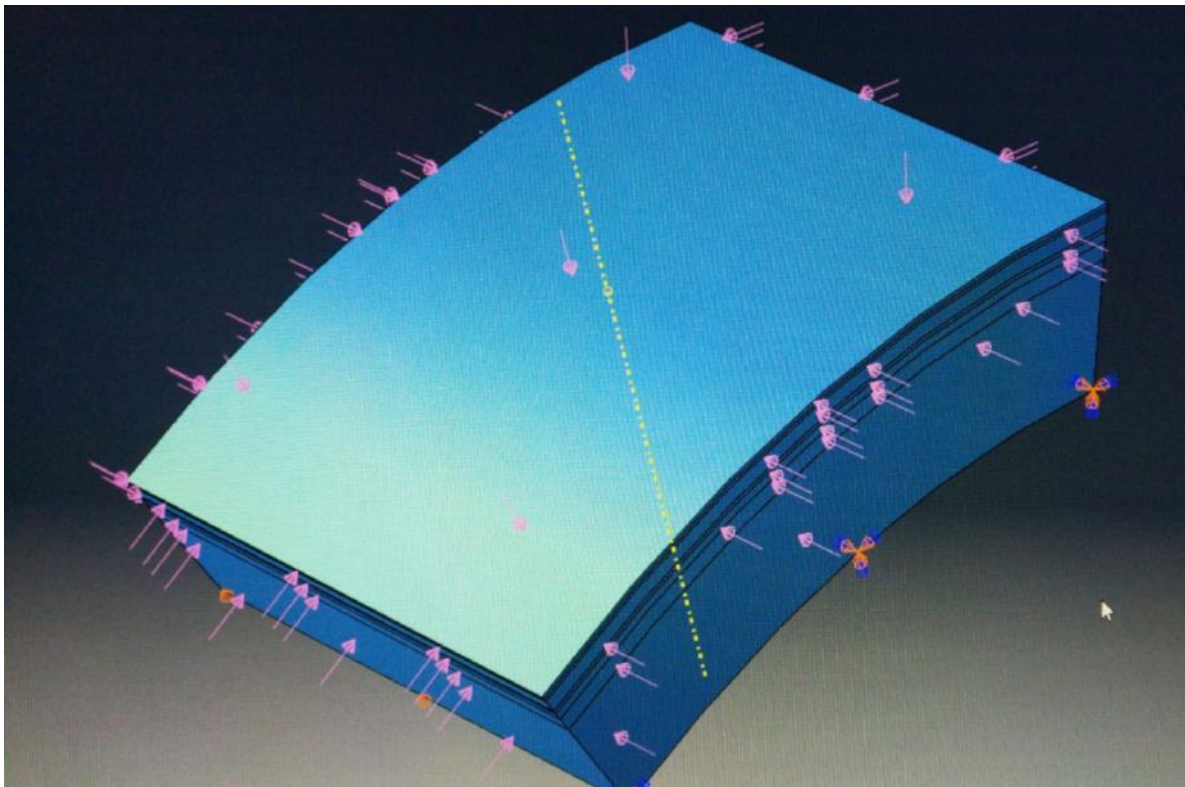


*Figure 48: Local model of the "study model", having the 6 layers of the grey matter, with load and boundary conditions applied.*

#### **4.7.2.1. Meshing**

Both models were meshed with explicit linear hexahedron elements, with the parameters 0.0005, 0.1 and 0.001, for maximum size, curvature, and minimum size, respectively. The layers of the different grey matter laminae were discretized effectively by pure hexahedrons.

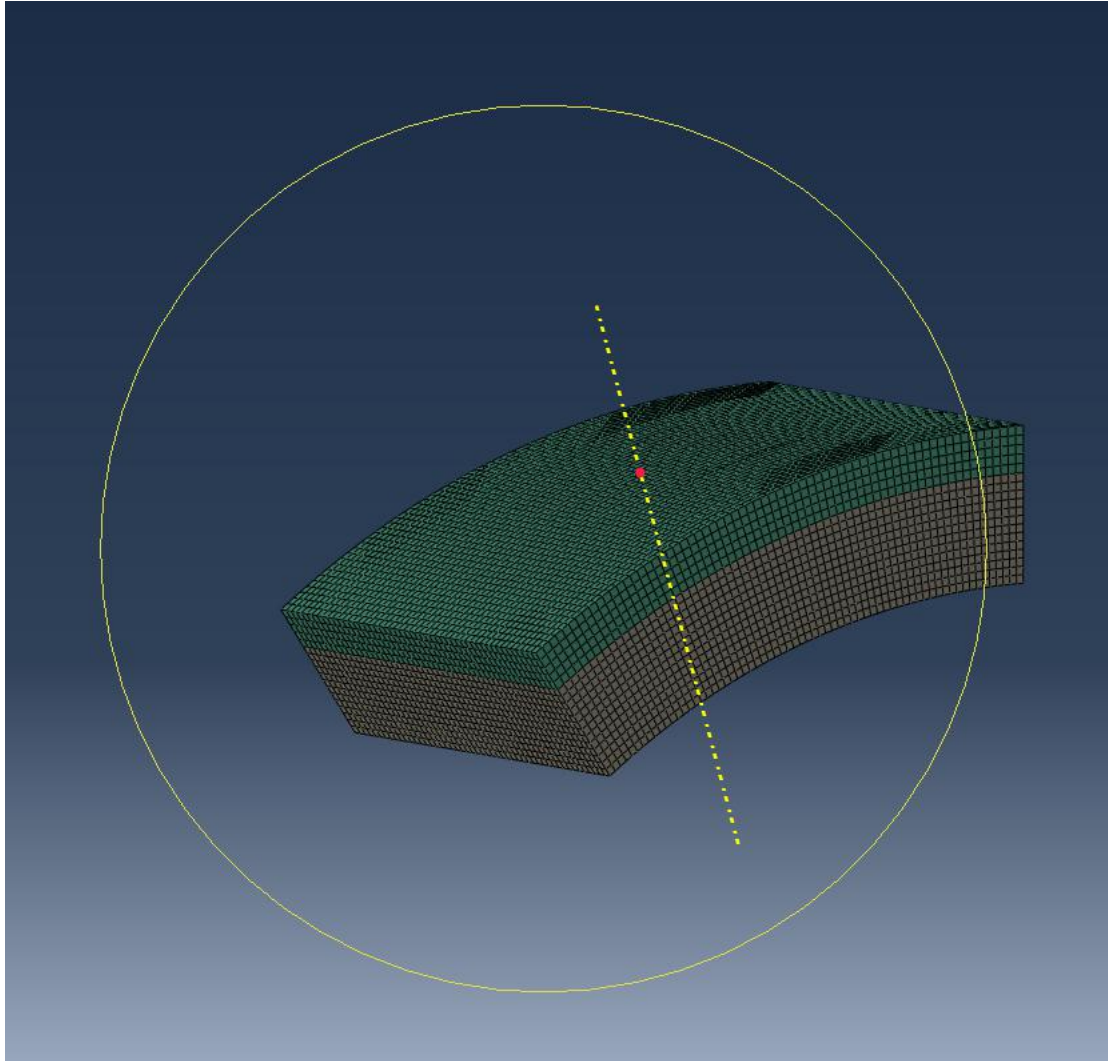


*Figure 49: Meshed local model of the "control model" of the cortex, having an unlayered grey matter, discretized by hexahedrons having the same size*

#### **4.7.2.2. Material models**

The material model of both local models included the density of  $1040 \text{ kg/m}^3$ , and a hyperelastic representation after Ogden (Chapter 3.6.2), applied for all layers of the models including white matter. The difference between the sample and control models was provided by the viscoelastic material properties of the particular layers. For the “study model”, parameters of the viscoelastic Prony-series function were provided for each of the 6 layers, based on the results of the experiments presented in Chapter 5.3.

For the “control model”, the averages of all layer means from Chapter 5.3 were applied as parameters of the two-term Prony-series.

The parameters of the viscoelastic model of the white matter for both local models were chosen to be sourced from the study of Finan et al. [32], for the parameter values in the given study are computed for a two-term Prony-series, based on measurements on a human cadaver, contributing to the feasibility and consistency of modeling in this study. The same hyperelastic model was chosen to be applied to all materials of the models, for the hyperelastic parameters provided by Kleiven et al. [4] provide an average representation, yielded by measurements on grey and white matter samples. Finan et al. [32] yielded the following mean values for a viscoelastic function of the white matter (representation in form of equation (15)):

$$G_{\infty} = 160.5 \text{ Pa}$$

$$G_1 = 363.8 \text{ Pa}$$

$$G_2 = 957.9 \text{ Pa}$$

$$\tau_1 = 1.17 \text{ s}$$

$$\tau_2 = 0.02 \text{ s}$$

After conversion to the normalized form of the Prony-series (formula 18), the following Prony-pairs were yielded and applied for the white matter in the local models:

$$g_1 = 0.245$$

$$g_2 = 0.646$$

$$\tau_1 = 1.17 \text{ s}$$

$$\tau_2 = 0.02 \text{ s}$$

#### **4.7.2.3. Load and boundary conditions**

The extracted stress curves from the global model for each appropriate side of the segment were applied as pressure loads, for both sample and control models in the same manner. Von Mises stress resembling a pressure was found to be justified in studies by Taylor et al. [115], [116]. The bottom surface of the local models was restricted by specially constructed boundary conditions, simulating its connection to the mass of the rest of the brain white matter. Translation in the radial direction was restricted for the entire surface, to resemble the connection to the mass. Two neighboring edges of the surface were embedded entirely by restricting all degrees of freedom, representing an origin, which is connected to the white matter mass, leaving the other edges and all other surfaces free for deformation.

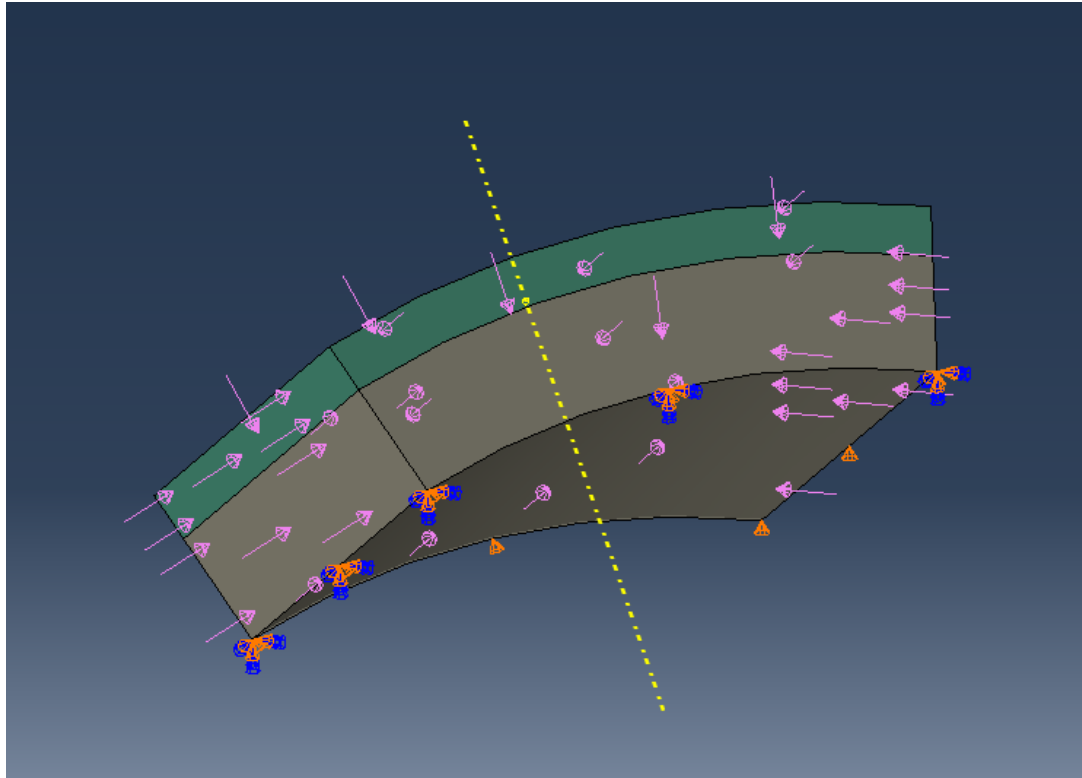


Figure 50: Load and boundary conditions applied on the "control model"

An explicit simulation, with a duration of 5 ms (impact 4.6 ms) was run for both models. For an analysis, first the strains (maximum principal logarithmic strain) of the entire GM of "control model" and "study model" were compared as an overall average. Second, the results of the "study model" were analyzed by comparing the mean strains and CSDM levels of the six layers.

## 5. Results

### 5.1. Microscopic images

From the obtained microscopic images of the prepared sample slices, the three most descriptive have been chosen for post-processing in the software. Cell nuclei were enhanced, and the surrounding myelin network and extracellular matrix were slightly faded. An overall visual assessment of all three images shows that the layers of the grey matter are distinguishable based on cellular density and tissue constitution. The images show a cross-section of the obtained specimen, from the superior frontal gyrus at the area of the superior frontal cortex in the dorsolateral region. The cross-section overlaps the neocortex, starting from the pia mater, across the layers of the grey matter, ending at the boundary of the white matter.



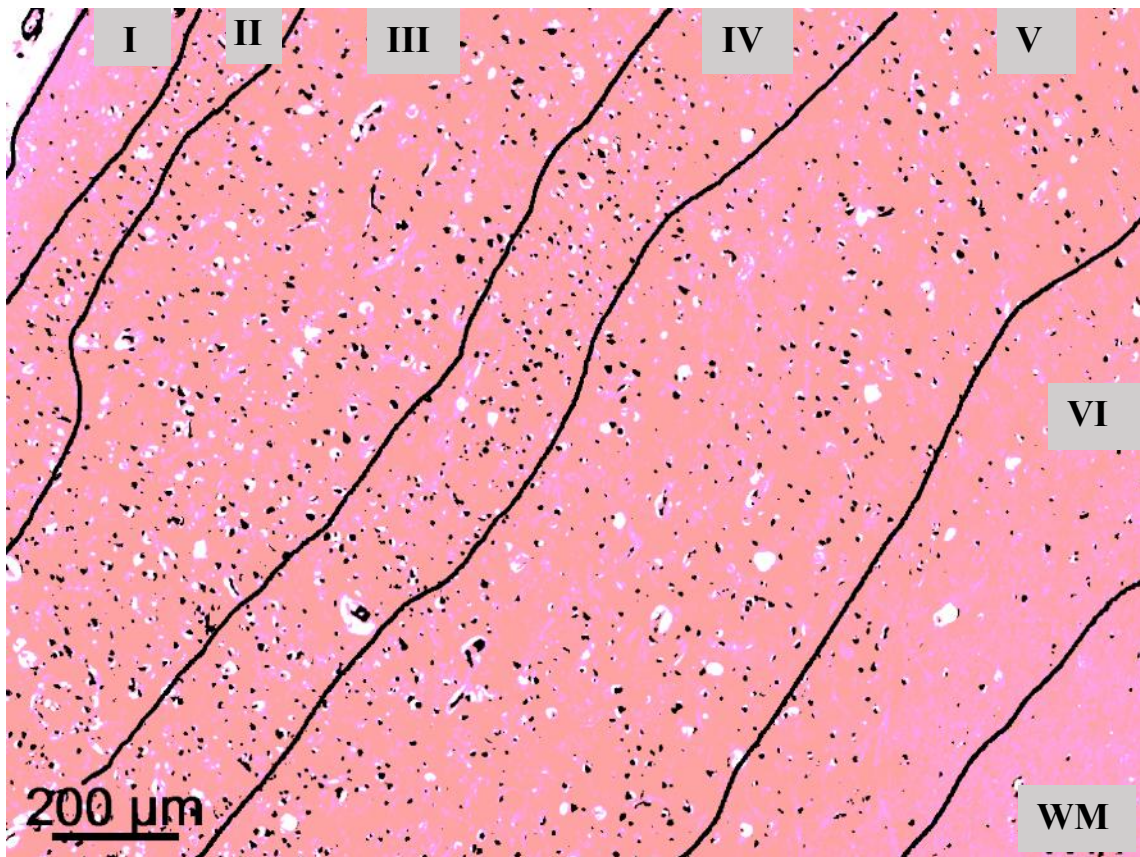


Figure 51: One of the obtained and post-processed microscopic images of a cross-section of the neocortical specimen. Observed layers separated by black lines, numbered with Roman numerals.

The H&E-staining provided clearly distinct cell nuclei in dark violet, and the structural features of the tissue, resulting from the dendritic and axonal processions of the cells and extracellular matrix, in light pink color. The cytoarchitecture across the layers is visible on (Figure 51).

Starting from the pia mater which depicts the borderline of the grey matter, moving perpendicular to the borderline, towards the inside region (WM) of the specimen, the first zone demonstrated a remarkable scarcity of cells. The width of the layer appeared to be around  $200\ \mu\text{m}$ . This region was observed as Layer I (Figure 51). Then, a clearly defined lining of a denser cellular accumulation was visible, marking the start of layer II. These cells demonstrated mostly circular shape (granular cells), and they were smaller than the conglomerate of the prominent cells in the next layer. Thus, layer II clearly represented a thin band of granular layer, spanning only about  $150 - 200\ \mu\text{m}$ . Next, the remarkable accumulation of larger, triangular shaped cells followed, moving further towards the white matter. These were identified as the pyramidal cells of layer III. This layer appeared to be distinct with its width as well: the mass of pyramidal cells reached a span of  $750 - 800\ \mu\text{m}$ . Afterward, the prevalence of triangular

cells reduced considerably for the thin band of the next layer, layer IV, which again only demonstrated granular cells, just as layer II. It spanned over a thickness of 200  $\mu m$ . Then, the pyramidal cells prevailed again, moving forward. These pyramidal cells were larger than in Layer III, but not so densely populated. This region was identified as layer V, having the width of 450  $\mu m$ . The next layer was hard to distinguish, but if examined closely, moving further towards the WM from layer V, the scarcity of the pyramidal cells could be observed, while larger cells having various shapes populated the zone. This was observed as the mixed layer VI, spanning 850  $\mu m$  while slowly transforming into white matter tissue. The end of layer VI was signaled by an observable disappearance of the large pyramidal and other various cells of significant size. The white matter demonstrated a striped structure of neurons (myeloarchitecture) and only a sparse population of point-like small cell nuclei (Figure 51).

## 5.2. Elastic properties

Resulting mean values of Young-moduli in different layers are shown in Table 2 for all samples.

<i>E</i>	<b>S1</b>	<b>S2</b>	<b>S3</b>	<b>S4</b>	<b>S5</b>	<b>S6</b>
<b>Layer I</b>	3.90	5.04	2.92	1.05	1.19	1.82
<b>Layer II</b>	10.75	5.44	4.57	1.94	1.72	1.77
<b>Layer III</b>	24.53	6.98	4.28	1.86	2.15	2.14
<b>Layer IV</b>	6.77					
<b>Layer V</b>		3.09		3.60	1.45	1.69
<b>Layer VI</b>					1.67	
<b>Average I-III</b>	13.06	5.81	3.92	1.61	1.68	1.91

Table 2: Resulting layer means of all samples computed from the measurements (*E* in kPa)

For the first statistical assessment of the difference between layers within each sample (Chapter 4.4.4.2), regarding the mean value of E-Modulus (ANOVA), a significant difference was revealed within samples S4 ( $p < 0.01$ ) and S2 ( $p < 0.1$ ). Tukey-Kramer post-hoc tests revealed, that the particular difference of E-modulus means between layers in S4 occurred between  $V > III$  and  $V > I$  ( $p = 0.01$ ).

As this was assessed on a rather low amount of data (number of successful measurements in S4 were 4, 4, 5, 3 for layers I, II, III, and V, respectively - number of successful measurements in S2 were 3, 3, 2, 4, 7, 1, for layers I to VI), these results would not be considered be representative. However, this assessment supplied a good initial signal for the occurrence of differences.

As discussed in Chapter 4.4.4.2, sample S1 was canceled from further assessments due to inconsistent and infeasible data.

After proof (ANOVA) that the overall means of some samples lie close to each other while being significantly different from other samples, the data of 3 similar samples (S4, S5, S6), the means of which lied close to each other (Table 2), could be cumulated and analyzed as a larger data collective, to be able to yield more representative results. ANOVA for the cumulated data for S4-6 was executed, comparing the means of the layers. Tests yielded a difference on  $p=0.15$  level of significance. As a Tukey-Kramer test was not utilizable for post-hoc assessment over  $p=0.1$  level of significance, 2-sided paired t-tests were conducted for each possible combination of two layers (15 tests). Pre-set level of significance of  $p=0.01$  was applied after a Bonferroni correction. The t-tests signalized a significant difference between the E-moduli means of layer I (1.38 kPa) and layer III (2.04 kPa).

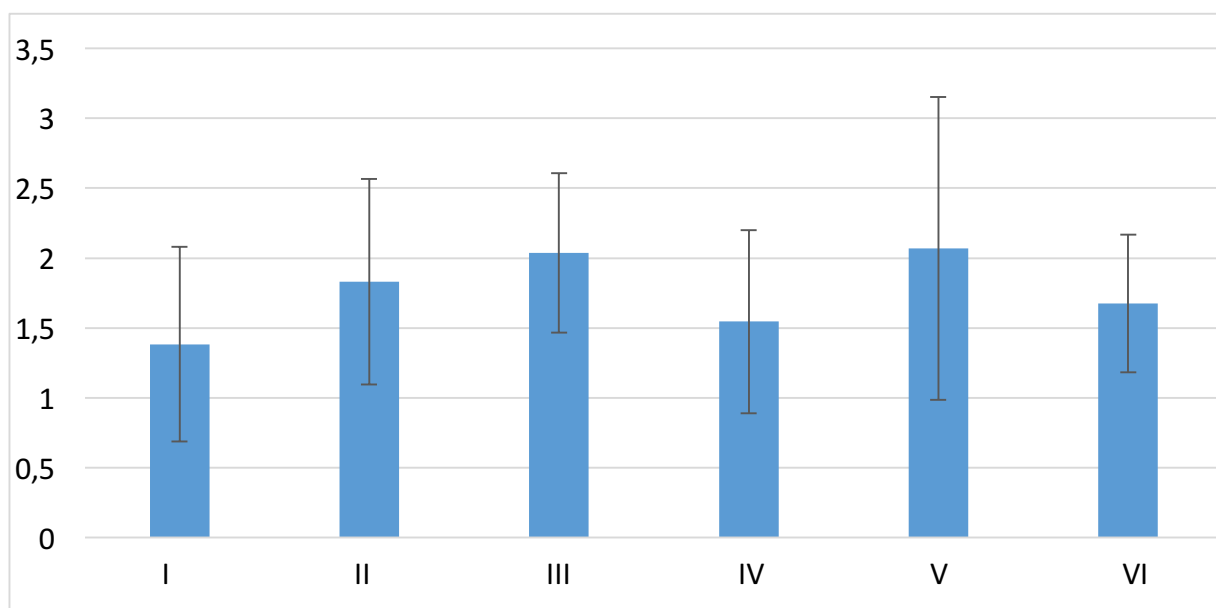


Figure 52: Layer means of E [kPa] for the cumulated data.

In this study, the emphasis is laid on the variation of the means between layers. In an effort to be able to yield feasible results from even more data as before, it was attempted to cumulate all samples S2 to S6, despite their averages being different. The absolute values of the averages of all samples S2-S6 were eliminated by a systematic normalization, so that a cumulated group even larger could be built, which represented only the variation of the layer means relative to each other without any influence of the absolute means due to difference of measurement parameters.

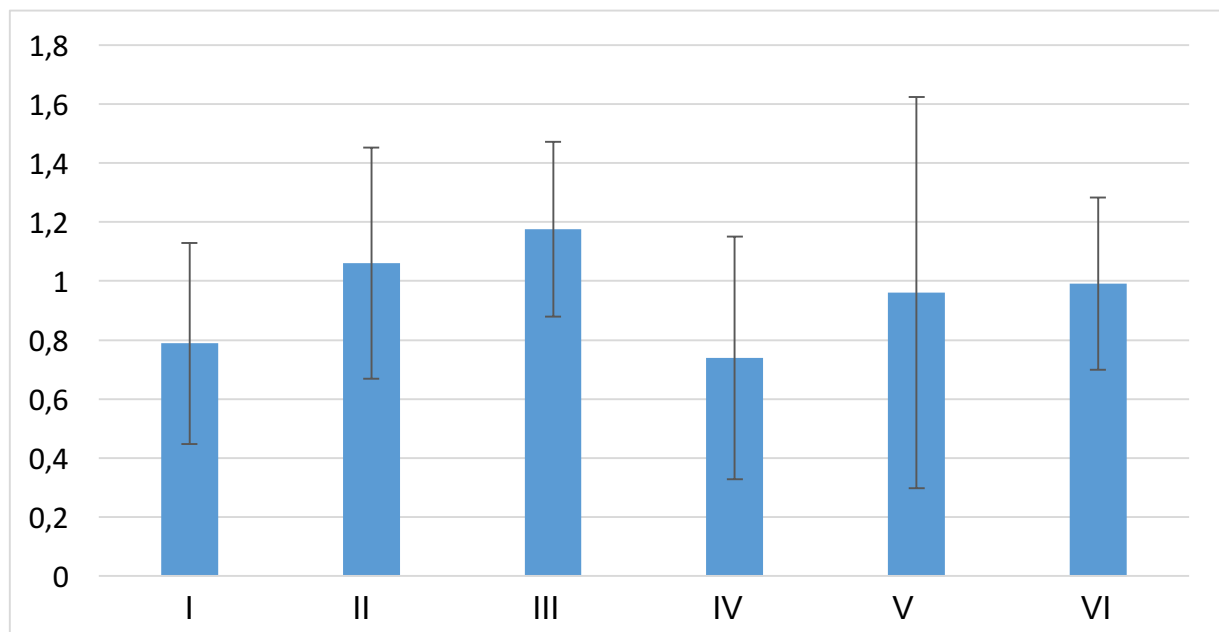


Figure 53: Variation of the layer means in the large dimensionless cumulated group of data

This process yielded a similar variation of the layer means, as seen in the smaller cumulated group (compare Figure 52 & Figure 53). One-way ANOVA for comparison of the yielded means signalized that the normalized values of the cumulated sample are different with  $p < 0.1$ . Tukey-Kramer post-hoc tests revealed that the difference is significant between layers I and III, which strengthened former results.

However, unlike the result of the previous statistics, no significance of the difference between layer V and the other layers can be shown. From the values, a stepwise increase of  $E$  from layer IV to VI was observed, unlike the result from the smaller cumulated data.

### 5.3. Viscoelastic properties

After conducting measurements, fitting, and calculating Prony-pairs for the dimensionless shear function of the viscoelastic model, the parameters in Table 3 were yielded for each of the six layers.

Parameter	$g_1$	$g_2$	$\tau_1$	$\tau_2$
Layer I	0.1779	0.1992	0.0913	3.4899
Layer II	0.1539	0.1808	0.0725	1.9213
Layer III	0.2349	0.1860	0.0537	2.4354
Layer IV	0.2592	0.2113	0.0679	1.5187
Layer V	0.2284	0.1690	0.0365	0.8851
Layer VI	0.1730	0.2403	0.0855	2.2547
Average	0.2003	0.1983	0.0688	2.1701

Table 3: Mean values of Prony-parameters of the grey matter layers, resulting from relaxation measurements

There is no significant difference, based on the conducted ANOVA tests, between any of the layers regarding time constants. A significant difference was detected only for parameter  $g_1$  ( $p=0.049$ ). Analyzing the difference with post-hoc tests could not detect the particular differing layers, being that the significance of the difference was not strong enough.

However, the differences between values of parameters do not necessarily relate to the actual difference in the time-dependent behavior, as it comprises of the overall effect of all four parameters. Thus, the dimensionless relaxation plots for each layer were created and compared by visual analysis, over one decade (10 s) time span (Figure 54 & Figure 55, layers numbered by Roman numerals). On the plots, it was observable that layers I and II not only demonstrated the same instantaneous response, but a very similar decay at the first part of the plot. Layers III, V, and VI converge together approximately to the same value (which represents the ratio  $G_\infty/G_0$ ). Apart from that, layer V was remarkable to have the fastest viscoelastic response of all.

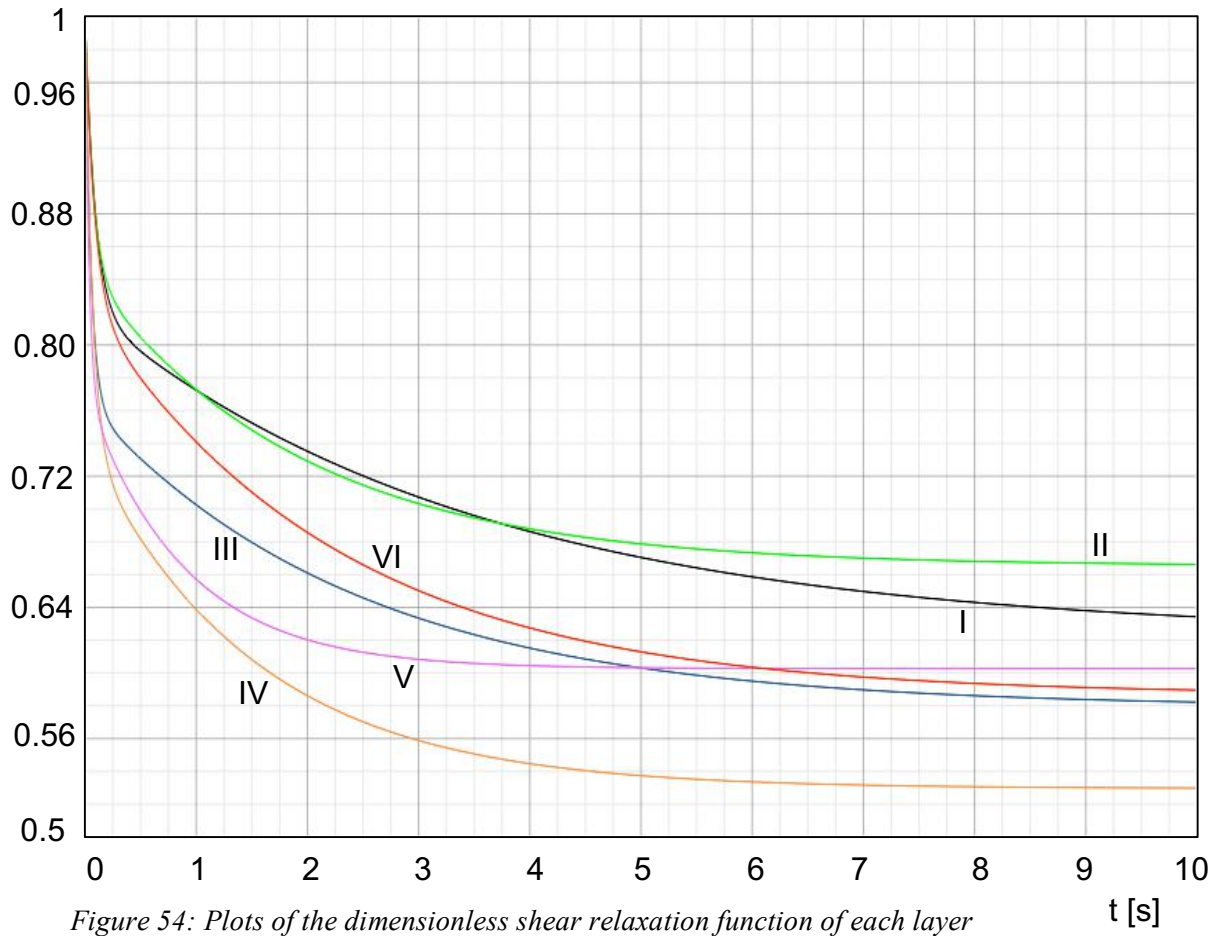


Figure 54: Plots of the dimensionless shear relaxation function of each layer

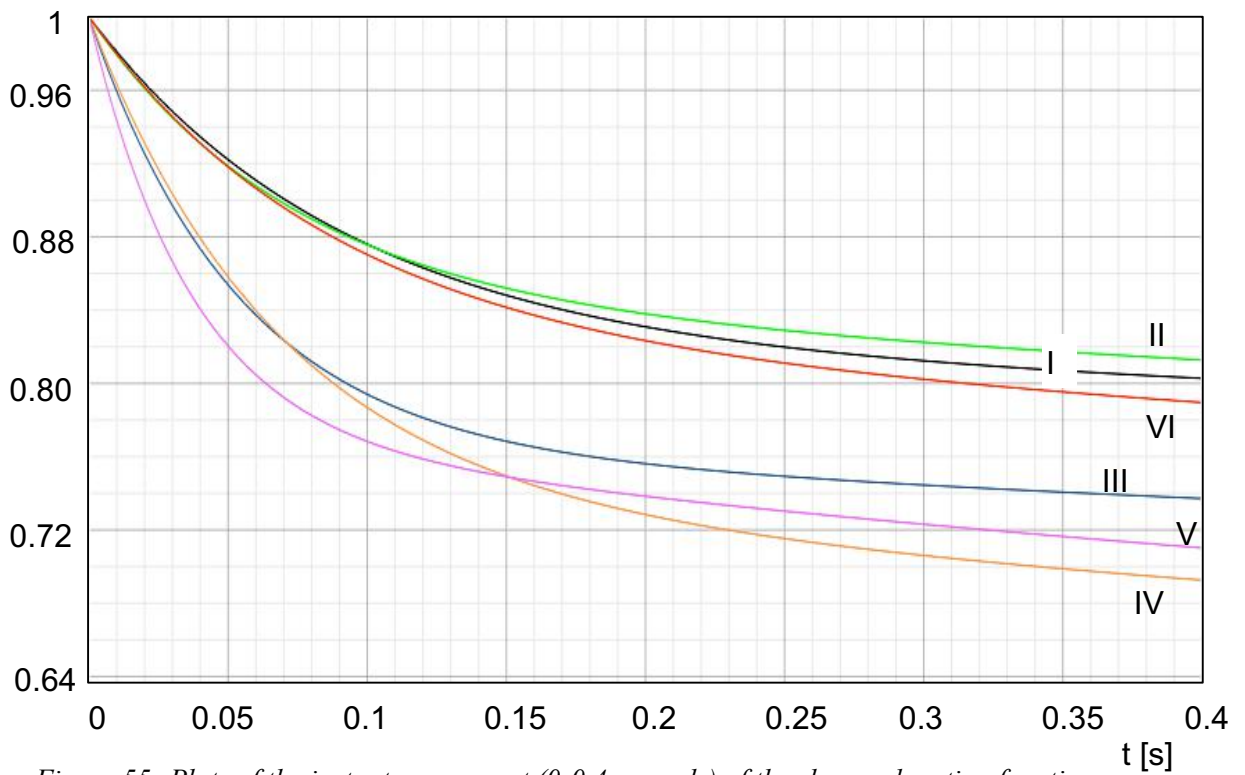


Figure 55: Plots of the instantaneous part (0-0.4 seconds) of the shear relaxation functions

## 5.4. FEM simulations

Two local models with different constitutions were simulated for the same stress state curve applied at their boundary. For an output, the maximum principal logarithmic strain component (LEPmax) was extracted for the elements comprising the entire grey matter.

In the case of the unlayered “control model” with a grey matter layer being homogeneous and having the average viscoelastic properties, the simulation, lasting until 5.5 milliseconds, yielded a peak average LEPmax of 0.02 (Figure 56). Absolute values of individual elements were not assessed for the set up might have caused artifacts due to excess strain at the boundaries of the model. In Figure 56 it is visible that the strain followed an exponential behavior, demonstrating the highest increase after the load pulse (4.6 ms) had already ended.

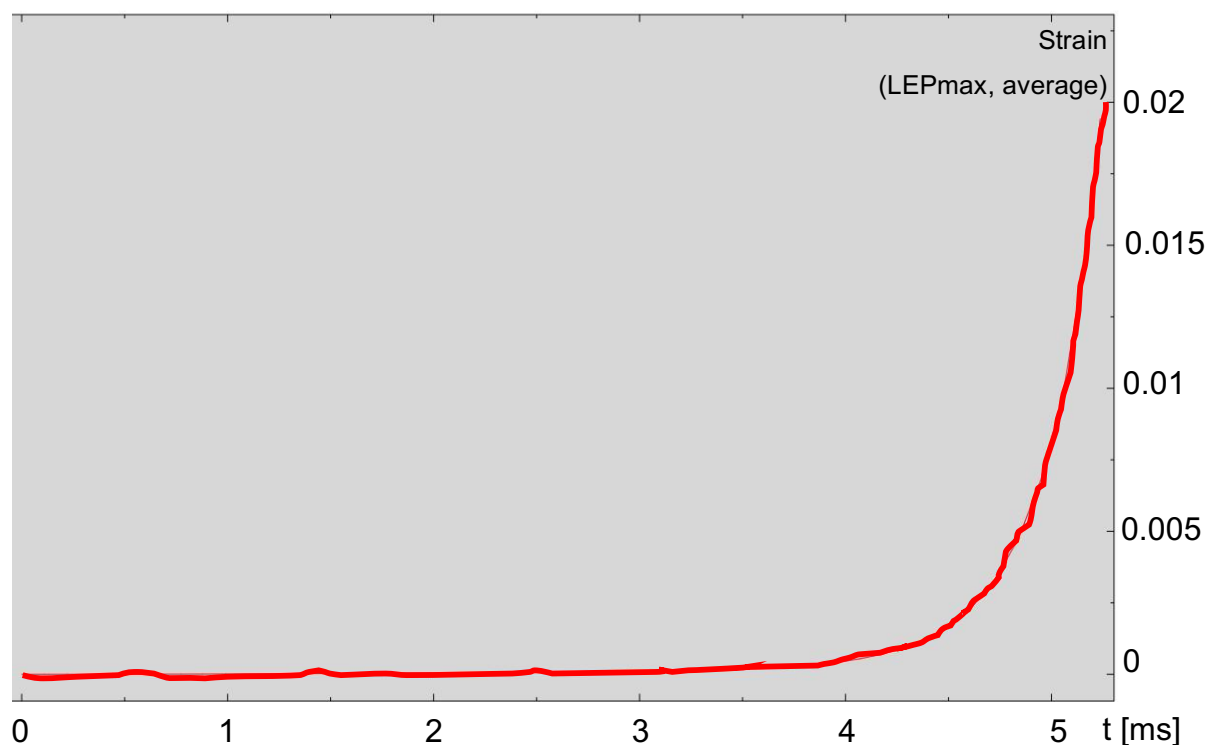


Figure 56: Overall strain over time averaged over the entire grey matter layer (created in Abaqus)

In contrast, the simulation of the layered “study model” (lasting 5 ms) resulted in a remarkably higher average LEPmax of 0.057, (0.012 in “control model” at 5 ms). More importantly, significant differences were revealed regarding the excess of strain between different layers (Table 4). While strains in layer I would even reach 0.2, and the average of layer II is as high as 0.131 as well, the other layers demonstrate decent strain levels well under 0.01.

Layer	I	II	III	IV	V	VI
<b>Average strain</b>	0.190	0.131	0.010	0.005	0.004	0.005
<b>Highest strain</b>	0.217	0.165	0.070	0.070	0.072	0.076
<b>Strains over 0.15</b>	yes	yes	no	no	no	no

Table 4: Strain level ( $LEP_{max}$ ) results for the layers of the "study model"

## 6. Discussion

A specimen of the dorsolateral superior frontal cortex was extracted from a cadaveric brain. After examining its cellular structure and tissue architecture visually, the six distinct layers of the neocortex could be identified, resembling the approximate size and histological features of the layered structure discussed in prior studies [38]–[47]. The observations resemble the characteristics of the superior frontal cortex and Brodmann's *area 9* described by Petrides & Pandya [117]: layer IV is not well developed (that is, it is narrow and not very densely populated). Likewise, layer II is narrow but densely populated in a compact manner with granular cells. The upper part of layer III is observed to be relatively dense, whereas the lower part is not as cell dense and has a number of large, deeply stained pyramidal neurons.

The specimen was examined for its material properties with AFM nanoindentation, focusing on the differences in the outcomes of material properties between the identified layers. During experiments, the continuous hydration of the sample was very important. It is sufficient to provide hydration by water only, suggested as well in [17], with a bubble of water covering the specimen during measurements. The temperature of the specimen was kept as low as possible, having 18 °C in the lab room.

Regarding the indenter diameter, a compromise had to be made, due to histological heterogeneities on different length scales. In the human brain, there is heterogeneity due to different anatomical regions at the centimeter length scale. There is heterogeneity due to fiber reorientation at the millimeter length scale. There is heterogeneity due to the distinction between cell bodies and neurites, and because of distinct layers, on the 100  $\mu m$  length scale, and due to the distinction between nuclei and cytoplasm at the 10  $\mu m$  length scale. In this experiment, the 38  $\mu m$  indenter diameter was selected to be small enough on the length scale



of transitions between the layers, to be able to measure in distinct regions. However, this size falls into the length scale of cell nuclei, being prone to cause some inconsistent measurements. That is, inside a layer, the mechanical response depends on the detailed constitution of the region where the measurement was made, if it hit a cell body, it might have been a stiffer result, than on the cytoplasm or a network of dendrites. These unfeasible data were eliminated in the statistical processes as outliers so that the final data become consistent, and significant differences in the mechanical properties could be detected. Differences were apparent among layers, as well as additional statistical significance could be yielded for the difference between the elastic modulus of layer III and layer I. The overall average elastic modulus value of the cumulated group  $E = 1.78$  lies close to the average of  $1.389 \text{ kPa} \pm 0.289 \text{ kPa}$  found by Budday et al. [29], strengthening the feasibility of the measurements in this study.

The pattern of the variation of the E modulus (Figure 52) through the cortical thickness could be connected to variations in the cytoarchitecture. Generally, the higher stiffness of layer III than layer I (with statistical significance) can be connected to the presence of pyramidal neurons in layer III in a dense population, while they are completely absent in layer I, as well as very scarcely populated in layer II and IV (see Figure 9, Figure 51, compare [38]–[42]). Eickhoff et al. [118], as well as Schleicher & Zilles [43]–[46] provided important figures, grey-level index (GLI) profiles, for the density of cells across the cortical depth from the pia mater to the WM, as well as visualization of the myelin density.

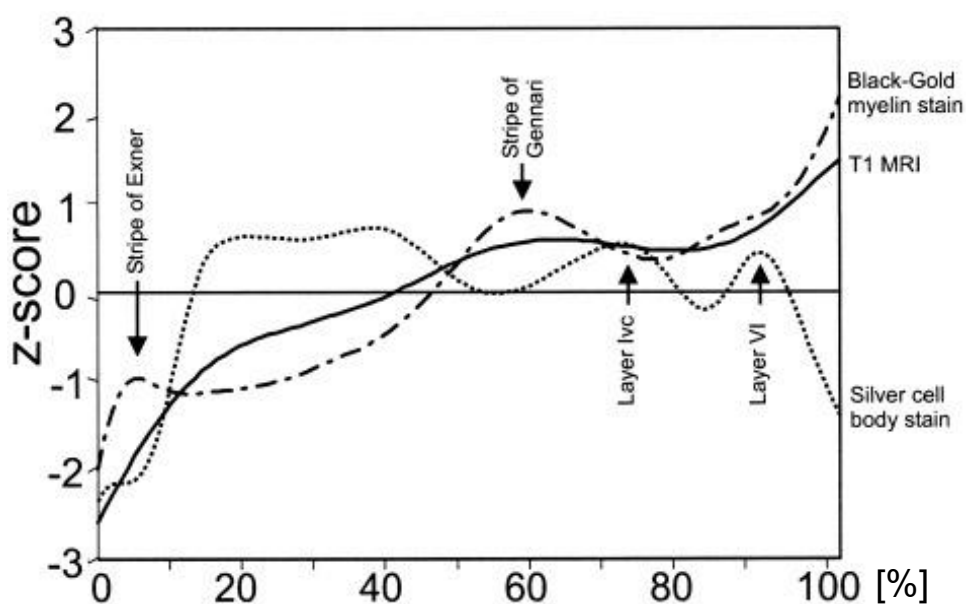


Figure 57: Visualisation of myelin density (dot-dashed line) and cell density (dotted line) starting from the pia mater (0%) to WM (100%) of the visual cortex in the occipital lobe [118]

The profile for the occipital cortex (with similar layered structure, compare [69] & [117]) provided by [118] (Figure 57) demonstrates similarity to the pattern of layer stiffness found in the current study (Figure 52). Pyramidal neurons may not only have an influence on the stiffness by the presence of their large cell nuclei but also by their high connectivity which implies a denser myelin network (Chapter 2.4.1.). Still, the pattern of the cell density resembles the pattern of the apparent stiffness across the layers in the first place. Based on this comparison, it can be suggested that the local stiffness properties of grey matter are influenced by the presence of pyramidal cells.

In the case of measuring the contact stiffness from the force-displacement plots provided by nanoindentation measurements (Chapters 4.4.2 & 4.4.3.3), the duration of the initial slopes of the unloading curve shall be short enough compared to the obtained relaxation times, suggested by Cheng et al. [8]. From the results from section 5.3, the higher average relaxation time of 2.17 s shall be considered. Approach velocities range from 50 *nm/s* to 4000 *nm/s* (Table 1), and the most occurring linear length of the slope is approximately 10 nm (Figure 38 and Figure 39). This implies that the duration value ranges from 0.2 s to 0.0025 s which is 0.08 – 0.001 times the higher relaxation time, corresponding to the suggested value by Cheng et al. [8], being the smallest in samples S4, S5, and S6 from which the most essential results have been obtained.

Regarding the viscoelastic relaxation experiments, among the extracted dimensionless Prony-parameters the pattern of the variation of  $g_1$  found to be significant, proven by the ANOVA test. However, this alone does not provide any clue for the overall viscoelastic relaxation behavior of the material. The viscoelastic functions were analyzed on the whole to obtain knowledge about differences. Meanwhile, it is to observe that the overall average of the parameters through the entire cortex yields almost the same value for  $g_1$  (0.2003) and  $g_2$  (0.1983).

The two relaxation times, (different in every layer with almost 2 orders of magnitude) could be associated with the viscous and the porous nature of brain tissue behavior, based on [32]. Apart from that, a greater measure of decay implies a looser histological structure. A fast relaxation with a little amount of decrease, such as in layer V, implies that the fibrous network remains relatively intact under load. This phenomenon can be associated with the high amount of proteoglycans and glia present in the matrix [48], which hold together the cellular network.

Proteoglycans are anions, which provide a negative ionic charge. Based on the study of Jamieson and Southwick [119], viscosity decreases with higher ionic strength. This explains the lower viscous behavior in layers III, V and eventually IV (Figure 54).

An additional explanation for the differences in time decay can be provided based on the findings of Chimich et al. [120], who showed that ligaments with higher water content demonstrated greater relaxation than ligaments with lower water content. Regarding the similarity of the tissue architecture of fibrous ligaments and a dense network of neuronal fibers, it can be assumed that a denser dendritic network holds water better, as it was found by Budday et al. [25] as well. Enhanced time-dependent behavior correlated with stress-induced moisture/water transfer is also suggested by [121]. Concerning our current findings, layers I and II have low water content, layers III, IV, V, and VI high water content, where layer V can hold it the most because of its dense myelin network, implying a fast response (Figure 54).

The pattern of the first relaxation time  $\tau_1$  in Table 3 clearly follows the characteristics of the cytoarchitecture, especially regarding pyramidal cells (Figure 9, Figure 51), having the smallest values (fastest decay) in layers III and V, and higher values with scarcely populated layers. The pattern of the second relaxation time  $\tau_2$  in Table 3 can be correlated with the myelin architecture (Figure 9), with having the lowest values (stiffer, fast response) in layers where strong myelin bands are present.

The *in silico* simulations of the local models employed simplified, concentrated average stress states on the sides of a rectangular group of extracted elements approximating cortical *area 9*. The stress curves, which result from a standard impact simulation of the head, were utilized as a load, and follow a continuous increase after a fast raise during the first millisecond. Remarkable is the induced strain, which was assessed by averaging LEPmax over all elements comprising a particular layer or the whole GM, and follows a clear exponential behavior, having the most significant increase after the original impact pulse after 4.6 ms has already finished.

## 6.1. Limitations of this study

The specimen for this study had been obtained from the region of the cadaveric brain depicted as *area 9* after Brodmann. All samples were obtained and all measurements were conducted on that specific cross-section of the neocortex. The yielded results correlate apparent

cytoarchitecture and mechanical properties, but the obtained values for the variation of the mechanical parameters are only valid for this specific area of the brain. As it has been already discussed (Chapter 2.3), different areas of the brain demonstrate differences in the tissue architecture and layer thicknesses of the neocortex. In this study, only one area was examined. Still, the correlation between the cytoarchitecture and mechanical properties are visible, and our results could provide an important basis for applying variations to the mechanical properties in various areas knowing their cytoarchitecture.

The findings in this study are not confined to the particular age of the brain cadaver (67 years old male), as there is no correlation between age and mechanical properties [32]. This implies, that the results of this study can be generalized for the human brain at all ages.

The tissue was tested *ex vivo*, which neglects important phenomena that could be captured when testing *in situ*, such as the cerebral perfusion pressure which might have a neurophysiological influence on the mechanical properties. However, our experimental design choice provided important advantages offering access to deeper cortical structures thus enabling examination of the detailed constitution of the laminae which are enclosed *in situ*. Although cerebral perfusion could have some influence, most deformation in brain tissue is deviatoric, not volumetric, the shear modulus being much lower than the bulk modulus. Therefore, any effect of hydrostatic pressure on the deformation field is likely to be modest.

The measurements for elastic modulus were occasionally affected by adhesion and surface tension effects, whereas most disturbances could be eliminated by conducting the measurements in an aqueous environment. The neutral deflection signal on the AFM caused inaccuracies regarding the idle value of the measured force, which was eliminated by zero-point corrections in both elastic and viscoelastic measurements.

Regarding FEM simulations, the extraction of the stress state from the borderline elements of the cortical part of the global model is a rough approximation, for those elements are large in relation to the size of the examined region, due to the element sizes being optimized for the global simulation. The approximation of the stress state in the value of the von Mises stress is another simplification. A complete stress state having six components were not possible to extract and apply due to the stress being a vector quantity and the exact vector directions could

not be extracted and applied in the local model in two different coordinate systems. Still, applying the von Mises stress at all boundaries of the model would not significantly impact outcomes regarding relative differences of layer strains. As the objective of this study is to determine the relative stress state among the different layers of the grey matter, the use of von would not change the ratio of stress among the layers.

## 7. Conclusion

A specimen of the dorsolateral superior frontal cortex was extracted from a cadaveric brain. After examining its cellular structure and tissue architecture visually, the six distinct layers of the neocortex could be identified, resembling the approximate size and histological features of the layered structure discussed in prior studies [38]–[47].

The specimen was examined for its material properties with AFM nanoindentation, focusing on the differences in the outcomes of material properties between the identified layers. Elastic properties (Young's Moduli  $E$ ) were obtained for each layer from several measurements and statistically analyzed for differences. Differences were apparent among layers, as well as additional statistical significance could be yielded for the difference between the elastic modulus of layer III and layer I. Likewise, dimensionless Prony-parameters were extracted with nanoindentation with a spherical tip, by conducting time-dependent relaxation experiments, again analyzed statistically by building layer means representing the corresponding dimensionless Prony-parameters for each layer. The newly obtained material properties were applied to a material model in a FEM simulation of a local model of the layered structure of the brain neocortex. The strain response of models with and without a layered grey matter was compared at the same stress state.

The pattern of the cell density resembles the pattern of the apparent stiffness across the layers. Based on this comparison, it can be suggested that the local stiffness properties of grey matter are influenced by the presence of pyramidal cells.

The viscoelastic properties of the layers differ in terms of the parameters of their viscoelastic function constructed as a Prony-series. Additionally, the behavior of the particular viscoelastic functions is different from each other in terms of apparent viscous or elastic dominance in

behavior, the speed of decay, and the ratio of the instantaneous modulus to the infinite shear modulus. This can also be related to the cyto- and myeloarchitecture of the particular layers.

Material properties of neocortical layers have not been experimentally examined before. Additionally, detailed mechanical FEM simulations of deeper neocortical architecture have not yet been concluded. Therefore, this research is an important contribution to the field of detailed head injury simulations providing a novelty in the analysis of grey matter layer material properties.

## **8. Extension in future studies**

Currently, important developments and studies are being established regarding the utilization of magnetic resonance elastography (MRE) to biological materials such as the brain, assessing its viscoelastic properties [34], [35], [122]. Mechanical properties of distinct areas of the brain cannot be captured by MRE measurements properly in such detail as by *ex vivo* measurements. However, further development of this technology could make it possible to capture viscoelastic properties of every region of the entire brain, distinguishing between several areas and layers of the grey matter, and build a general, highly detailed mechanical simulation.

As discussed in Chapter 6.1, the experiments were conducted merely on a sample of a specific brain area, the frontal cortex (*area 9*). Since there is a difference in the laminated structure among different brain areas, due to the neuronal constitution and density, the allocation of mechanical properties between layers is also different. More knowledge about the mechanical behavior of other parts of the brain can be obtained by studying the detailed mechanical properties of other areas, thus revealing and assessing the risk in specific regions exposed to injuries.

One of the most interesting novelties of materials engineering is the invention of functionally graded composites. These are implied as shells or beams, comprising of a bulk basic matrix substance, and a compositional gradient substance, changing progressively through a cross-section, from layer to layer. The volume fraction or density of the mixed compositional substance implies that the mechanical and material properties, such as thermal gradient or the elastic modulus of such materials follow a pattern which can be also defined with a function

[123], [124]. The pattern of the mechanical properties through the grey matter layers could be approximated with a function as well so that the grey matter neocortex is described as a shell of functionally graded material. Considering the distribution and the size of neural cells, the principal orientation of axons, the myelin density, functional gradients could be set up to describe the variation of a specific material property through the cortex thickness.

## Bibliography

- [1] K.-U. Schmitt, P. F. Niederer, and F. Walz, *Trauma Biomechanics : Introduction to Accidental Injury*. Springer Berlin Heidelberg, 2004.
- [2] T. W. McAllister *et al.*, “Maximum principal strain and strain rate associated with concussion diagnosis correlates with changes in corpus callosum white matter indices,” *Ann. Biomed. Eng.*, vol. 40, no. 1, pp. 127–140, 2012.
- [3] K. Baeck, J. Goffin, and J. Sloten Vander, “The use of different CSF representations in a numerical head model and their effect on the results of FE head impact analyses,” *8th Eur. LS-DYNA Users Conf.*, no. May, 2011.
- [4] S. Kleiven, “Predictors for traumatic brain injuries evaluated through accident reconstructions,” 2007.
- [5] F. A. O. Fernandes and R. J. A. De Sousa, “Head injury predictors in sports trauma - A state-of-the-art review,” *Proc. Inst. Mech. Eng. Part H J. Eng. Med.*, vol. 229, no. 8, pp. 592–608, 2015.
- [6] W. C. Oliver and G. M. Pharr, “Measurement of hardness and elastic modulus by instrumented indentation: Advances in understanding and refinements to methodology,” 2004.
- [7] G. M. Pharr and A. Bolshakov, “Understanding nanoindentation unloading curves,” 2002.
- [8] Y. T. Cheng and C. M. Cheng, “Relationships between initial unloading slope, contact depth, and mechanical properties for spherical indentation in linear viscoelastic solids,” *Mater. Sci. Eng. A*, vol. 409, no. 1–2, pp. 93–99, 2005.
- [9] D. M. Ebenstein and L. A. Pruitt, “Nanoindentation of soft hydrated materials for application to vascular tissues,” *J. Biomed. Mater. Res. - Part A*, vol. 69, no. 2, pp. 222–232, 2004.
- [10] D. M. Ebenstein, D. Coughlin, J. Chapman, C. Li, and L. A. Pruitt, “Nanomechanical properties of calcification, fibrous tissue, and hematoma from atherosclerotic plaques,” *J. Biomed. Mater. Res. - Part A*, vol. 91, no. 4, pp. 1028–1037, 2009.
- [11] L. Cheng, X. Xia, L. E. Scriven, and W. W. Gerberich, “Spherical-tip indentation of viscoelastic material,” *Mech. Mater.*, vol. 37, no. 1, pp. 213–226, 2005.
- [12] P. Chandrasekaran *et al.*, “Biomechanical properties of murine TMJ articular disc and condyle cartilage via AFM-nanoindentation,” *J. Biomech.*, vol. 60, pp. 134–141, 2017.



- [13] K. Sweers, K. van der Werf, M. Bennink, and V. Subramaniam, “Nanomechanical properties of  $\alpha$ -synuclein amyloid fibrils: A comparative study by nanoindentation, harmonic force microscopy, and Peakforce QNM,” *Nanoscale Res. Lett.*, vol. 6, no. 1, p. 270, 2011.
- [14] G. Thomas, N. A. Burnham, T. A. Camesano, and Q. Wen, “Measuring the Mechanical Properties of Living Cells Using Atomic Force Microscopy,” *J. Vis. Exp.*, no. 76, pp. 1–8, 2013.
- [15] J. C. Benech *et al.*, “Diabetes increases stiffness of live cardiomyocytes measured by atomic force microscopy nanoindentation,” *Am. J. Physiol. Physiol.*, vol. 307, no. 10, pp. C910–C919, 2014.
- [16] H. K. Heris, A. K. Miri, U. Tripathy, F. Barthelat, and L. Mongeau, “Indentation of poroviscoelastic vocal fold tissue using an atomic force microscope,” *J. Mech. Behav. Biomed. Mater.*, vol. 28, 2014.
- [17] E. G. Herbert, P. Sudharshan Phani, and K. E. Johanns, “Nanoindentation of viscoelastic solids: A critical assessment of experimental methods,” *Curr. Opin. Solid State Mater. Sci.*, vol. 19, no. 6, pp. 334–339, 2015.
- [18] J. E. Galford and J. H. McElhaney, “A viscoelastic study of scalp, brain, and dura,” *J. Biomech.*, vol. 3, no. 2, pp. 211–21, Mar. 1970.
- [19] J. S. Ruan, T. B. Khalil, and A. I. King, “Finite Element Modeling of Direct Head Impact,” 1993.
- [20] K. Miller and K. Chinzei, “Constitutive modelling of brain tissue: Experiment and theory,” *J. Biomech.*, vol. 30, no. 11–12, pp. 1115–1121, 1997.
- [21] R. W. Ogden, “Large Deformation Isotropic Elasticity - On the Correlation of Theory and Experiment for Incompressible Rubberlike Solids,” *Proc. R. Soc. A Math. Phys. Eng. Sci.*, vol. 326, no. 1567, pp. 565–584, Feb. 1972.
- [22] L. A. Mihai, L. K. Chin, P. A. Janmey, and A. Goriely, “A comparison of hyperelastic constitutive models applicable to brain and fat tissues,” *J. R. Soc. Interface*, vol. 12, no. 110, 2015.
- [23] K. Miller, “Finite Deformation, Linear And Non-Linear Viscoelastic Models Of Brain Tissue Mechanical Properties.” ASME, pp. 297–298, 1999.
- [24] K. Miller and K. Chinzei, “Mechanical properties of brain tissue in tension,” *J. Biomech.*, vol. 35, no. 4, pp. 483–490, 2002.
- [25] S. Budday, G. Sommer, G. A. Holzapfel, P. Steinmann, and E. Kuhl, “Viscoelastic parameter identification of human brain tissue,” *J. Mech. Behav. Biomed. Mater.*, vol.

- 74, no. May, pp. 463–476, 2017.
- [26] G. Franceschini, “the Mechanics of Human Brain Tissue,” *Dep. Mech. Struct. Eng.*, p. 130, 2006.
- [27] B. Rashid, M. Destrade, and M. D. Gilchrist, “Hyperelastic and Viscoelastic Properties of Brain Tissue in Tension,” *Proc. ASME 2012 Int. Mech. Eng. Congr. Expo.*, p. 921, 2012.
- [28] A. F. Christ *et al.*, “Mechanical difference between white and gray matter in the rat cerebellum measured by scanning force microscopy,” *J. Biomech.*, vol. 43, no. 15, pp. 2986–2992, 2010.
- [29] S. Budday *et al.*, “Mechanical properties of gray and white matter brain tissue by indentation,” *J. Mech. Behav. Biomed. Mater.*, vol. 46, pp. 318–330, 2016.
- [30] E. P. Canovic *et al.*, “Characterizing Multiscale Mechanical Properties of Brain Tissue Using Atomic Force Microscopy, Impact Indentation, and Rheometry,” *J. Vis. Exp.*, no. 115, 2016.
- [31] L. Qian *et al.*, “Influence of strain rate on indentation response of porcine brain,” *J. Mech. Behav. Biomed. Mater.*, vol. 82, no. March, pp. 210–217, 2018.
- [32] J. D. Finan, S. N. Sundaresh, B. S. Elkin, G. M. McKhann, and B. Morrison, “Regional mechanical properties of human brain tissue for computational models of traumatic brain injury,” *Acta Biomater.*, vol. 55, pp. 333–339, 2017.
- [33] M. A. Green, L. E. Bilston, and R. Sinkus, “*In vivo* brain viscoelastic properties measured by magnetic resonance elastography,” *NMR Biomed.*, vol. 21, no. 7, pp. 755–764, Aug. 2008.
- [34] F. B. Freimann *et al.*, “MR elastography in a murine stroke model reveals correlation of macroscopic viscoelastic properties of the brain with neuronal density,” *NMR Biomed.*, vol. 26, no. 11, pp. 1534–1539, Nov. 2013.
- [35] C. Klein *et al.*, “Enhanced Adult Neurogenesis Increases Brain Stiffness: In Vivo Magnetic Resonance Elastography in a Mouse Model of Dopamine Depletion,” 2014.
- [36] M. C. Murphy, J. Huston, and R. L. Ehman, “MR elastography of the brain and its application in neurological diseases,” *Neuroimage*, Oct. 2017.
- [37] L. V. Hiscox *et al.*, “High-resolution magnetic resonance elastography reveals differences in subcortical gray matter viscoelasticity between young and healthy older adults,” *Neurobiol. Aging*, vol. 65, pp. 158–167, May 2018.
- [38] K. Brodmann, *Vergleichende Lokalisationslehre der Grosshirnrinde: in ihren Prinzipien dargestellt auf Grund des Zellenbaues*. Leipzig: J.A. Barth, 1909.

- [39] O. Vogt, "Die myeloarchitektonische Felderung des menschlichen Stirnhirns," *J. Psychol. Neurol.*, vol. 15, no. 221–232, 1910.
- [40] C. Vogt and O. Vogt, "Allgemeinere Ergebnisse unserer Hirnforschung. Zweite Mitteilung. Das Wesen der topischen architektonischen Differenzen des Cortex cerebri," *J. Psychol. Neurol.*, vol. 25, pp. 292–360, 1919.
- [41] M. Judaš and M. Cepanec, "Oskar vogt: The first myeloarchitectonic map of the human frontal cortex," *Transl. Neurosci.*, vol. 1, no. 1, pp. 72–94, 2010.
- [42] K. Amunts and K. Zilles, "Architectonic Mapping of the Human Brain beyond Brodmann," *Neuron*, vol. 88, pp. 1086–1107, 2015.
- [43] A. Schleicher and K. Zilles, "A quantitative approach to cytoarchitectonics: Analysis of structural inhomogeneities in nervous tissue using an image analyser," *J. Microsc.*, vol. 157, no. 3, pp. 367–381, Mar. 1990.
- [44] A. Wree, A. Schleicher, and K. Zilles, "Estimation of volume fractions in nervous tissue with an image analyzer," *J. Neurosci. Methods*, vol. 6, no. 1–2, pp. 29–43, Jul. 1982.
- [45] A. Schleicher, P. Morosan, A. Katrin, A. Ae, and K. Zilles, "Quantitative Architectural Analysis: A New Approach to Cortical Mapping," *J. Autism Dev. Disord.*, vol. 39, pp. 1568–1581, 2009.
- [46] K. Zilles *et al.*, "A rchitectonics of the human cerebral cortex and transmitter receptor ngerprints: reconciling functional neuroanatomy and neurochemistry," *Eur. Neuropsychopharmacol.*, vol. 12, pp. 587–599, 2002.
- [47] N. Palomero-Gallagher and K. Zilles, "Cortical layers: Cyto-, myelo-, receptor- and synaptic architecture in human cortical areas," *Neuroimage*, Aug. 2017.
- [48] K. Holtzmann, H. O. B. Gautier, A. F. Christ, J. Guck, R. T. Káradóttir, and K. Franze, "Brain tissue stiffness is a sensitive marker for acidosis," *J. Neurosci. Methods*, vol. 271, pp. 50–54, 2016.
- [49] P. R. Huttenlocher, "Synaptic density in human frontal cortex — Developmental changes and effects of aging," *Brain Res.*, vol. 163, no. 2, pp. 195–205, Mar. 1979.
- [50] A. M. Thomson, "Functional maps of neocortical local circuitry," *Front. Neurosci.*, vol. 1, no. 1, pp. 19–42, 2007.
- [51] A. M. Nahum, R. Smith, and C. C. Ward, "Intracranial Pressure Dynamics During Head Impact," 1977.
- [52] L. Zhang, A. King, and K. Yang, "Recent Advances in Brain Injury Research : A New Human Head Model Development and Validation Recent Advan," *Stapp Car Crash J.*, vol. 45, no. November, 2001.

- [53] W. N. Hardy *et al.*, “A study of the response of the human cadaver head to impact.,” *Stapp Car Crash J.*, vol. 51, pp. 17–80, Oct. 2007.
- [54] B. Yang *et al.*, “Development of a finite element head model for the study of impact head injury.,” *Biomed Res. Int.*, vol. 2014, p. 408278, 2014.
- [55] P. Saboori and A. Sadegh, “On the properties of brain sub arachnoid space and biomechanics of head impacts leading to traumatic brain injury,” *Adv. Biomech. Appl.*, vol. 1, no. 4, pp. 253–267, 2014.
- [56] P. Saboori and A. Sadegh, “Brain subarachnoid space architecture: Histological approach,” *ASME 2011 Int. Mech. Eng. Congr. Expo. IMECE 2011*, vol. 2, no. 2007, pp. 89–94, 2011.
- [57] P. Saboori and A. Sadegh, “Histology and Morphology of the Brain Subarachnoid Trabeculae,” *Anat. Res. Int.*, vol. 2015, p. 279814, 2015.
- [58] N. L. Strominger, R. J. Demarest, and L. B. Laemle, *Noback’s Human Nervous System*, Seventh Ed. New York: Springer, 2012.
- [59] G. J. Tortora and B. Derrickson, *Principles of Anatomy and Physiology*, 13th editi. USA: Wiley, 2012.
- [60] A. Schleicher, P. Morosan, K. Amunts, and K. Zilles, “Quantitative architectural analysis: A new approach to cortical mapping,” *J. Autism Dev. Disord.*, vol. 39, no. 11, pp. 1568–1581, 2009.
- [61] M. Matsumae *et al.*, “Age-related changes in intracranial compartment volumes in normal adults assessed by magnetic resonance imaging,” *J. Neurosurg.*, vol. 84, no. 6, pp. 982–991, 1996.
- [62] J. S. Allen, J. Bruss, C. K. Brown, and H. Damasio, “Normal neuroanatomical variation due to age: The major lobes and a parcellation of the temporal region,” *Neurobiol. Aging*, vol. 26, no. 9, pp. 1245–1260, 2005.
- [63] D. D. Blatter *et al.*, “Quantitative volumetric analysis of brain MR: Normative database spanning 5 decades of life,” *Am. J. Neuroradiol.*, vol. 16, no. 2, pp. 241–251, 1995.
- [64] A. M. Hedman, N. E. M. van Haren, H. G. Schnack, R. S. Kahn, and H. E. Hulshoff Pol, “Human brain changes across the life span: A review of 56 longitudinal magnetic resonance imaging studies,” *Hum. Brain Mapp.*, vol. 33, no. 8, pp. 1987–2002, 2012.
- [65] R. Riello *et al.*, “Brain volumes in healthy adults aged 40 years and over: a voxel-based morphometry study,” *Aging Clin Exp Res*, vol. 17, no. 4, pp. 329–336, 2005.
- [66] J. H. Cole *et al.*, “Spatial patterns of progressive brain volume loss after moderate-severe traumatic brain injury,” *Brain*, vol. 141, no. 3, pp. 822–836, 2018.

- [67] C. Economo, "Frontal Lobe," in *Cellular Structure of the human Cerebral Cortex*, L. C. Triarhou, Ed. Basel: Karger, 2009, pp. 32–72.
- [68] M. Marín-Padilla, "The Mammalian Pyramidal Neuron: Development, Structure, and Function," in *The Human Brain*, Berlin Heidelberg : Springer-Verlag , 2011.
- [69] N. Palomero-Gallagher and K. Zilles, "Cortical layers: Cyto-, myelo-, receptor- and synaptic architecture in human cortical areas," *Neuroimage*, no. August, pp. 1–26, 2017.
- [70] T. J. CULLEN, M. A. WALKER, S. L. EASTWOOD, M. M. ESIRI, P. J. HARRISON, and T. J. CROW, "Anomalies of asymmetry of pyramidal cell density Anomalies of asymmetry of pyramidal cell density and structure in dorsolateral prefrontal cortex and structure in dorsolateral prefrontal cortex in schizophrenia," *BRITISH JOURNAL OF PSYCHIATRY*, vol. 188, pp. 26–31, 2006.
- [71] T. Nevian, M. E. Larkum, A. Polsky, and J. Schiller, "Properties of basal dendrites of layer 5 pyramidal neurons: a direct patch-clamp recording study," *Nat. Neurosci.*, vol. 10, no. 2, pp. 206–214, Feb. 2007.
- [72] N. Spruston, "Pyramidal neurons: Dendritic structure and synaptic integration," *Nat. Rev. Neurosci.*, vol. 9, no. 3, pp. 206–221, 2008.
- [73] S. a Marshall and R. Bell, "Traumatic Brain Injury."
- [74] M. Faul, L. Xu, M. M. Wald, and V. G. Coronado, "Traumatic brain injury in the United States: emergency department visits, hospitalizations, and deaths," *Centers Dis. Control Prev. Natl. Cent. Inj. Prev. Control*, pp. 891–904, 2010.
- [75] A. Sidaros *et al.*, "Long-term global and regional brain volume changes following severe traumatic brain injury: A longitudinal study with clinical correlates," *Neuroimage*, vol. 44, no. 1, pp. 1–8, 2009.
- [76] C. A. Raji, D. A. Merrill, J. R. Barrio, B. Omalu, and G. W. Small, "Progressive Focal Gray Matter Volume Loss in a Former High School Football Player: A Possible Magnetic Resonance Imaging Volumetric Signature for Chronic Traumatic Encephalopathy," *Am. J. Geriatr. Psychiatry*, vol. 24, no. 10, pp. 784–790, 2016.
- [77] A. C. Mckee *et al.*, "Chronic Traumatic Encephalopathy in Athletes: Progresive Tauopathy following Repetitive Head Injury," *J. Neuropathol. Exp. Neurol.*, vol. 68, no. 7, pp. 709–735, 2009.
- [78] S. Kleiven, "Consequences of Reduced Brain Volume Following Impact in," *Clin. Neurosci.*, pp. 1–13, 2002.
- [79] Y. Luo, Z. Li, and H. Chen, "Finite-element study of cerebrospinal fluid in mitigating closed head injuries," *Proc. Inst. Mech. Eng. Part H J. Eng. Med.*, vol. 226, no. 7, pp.

- 499–509, 2012.
- [80] F. A. Bandak and R. H. Eppinger, “A Three-Dimensional Finite Element Analysis of the Human Brain Under Combined Rotational and Translational Accelerations,” 1994.
- [81] L. E. Thibault, T. A. Gennarelli, S. S. Margulies, J. Marcus, and R. Eppinger, “The Strain Dependent Pathophysiological Consequences of Inertial Loading on Central Nervous System Tissue,” in *IRCOBI*, 1990.
- [82] P. Brewick, R. Saunders, and A. Bagchi, “Biomechanical Modeling of the Human Head,” 2017.
- [83] M. S. CHAFI, S. GANPULE, L. GU, and N. CHANDRA, “Dynamic Response of Brain Subjected To Blast Loadings: Influence of Frequency Ranges,” *Int. J. Appl. Mech.*, vol. 03, no. 04, pp. 803–823, 2011.
- [84] G. A. Holzapfel and R. W. Ogden, *Mechanics of biological tissue*. 2006.
- [85] W. Flugge, *Viscoelasticity*. Waltham, Mass, 1967.
- [86] R. Lakes, *Viscoelastic Materials*. Cambridge: Cambridge University Press, 2009.
- [87] F. J. Lockett, *Nonlinear viscoelastic solids*. Academic Press, 1972.
- [88] R. Michalczyk, “Implementation of Generalized Viscoelastic Material Model in Abaqus Code,” *Logistyka*, vol. 6, no. January 2011, 2011.
- [89] B. Babaei, S. D. Abramowitch, E. L. Elson, S. Thomopoulos, and G. M. Genin, “A discrete spectral analysis for determining quasi-linear viscoelastic properties of biological materials,” *J. R. Soc. Interface*, vol. 12, no. 113, p. 20150707, Dec. 2015.
- [90] M. S. Chafi, V. Dirisala, G. Karami, and M. Ziejewski, “A finite element method parametric study of the dynamic response of the human brain with different cerebrospinal fluid constitutive properties,” *Proc. Inst. Mech. Eng. Part H J. Eng. Med.*, vol. 223, no. 8, pp. 1003–1019, 2009.
- [91] Abaqus/Explicit Advanced techniques, “Lecture 3: Numerical Modeling of Materials,” *iMechanica*, 2005.
- [92] J. McElhaney, *Dynamic mechanical properties of scalp and brain*. 1969.
- [93] J.-X. Jin, J.-Y. Zhang, X.-W. Song, H. Hu, X.-Y. Sun, and Z.-H. Gao, “Effect of Cerebrospinal Fluid Modeled With Different Material Properties on a Human Finite Element Head Model,” *J. Mech. Med. Biol.*, vol. 15, no. 1, p. 1550027, 2014.
- [94] E. Lozano-Mínguez, M. Palomar, D. Infante-García, M. J. Rupérez, and E. Giner, “Assessment of Mechanical Properties of Human Head Tissues for Trauma Modelling,” *Int. j. numer. method. biomed. eng.*, no. January, p. e2962, 2018.
- [95] M. T. Abba, “Spherical Nanoindentation Protocols for Extracting Microscale

- Mechanical Properties in Viscoelastic Materials Spherical Nanoindentation Protocols for Extracting Microscale Mechanical Properties in,” no. December, 2015.
- [96] E. K. Dimitriadis, F. Horkay, J. Maresca, B. Kachar, and R. S. Chadwick, “Determination of Elastic Moduli of Thin Layers of Soft Material Using the Atomic Force Microscope.”
- [97] Asylum, “MFP-3D user manual (full),” 2008.
- [98] H. Hertz, *Miscellaneous papers*. London ;;New York: MacMillan and Co., 1896.
- [99] J. R. M. Radok, “Visco-elastic stress analysis,” *Q. Appl. Math.*, vol. 15, no. 2, pp. 198–202, Jul. 1957.
- [100] Y. M. Efremov, W.-H. Wang, S. D. Hardy, R. L. Geahlen, and A. Raman, “Measuring nanoscale viscoelastic parameters of cells directly from AFM force-displacement curves,” *Sci. Rep.*, vol. 7, no. 1, p. 1541, May 2017.
- [101] G. W. Gill, *Cytopreparation*. New York: Springer, 2013.
- [102] C. Heinrich, A. M. Waas, and A. S. Wineman, “Determination of material properties using nanoindentation and multiple indenter tips,” *Int. J. Solids Struct.*, vol. 46, no. 2, pp. 364–376, 2009.
- [103] B. G. Amidan, T. A. Ferryman, and S. K. Cooley, “Data outlier detection using the Chebyshev theorem,” in *2005 IEEE Aerospace Conference*, 2005, pp. 3814–3819.
- [104] H. Lohninger, “Fundamentals of Statistics,” 2012. [Online]. Available: [http://www.statistics4u.com/fundstat\\_eng/copyright.html](http://www.statistics4u.com/fundstat_eng/copyright.html). [Accessed: 02-Jul-2018].
- [105] E. M. Darling, S. Zauscher, J. A. Block, and F. Guilak, “A Thin-Layer Model for Viscoelastic, Stress-Relaxation Testing of Cells Using Atomic Force Microscopy: Do Cell Properties Reflect Metastatic Potential?”
- [106] Stevens, “Post Hoc Tests in ANOVA,” 1999.
- [107] N. Sasaki, “Viscoelastic Properties of Biological Materials,” *Viscoelasticity - From Theory to Biol. Appl.*, pp. 99–122, 2012.
- [108] H. Wanifuchi, T. Shimizu, and T. Maruyama, “Age-related changes in the proportion of intracranial cerebrospinal fluid space measured using volumetric computerized tomography scanning,” *J. Neurosurg.*, vol. 97, no. 3, pp. 607–10, 2002.
- [109] Z. Asgharpour, D. Baumgartner, R. Willinger, M. Graw, and S. Peldschus, “The validation and application of a finite element human head model for frontal skull fracture analysis,” *J. Mech. Behav. Biomed. Mater.*, vol. 33, pp. 16–23, May 2014.
- [110] C. Klug, U.-P. Dipl-Ing Drtechn Herman Steffan Betreuer, and D.-I. Drtechn Florian Feist, “Modellierung des Cerebrospinal Fluids,” 2013.

- [111] L. Sakka, G. Coll, and J. Chazal, "Anatomy and physiology of cerebrospinal fluid," *Eur. Ann. Otorhinolaryngol. Head Neck Dis.*, vol. 128, no. 6, pp. 309–316, 2011.
- [112] P. Taylor, A. Brundage, D. Burnett, C. Cooper, A. Gullerud, and R. Terpsma, "IMECE 2015-52696," in *Virtual Simulation of the Effects of Intracranial Fluid Cavitation*, 2016, pp. 1–10.
- [113] F. Yetkin, U. Kayabas, Y. Ersoy, Y. Bayindir, S. A. Toplu, and I. Tek, "Cerebrospinal fluid viscosity: A novel diagnostic measure for acute meningitis," *South. Med. J.*, vol. 103, no. 9, pp. 892–895, 2010.
- [114] C. Klug, W. Sinz, G. Brenn, and F. Feist, "Experimental Sphere-in-Sphere Testing for the Validation of a Numerical Cerebrospinal Fluid Model," *IRCOBI Conf.*, pp. 483–496, 2013.
- [115] P. A. Taylor and C. C. Ford, "Simulation of Blast-Induced Early-Time Intracranial Wave Physics leading to Traumatic Brain Injury," *J. Biomech. Eng.*, vol. 131, no. 6, p. 061007, 2009.
- [116] D. F. Moore, A. Jérusalem, M. Nyein, L. Noels, M. S. Jaffee, and R. A. Radovitzky, "Computational biology - Modeling of primary blast effects on the central nervous system," *Neuroimage*, vol. 47, no. SUPPL. 2, pp. T10–T20, 2009.
- [117] M. Petrides and D. N. Pandya, "The Frontal Cortex," in *The Human Nervous System*, Academic Press, 2012, pp. 988–1011.
- [118] S. Eickhoff *et al.*, "High-resolution MRI reflects myeloarchitecture and cytoarchitecture of human cerebral cortex," *Hum. Brain Mapp.*, vol. 24, no. 3, pp. 206–215, Mar. 2005.
- [119] Royal Society of Chemistry (Great Britain). Faraday Division, *Molecular basis of viscoelasticity*. Faraday Division, the Royal Society of Chemistry, 1984.
- [120] D. Chimich, N. Shrive, C. Frank, L. Marchuk, and R. Bray, "Water content alters viscoelastic behaviour of the normal adolescent rabbit medial collateral ligament," *J. Biomech.*, vol. 25, no. 8, pp. 831–837, Aug. 1992.
- [121] G. J. Creus, *Viscoelasticity: basic theory and applications to concrete structures*. Springer-Verlag, 1986.
- [122] G. McIlvain, H. Schwarb, N. J. Cohen, E. H. Telzer, and C. L. Johnson, "Mechanical properties of the in vivo adolescent human brain," *Dev. Cogn. Neurosci.*, vol. 34, pp. 27–33, Nov. 2018.
- [123] H. Hassanin and K. Jiang, "Fabricating functionally graded ceramic micro-components using soft lithography," in *Advances in Ceramic Matrix Composites*, Elsevier, 2014, pp. 611–623.



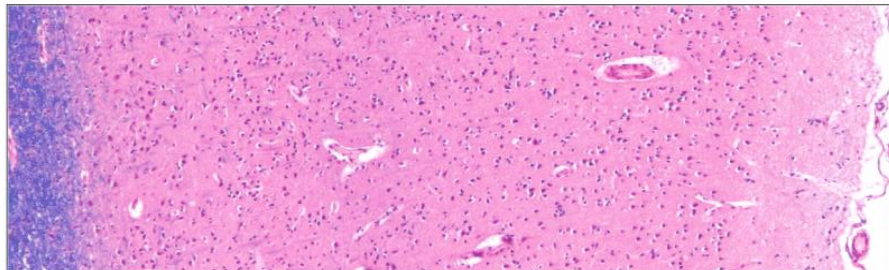
- [124] Z. Liu, M. A. Meyers, Z. Zhang, and R. O. Ritchie, “Functional gradients and heterogeneities in biological materials: Design principles, functions, and bioinspired applications,” *Prog. Mater. Sci.*, vol. 88, pp. 467–498, Jul. 2017.
- [125] S. Keihaninejad, R. A. Heckemann, G. Fagiolo, M. R. Symms, J. V. Hajnal, and A. Hammers, “A robust method to estimate the intracranial volume across MRI field strengths (1.5T and 3T),” *Neuroimage*, vol. 50, no. 4, pp. 1427–1437, 2010.
- [126] N. Spruston, “Pyramidal neurons: dendritic structure and synaptic integration,” *Nat. Rev. Neurosci.*, vol. 9, no. 3, pp. 206–221, Mar. 2008.

# Appendix A – An overview of cortical cell characteristics

(www.drawittoknowit.com)

## CEREBRAL CORTICAL HISTOLOGY

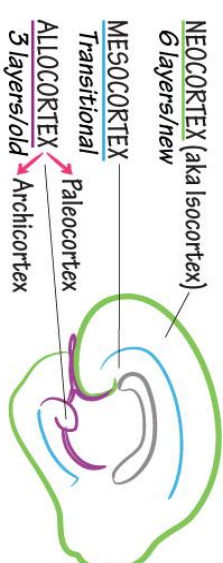
Neocortical Layers



- I. MOLECULAR  
Cell sparse; primarily axons & dendrites.
- II. EXTERNAL GRANULAR  
Non-pyramidal cells: 5 to 15 μm (eg, stellate cells).
- III. EXTERNAL PYRAMIDAL  
Pyramidal cells of varying sizes: 10 to 80 μm.
- IV. INTERNAL GRANULAR  
Non-pyramidal cells. External band of Baillarger.
- V. INTERNAL PYRAMIDAL  
Large pyramidal cells (eg, Betz cell) Internal band of Baillarger.
- VI. MULTIFORM  
Multitude of cell types. Blends into underlying white matter.

WHITE MATTER

## Cerebral Cortex Classification

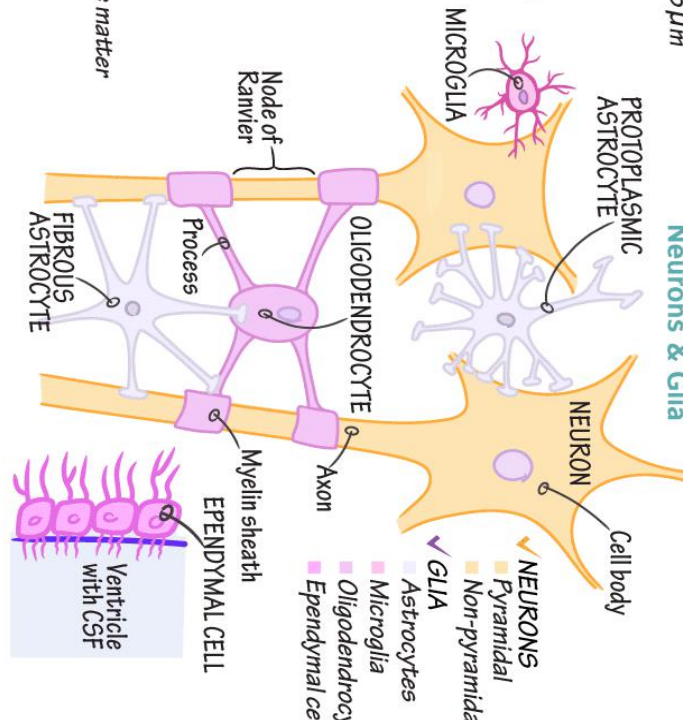


NEOCORTEX (aka Isocortex)  
6 layers/new

MESOCORTEX  
Transitional

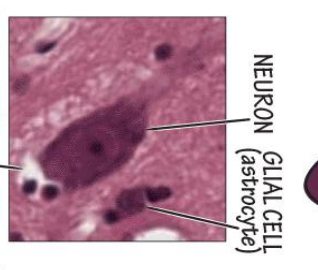
ALLOCORTEX  
3 layers/old  
Archicortex

### Neurons & Glia



- ✓ NEURONS
  - Pyramidal
  - Non-pyramidal
- ✓ GLIA
  - Astrocytes
  - Microglia
  - Oligodendrocytes
  - Ependymal cells

### Neurons & Glia – Histology



NEURON

- Process
- Nucleus
- Nucleolus
- Cytoplasm

GLIAL CELL (astrocyte)

NEURON

- Axon
- Dendrite
- Myelin sheath
- EPENDYMAL CELL
- Ventricle with CSF

## Appendix B - Technical specifications of the applied cantilever

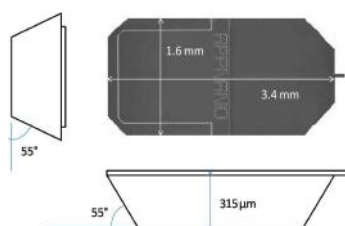
### Technical Specifications Sheet

### Probe Model: SICON-TL

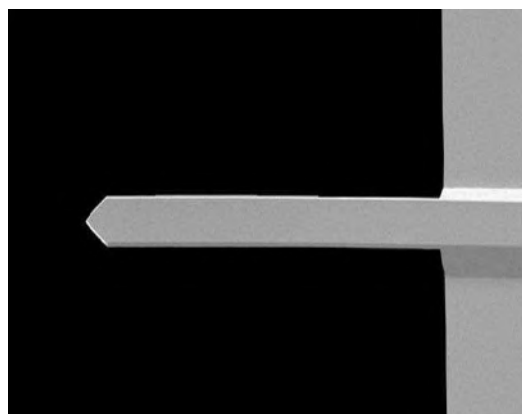
**APPNANO** probes are compatible with most commercially available SPMs. These probes are nanofabricated using highly doped single crystal silicon with unparalleled reproducibility, robustness and sharpness for consistent high resolution imaging capabilities.

**SICON-TL Probes** are tipless probes designed for contact mode applications. These probes have a long, thin cantilever allowing for a low spring constant and improved laser clearance.

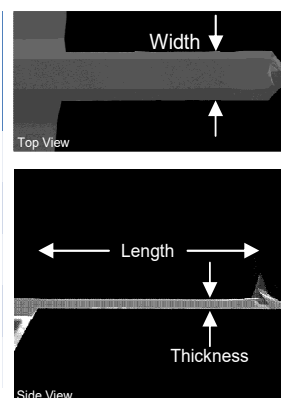
Handle Chip Specifications	
L x W x T	3.4 mm x 1.6 mm x 315 $\mu$ m
Alignment Grooves	YES



Cantilever Specifications	
Material	Si
Shape	Rectangular
Reflex Side Coating	None



Parameter	Value		
	Nominal	Minimum	Maximum
Spring Constant (N/m)	0.29	0.13	0.60
Frequency (kHz)	15	11	19
Length ( $\mu$ m)	450	440	460
Width ( $\mu$ m)	49	44	54
Thickness ( $\mu$ m)	2.5	2.0	3.0



Ordering Information	
Part Number	Probes
SICON-TL-10	10
SICON-TL-20	20
SICON-TL-50	50
SICON-TL-200	200
SICON-TL-W	410 - 424

#### NOTES:

1. The specification range is **guaranteed**. The values of spring constant and frequency are calculated using mathematical formulation
2. These probes feature **alignment grooves** compatible with all alignment chips available in the market.
3. Please contact our **distributor** in your area to **order** the probes.
4. For more technical information, please contact either our distributor in your area or e-mail us directly at [info@appnano.com](mailto:info@appnano.com)

**Appendix C - Transitions between layers on AFM images ( $\mu\text{m}$  scale)**

